

N O T I C E

THIS DOCUMENT HAS BEEN REPRODUCED FROM
MICROFICHE. ALTHOUGH IT IS RECOGNIZED THAT
CERTAIN PORTIONS ARE ILLEGIBLE, IT IS BEING RELEASED
IN THE INTEREST OF MAKING AVAILABLE AS MUCH
INFORMATION AS POSSIBLE

N82-20654

(DOE/JPL-954852-81/4) EBIC/TEM
INVESTIGATIONS OF DEFECTS IN SOLAR SILICON
RIBBON MATERIALS Final Report (Cornell
Univ., Ithaca, N. Y.) 131 p HC A07/MF A01

Unclas
CSCL 10A G3/44 09332

9950-628
DOE/JPL-954852-81/4

Distribution Category UC-63

EBIC/TEM INVESTIGATIONS OF DEFECTS IN SOLAR SILICON RIBBON MATERIALS

January 1981

Final Report

JPL Contract No. 954852



by

D.G.Ast

Materials Science and Engineering

Bard Hall, Cornell University

Ithaca NY, 14853

The JPL low cost solar array project is sponsored by the US Department of Energy and forms part of the Solar Photovoltaic Conversion Program to initiate a major effort towards the development of low-cost solar arrays. This work was performed for the Jet Propulsion Laboratory, California Institute of Technology, by agreement between NASA and DOE.

INTRODUCTION

Many of the growth methods which produce silicon material for the fabrication of inexpensive solar cells yield material which contains a relative high density of structural defects, such as grain boundaries, twin boundaries and dislocations. Because such defects will, in general, reduce the efficiency of a solar cell, there is a technological incentive to study the formation and structure of such defects, and their influence on the minority carrier lifetime.

In the following section, we will discuss the applications of TEM and EBIC to the study of crystalline defects.

CORRELATED EBIC AND TEM STUDIES OF DEFECTS

A convenient way to study the relationship between the electrical properties and the structure of a defect is to combine electron beam induced current microscopy (EBIC) with transmission electron microscopy [1,2]. The principles underlying EBIC are identical to those governing the operation of a solar cell under optical excitation. The specimen is illuminated with a narrow beam of electrons which is scanned across the cell and the short circuit current $I(o)$ is collected by a Schottky or p-n junction and recorded as a function of position. $I(o)$ decreases in the vicinity of defects which act as recombination centers. Calculations [3] and experiment [4] show that the spatial resolution of the technique is not, as one might suspect, set by the diffusion length of the minority carriers, but largely depends on the volume into which the incident electrons are scattered. This generation volume varies with energy and is, at practical beam voltages between 10 and 20 keV, in the order of 1 μ m, i.e. the resolution of EBIC images is comparable to that of optical micrographs.

The relatively low spatial resolution of EBIC requires that the defects being studied are separated by several microns. Transmission electron microscopy (TEM) can supply detailed information on the structure of defects. The chief disadvantage of transmission electron microscopy at conventional beam voltages (100 KeV) is the necessity to prepare thin (below 100 nanometer) specimens. Usually, the specimen is polished until a small hole with sloping edges is formed. Observation is restricted to the areas in the vicinity of the hole. Much larger areas can be inspected (and hence correlated with the EBIC image) by high voltage transmission electron microscopy (1 MeV) which is capable of penetrating several microns of silicon. For this reason EBIC images are usually correlated with HVTEM micrographs, unless high resolution (lattice images) is required. The latter are obtained from imaging very thin sections of the specimen in high resolution instruments operating at conventional voltages.

THE DEFECT STRUCTURE OF LASS THIN RIBBON MATERIAL.

The above techniques were applied to investigate the defect structure of edge defined film growth (EFG) material, fabricated by Mobil Tyco; web dendritic ribbons (WEB), grown by Westinghouse Co, and ribbon to ribbon recrystallized material (RTR) produced by Motorola.

The most common defects in all of these materials are coherent first order twin boundaries. These coherent twins can be very thin, a few atomic layers. Bundles of these twins which contain odd numbers of twins will, in optical images (i.e. resolution of about 1 μm) appear as a seemingly single first order twin boundary. First order coherent twin boundaries are not electrically active, except at locations where they contain intrinsic (grain boundary dislocations). These dislocations take up small deviations from the ideal twin relation and play the same role in twin boundaries as conventional edge and screw dislocations in small angle tilt and twist boundaries.

Besides first order coherent twin boundaries (which are called SIGMA = 3 boundaries in the notation developed by Bollmann), the materials generally contain dislocations and higher order twin boundaries. Some of these higher order twin boundaries share the (111) habit plane of first order coherent twin boundaries. A first order coherent twin boundary may "split" by emitting a first order twin boundary "sideways" (i.e. on an other twinning plane) and continue, in a straight continuation, as a second order (111)/(115) twin. These twins are strongly electrically active.

The results obtained on the various materials are ordered as follows:

- i) RTR material
- ii) WEB material
- iii) EFG material.

Additional articles which discuss the investigation of grain boundaries in Si in more detail are attached in the appendix for the those readers which are interested in more details.

REFERENCES

1. J. Heydenreich, H. Blumtritt, R. Gleichmann and H. ,Johansen. J. de Physique, Supplement C-6 (1979) p.23
2. H. Strunk and D. G. Ast. 38th Ann.Proc.Electron.Microscopy.Soc.Amer., E. W. Bailey (ed), San Francisco. CA (1980) p.322
3. C. Donolato, Appl.Phys.Let. 34 (1979) p.80; Optik 52 (1979/80) p.19; Solid State Electronics 22 (1979) 797
4. H. J. Leamy, L. C. Kimerling and S. D. Ferris, Scanning Electron Microscopy. Vol.1 (SEM Inc.,AMP O'Hare, IL 6066, USA. 1978) p.717

I) THE DEFECT STRUCTURE OF RTR SILICON ; PART I

Abstract

The defect structure of one RTR ribbon supplied by JPL (sample identification #6-731, run 803) was evaluated by transmission electron microscopy, complemented by other techniques such as etching or scanning electron microscopy. In addition to dislocations, stacking faults and twins, a high density ($\sim 10^{13} \text{ cm}^{-3}$) of small, heavy metal related precipitates were observed. Such precipitates, in general, act as efficient recombination centers and may be responsible for the low efficiency of solar cells fabricated from RTR ribbons.

1. Introduction

In the JPL/DOE low-cost silicon solar array project characterization of the defect structure of silicon ribbon material is part of the effort to reduce costs of the ribbon fabrication. Crystalline defects in semi-conducting materials frequently affect the electrical properties, (e.g., $1/\tau$), for example, minority carrier lifetime, by acting as efficient recombination centers. Analysis of the nature of the defects and their electronic properties can aid in controlling ribbon growth such that the content of electrically active defects is reduced to a tolerable level.

This report summarizes the results obtained during an extensive analysis of one Motorola RTR ribbon, sample identification #6-731, run 803. This ribbon was produced by CVD from SiHCl_3 onto a Mo substrate. The approximately 12 mil thick and 1 - 1.25 inch wide ribbon was subsequently laser recrystallized with a feed rate of .5 inch/min. and a growth rate of 1 inch/min. causing a factor-of-two reduction in thickness. Finally the ribbon was annealed in N_2 for 1 hour at 1100°C .

2. Experimental techniques

Transmission electron microscopy (TEM) was used to characterize the material. The TEM samples were produced by breaking off small pieces from different areas of the ribbon to ensure good statistics. These pieces were mechanically ground to a thickness of approx. $50\text{ }\mu\text{m}$, from one side to investigate the surface-near regions and from both sides to investigate the central part of the ribbon. The slices were finally thinned by ion milling until a hole appeared. To check that no artifacts were introduced by ion milling, some slices were thinned by chemical dissolution in $\text{HNO}_3:\text{HF}:\text{HAC}$ 5:1:1. These specimens showed preferential attack at defects, especially at twin boundaries (e.g., Fig. 5). All samples were investigated in a

Siemens 102 Elmiskop, using an accelerating voltage of 125 kV.

Other techniques used to complement the TEM were: etch-pitting and optical microscopy, neutron activation analysis and Laue X-raying; scanning electron microscopy in the microprobe-(see below) and EBIC-mode (electron beam induced current) on Schottky diodes prepared on the ribbon material.

3. Observed defect structure

Different types of defects were observed and these shall be considered separately. Table 1 summarizes the main data.

Lattice dislocations. These are present in the ribbon in a random manner (at least on the scale of TEM micrographs). They are generally bowed out, and sometimes exhibit cusps indicating that they are pinned at jogs in their lines. A typical array is shown in Fig. 1. Clusters of dislocations have been found only infrequently. These clusters are generally associated with one or several planar faults such as a microtwin (see also below). We did not see any indication of a decoration of the dislocation lines by microprecipitates.

The overall appearance of the dislocation structure suggests that the dislocations were created by glide, probably caused by thermal stresses created during cooling of the ribbon. The fact that precipitation occurred in the bulk of the ribbon (see below) and not at dislocations indicates that the lattice dislocations were formed after the precipitation process, possibly after the annealing treatment, since the dislocation structure does not exhibit features due to annealing.

Stacking faults. These occur on all four {111}-planes. They have a round appearance with a diameter of approximately 3 μm . The two stacking faults visible in Fig. 2 are confined to differently inclined {111}-planes

and are only partially contained in the foil. Stacking faults of this type are a common feature in silicon crystals cooled from the melt (or high temperatures) and result from the condensation of intrinsic point defects. The size of these stacking faults leads to the presumption that they are stabilized against unfauling by impurities /2/, however, visible decoration by microprecipitates has not been observed.

Twins. These occur in a macroscopic network of twin-'needles'. Their thickness is generally in the range of a few to several tens of {111}-planes, and their lengths extend to a few mm. Isolated twin boundaries (two of which could be thought of as representing a 'thick' twin) are also present. Fig. 3 shows a typical array of such twins and twin boundaries. The boundaries are slightly inclined in the foil and exhibit in part fringe contrast effects. Fig. 3 also shows the relative rare case of a thin twin ending in the matrix. Such ends are generally associated with a few lattice dislocations which sometimes form tangles and/or have small dislocation loops nearby (Fig. 4). It should be noticed that the twin boundaries contain relatively few twin boundary dislocations, most of which seem to be caused by the interaction of lattice dislocations with the boundaries (Fig. 5). Only one dislocation has been found to be decorated with microprecipitates similar to those described in the following section. In large grain EFG ribbon, twin boundary dislocations are very common (e.g., 3) and are efficient recombination centers for minority carriers /3;4/.

Precipitates. Close inspection of Figs. 1 to 5 reveals that in addition to the defects described above small defects are present in relative large density (Tab. 1), giving rise to loop-like contrast structures. Close examination shows the contrast to be of Ashby-Brown-type /5/, i.e., it arises from precipitates acting as strain centers. These precipitates are

quasi-homogeneously distributed in the ribbon material. The nature of the strain, whether compressional or dilatational, could not be determined because of the anisotropic shape of the precipitates. Information on the shape was obtained by high resolution TEM, i.e., weak-beam dark-field imaging (e.g., Fig. 6e and f), bright-field imaging with many beams excited ('multi-beam', Fig. 7) and lattice resolution (Fig. 8). Fig. 6 to 8 are seen along a $\langle 110 \rangle$ -direction (Fig. 6 nearly, Figs. 7 and 8 exactly). The projected outlines of the precipitates tend to follow $\langle 112 \rangle$ -directions; frequently a regular rhombic shape is formed (Fig. 7 and 8a), but irregularities in the outlines also occur (Fig. 6 and 8b). Edge-on observations suggest that the precipitates are platelets with sometimes a thickened central region and a tendency to lie preferably on planes near $\{100\}$. However, large deviations may occur. From the direction of the projected outlines and the $\{100\}$ habit plane it follows that the precipitate edges are aligned preferentially along $\langle 110 \rangle$ -directions. Imaging with $\{004\}$ reflections always minimizes the strain-field contrast, e.g., Fig. 6d. Each precipitate then shows up as a dark area, the geometry of which compares to that obtained from high resolution microscopy (Fig. 6e, f). This contrast behavior is typical of 'absorption contrast', which indicates the precipitates to be of higher mass density than the matrix.

The crystallographic nature of the precipitates could not be determined, since it was not possible to obtain diffraction patterns from the precipitates. The lattice images (Fig. 8) exhibit 'amorphous' looking patches inside the precipitates, so that the precipitates are probably amorphous in nature.

The chemical composition of the precipitates is not known. From their contrast behavior it may be concluded that they contain heavy elements.

One element could be Mo (probably associated with nitrogen), which might have diffused into the silicon ribbon from the substrate during ribbon growth and annealing. Microprobe experiments failed to indicate the presence of impurities, since the bulk concentration of these impurities is below the detection limit (in the order of 1000 ppm). A preliminary neutron-activation analysis revealed Au as a trace impurity in the ppb-range. Further experiments are in progress.

Interaction between different defects. In order to complete the description it should be mentioned that different defects occasionally interact to form complicated structures. Some of these interactions have been considered above, a few more examples shall be described. Fig. 9a shows a small twin being intersected by a stacking fault that contains several precipitates. In Fig. 9b the same area is seen edge-on: the trace of the twin can be seen as well as the partial dislocations of the stacking fault. The dislocation at the intersection is imaged as a point only, since its line coincides with the direction of the incident electron beam (along $\langle 110 \rangle$). Fig. 10 shows a cluster of perfect and partial dislocations associated with stacking faults and small dislocation loops. Such structures are rarely encountered and are therefore not expected to influence the material characteristics.

4. Conclusions

The defect structure observed in the present RTR ribbon differs from that of ribbons grown by other techniques, e.g., EFG, predominantly in that it contains a high density of small precipitates ($\sim 1.2 \times 10^{13} \text{ cm}^{-3}$). Precipitates are considered to be very efficient recombination sites for minority carriers; it is to be supposed that the high density impedes the application of this particular ribbon to the production of sufficiently efficient solar cells. This conclusion is corroborated by the experimental experience that we, in spite of repeated efforts, could not produce Schottky diodes on this

material in order to carry out an EBIC investigation. The preparation of the Schottky diode used cleaning and evaporation procedures which yielded good diodes on a variety of other ribbon material of comparable defect structure except for the presence of the small precipitates described. These precipitates and/or the impurity content indicated by their presence may be responsible for the low efficiency of solar cells /6/ fabricated from RTR ribbons.

References

1. L.B. Holt, J. Physique, Colloque C6, 40, 189 (1979).
2. E. Föll and B.O. Kolbesen, Appl. Phys. 8, 319 (1975).
3. H. Strunk and D.G. Ast, submitted to 38. EMSA meeting to be held August 4-8, 1980 in San Francisco.
4. H. Föll and D.G. Ast, 'Planar defects in Silicon', JPL Technical Report, #1, 1979, Contract No. 954852.
5. M.F. Ashby and L.M. Brown, Phil. Mag. 8, 1083 (1963).
6. H.I. Hoo, P.A. Iles and D.P. Tanner, 'Silicon Solar Cell Process Development, Fabrication and Analysis', JPL Technical Report, Contract No. 955089, Optical Coating Laboratory, 1979.

Table 1

Defect structure data extracted from TEM

| Defect type | Density | Size | Remarks |
|-----------------|--------------------------------------|--|---|
| dislocations | $10^6 - 10^7 \text{ cm}^{-2}$ | ---- | Density varies locally. No decoration by precipitates observed. |
| stacking faults | 10^{10} cm^{-3} | $3 \mu\text{m } \phi$ | Density estimated from investigated volume. Order of magnitude only. |
| twinned regions | ---- | thickness typ. 5-100 nm frequent length up to order of mm | Twins ending in matrix infrequent. |
| precipitates | $1.2 \times 10^{13} \text{ cm}^{-3}$ | typ. 10-20 nm wide $\sim 5 \text{ nm}$ thick | Quasi-homogeneously distributed in the ribbon. |

Figure Captions

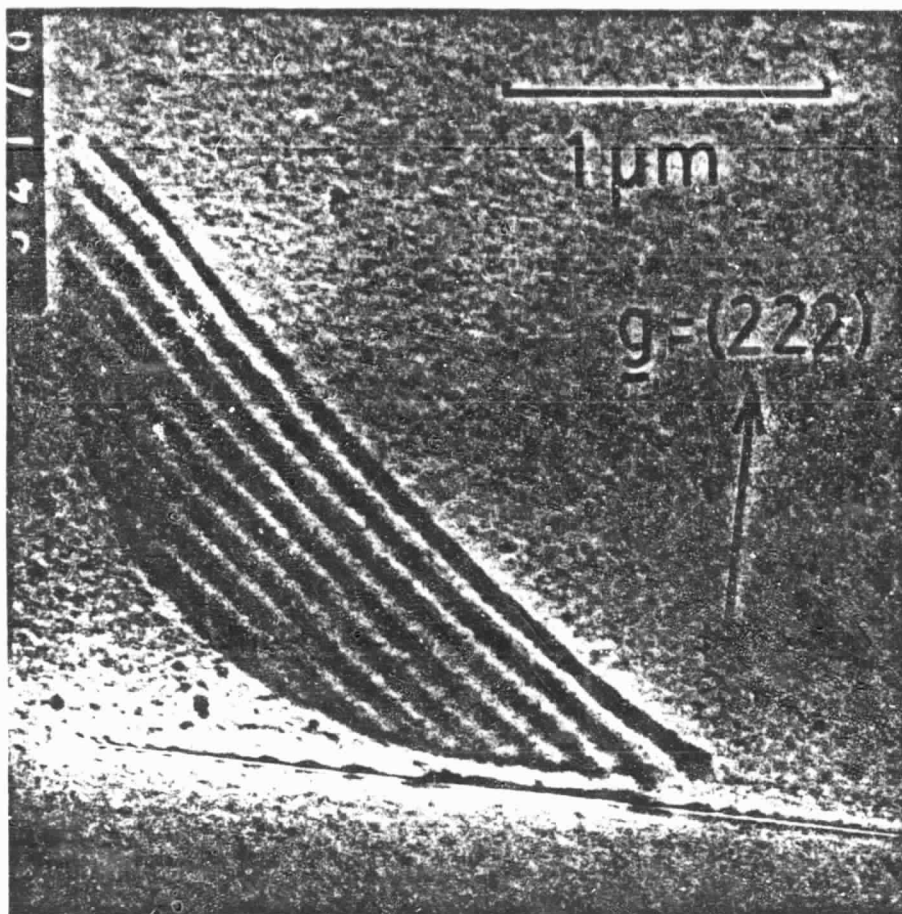
1. Typical dislocation array. g : diffraction vector. The variation in background intensity is due to a varying specimen thickness, which occurs in ion-milling.
2. Two stacking faults inclined in the foil. They are alternately visible in Fig. a and b.
3. Characteristic area containing twin boundaries. Dark field micrograph. The diffraction vector is chosen so that areas with twin orientation relation show up dark and bright. Areas denoted with the same letters A or B have the same orientation. At the right is a twinned area ending in the matrix.
4. End of a microtwin.
5. Lattice dislocations reacting with the boundaries of a thin twin. Note the bright seams near the twin due to preferential etch which occurred during the chemical thinning.
6. Precipitates imaged with different reflections a to d. They cause strong Ashby-Brown contrast except when imaged with a $\{004\}$ -reflection, where they are seen in 'absorption contrast'. Note the improvement in resolution using dark-field weak-beam techniques, compare Figs. e and f with Fig. c.
7. Precipitates with a regular shape. Image is taken along $\langle 110 \rangle$ with many beams excited.

8. a. Regularly and b. irregularly shaped precipitate, imaged with lattice resolution. Note the 'amorphous' looking patches within the precipitates. Insets represent the Si-lattice as projected along an $\langle 110 \rangle$ -direction, the traces of the $\{111\}$ planes are indicated.
9. a. Stacking fault crossing a thin twin. Both are seen inclined to the electron beam by several degrees.
b. Same area, but stacking fault and microtwin seen edge-on. Several precipitates are also present. Bright field. Multibeam along $\langle 110 \rangle$ axis.
10. Complicated arrangement of lattice dislocations, partial dislocations, stacking faults and small dislocation loops. Bright field. Multibeam along $\langle 110 \rangle$ axis.

ORIGINAL PAGE
BLACK AND WHITE PHOTOGRAPH



Fig. 1

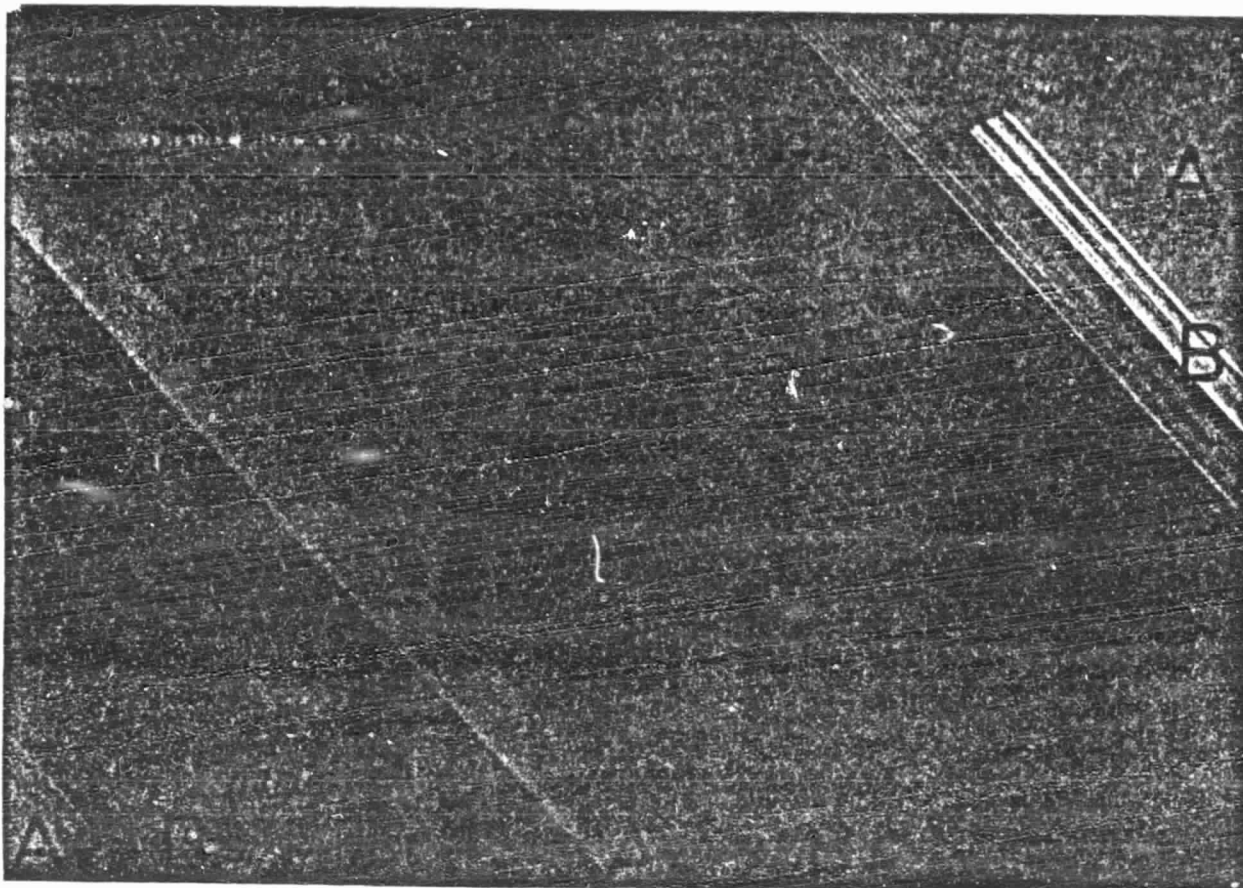


a



b

Fig. 2



ORIGINAL PAGE
BLACK AND WHITE PHOTOGRAPH

Fig. 3

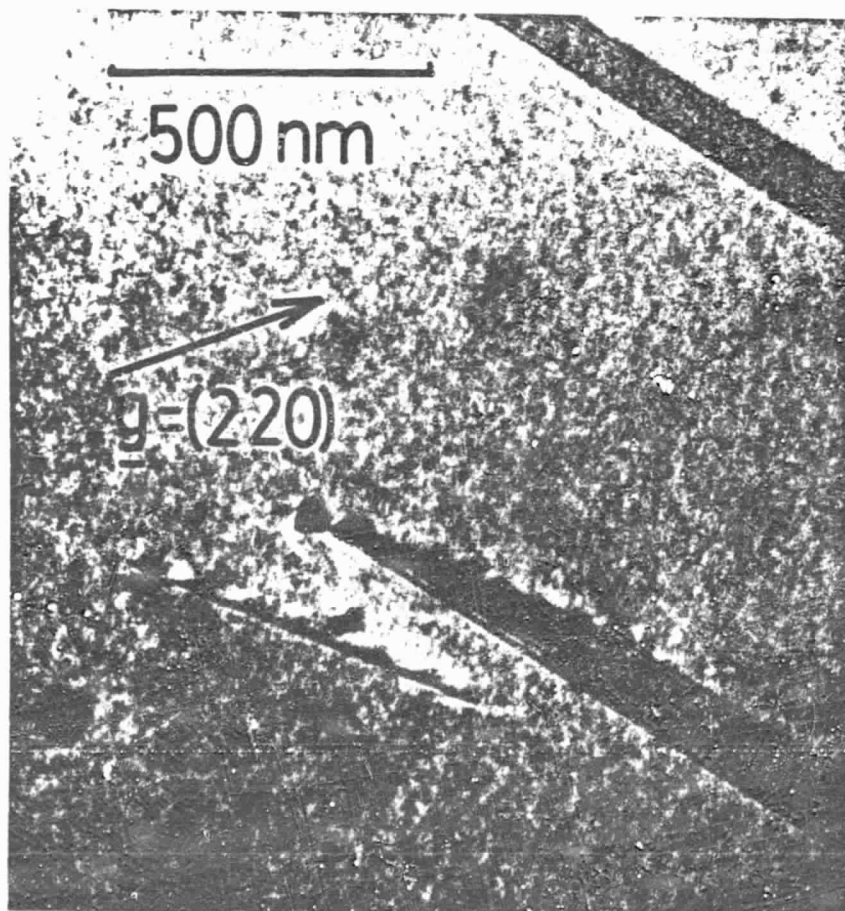


Fig. 4

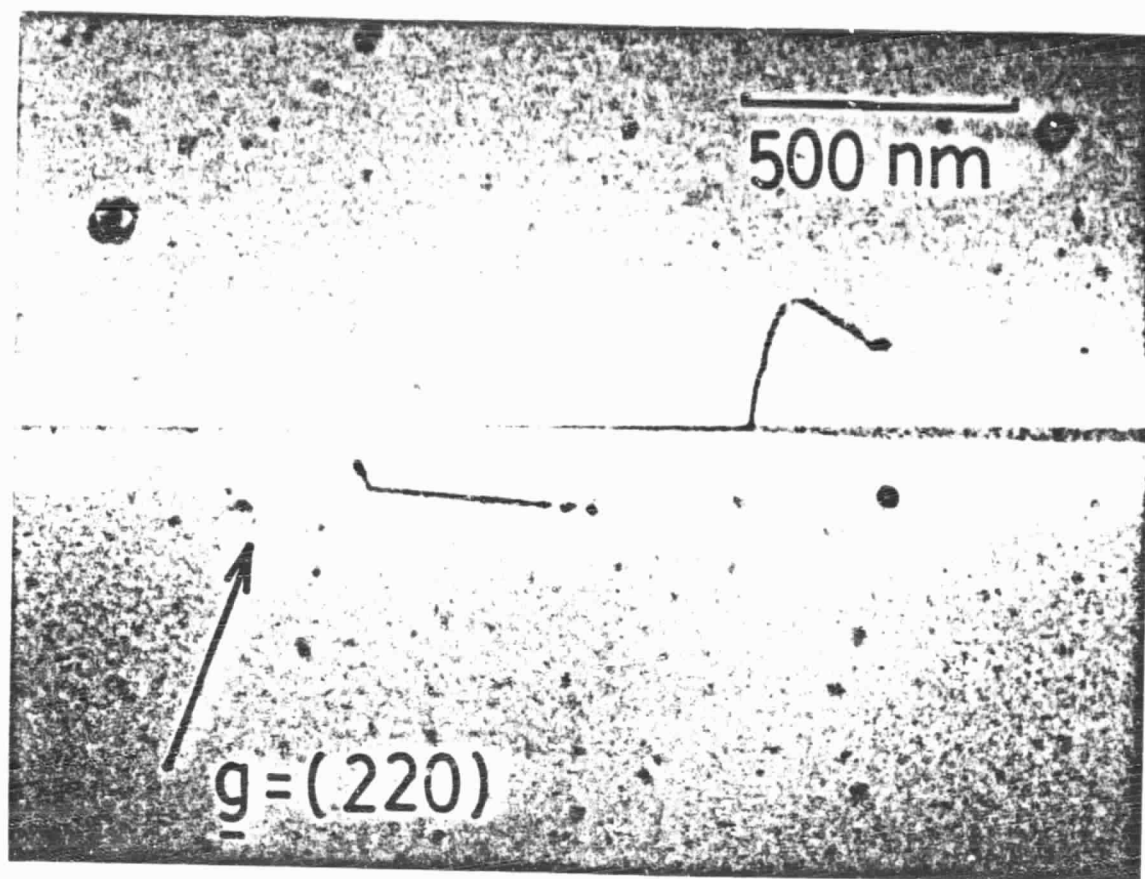


Fig. 5

ORIGINAL PAGE
BLACK AND WHITE PHOTOGRAPH

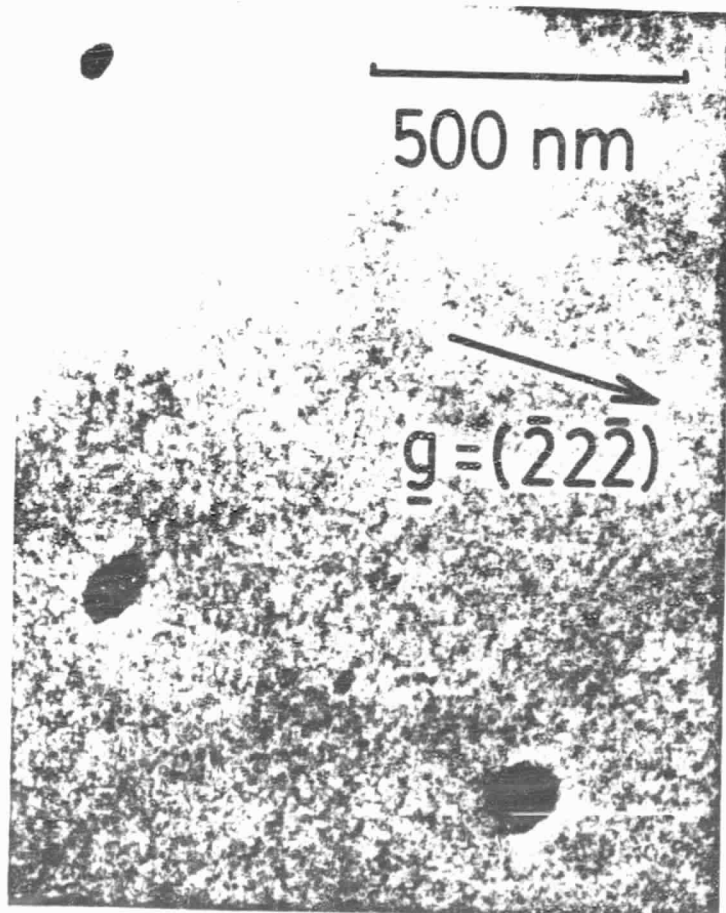


Fig. 6 a

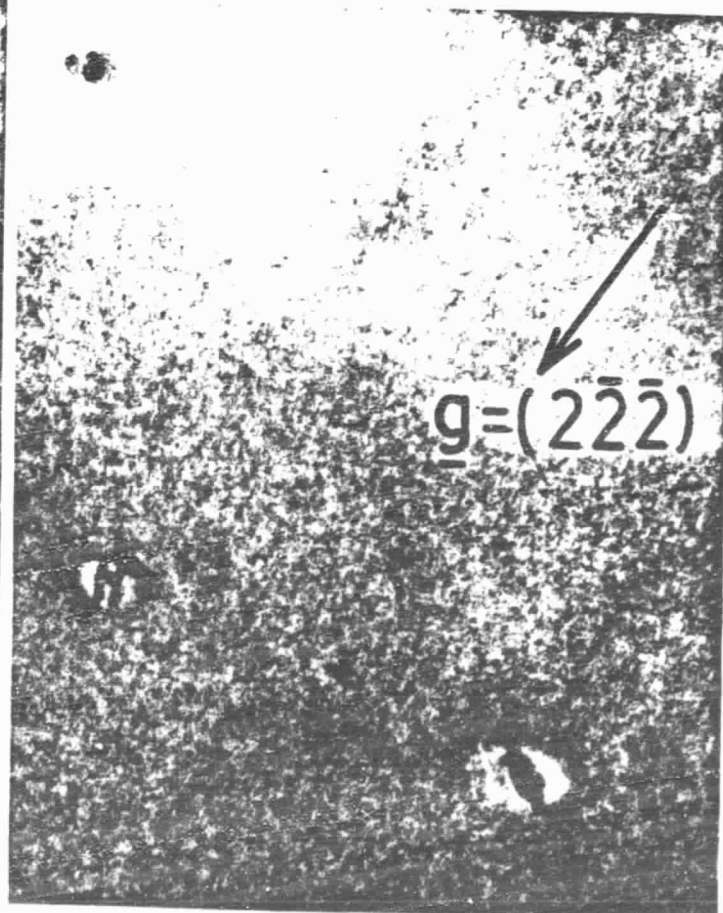
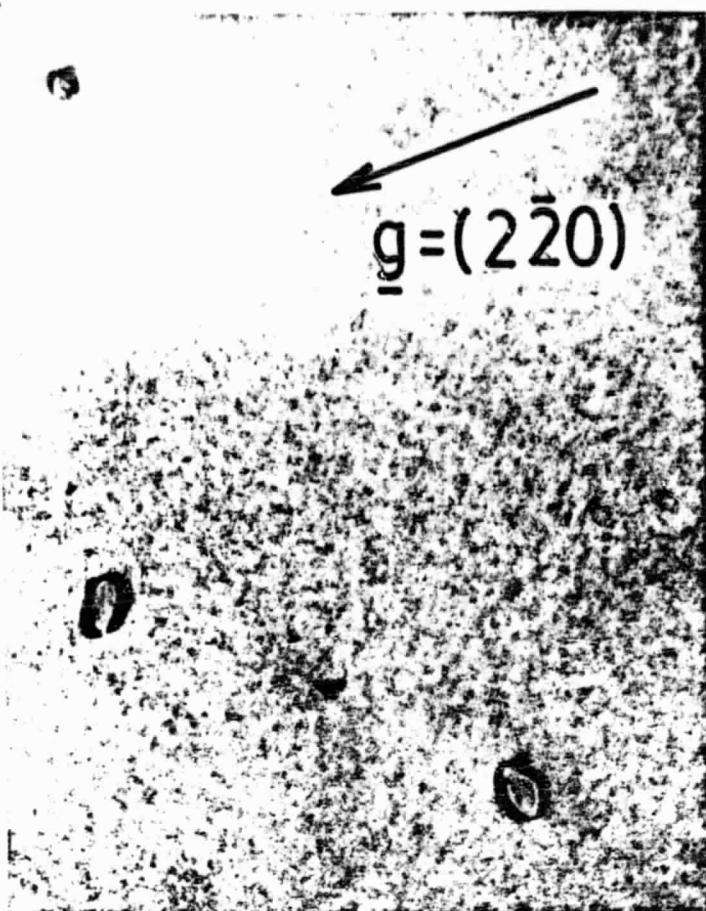
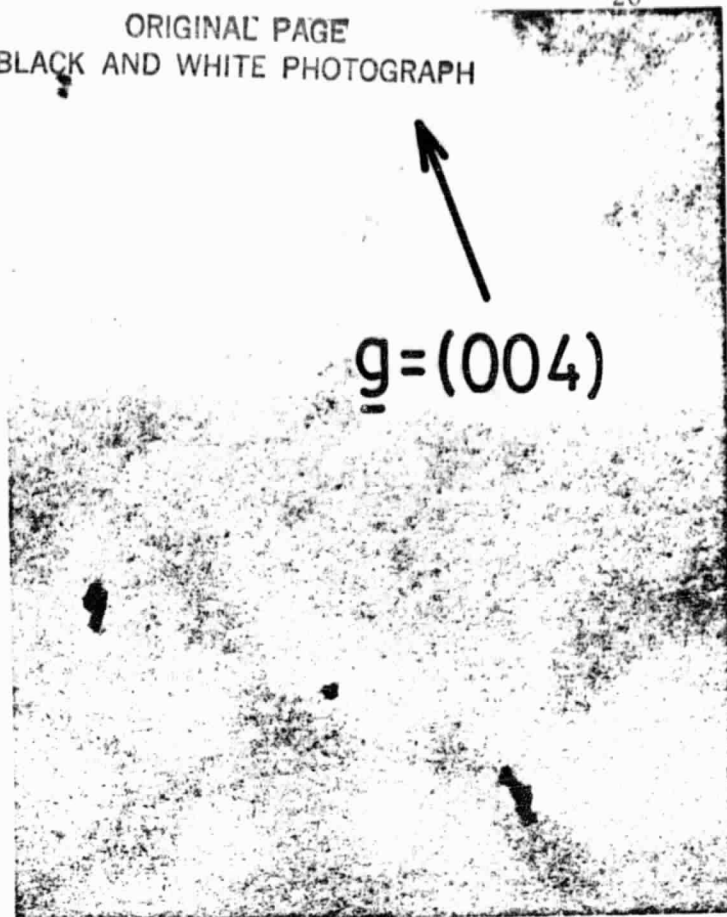


Fig. 6 b

ORIGINAL PAGE
BLACK AND WHITE PHOTOGRAPH



c



d

Fig. 6 c-f



e



f



Fig. 7

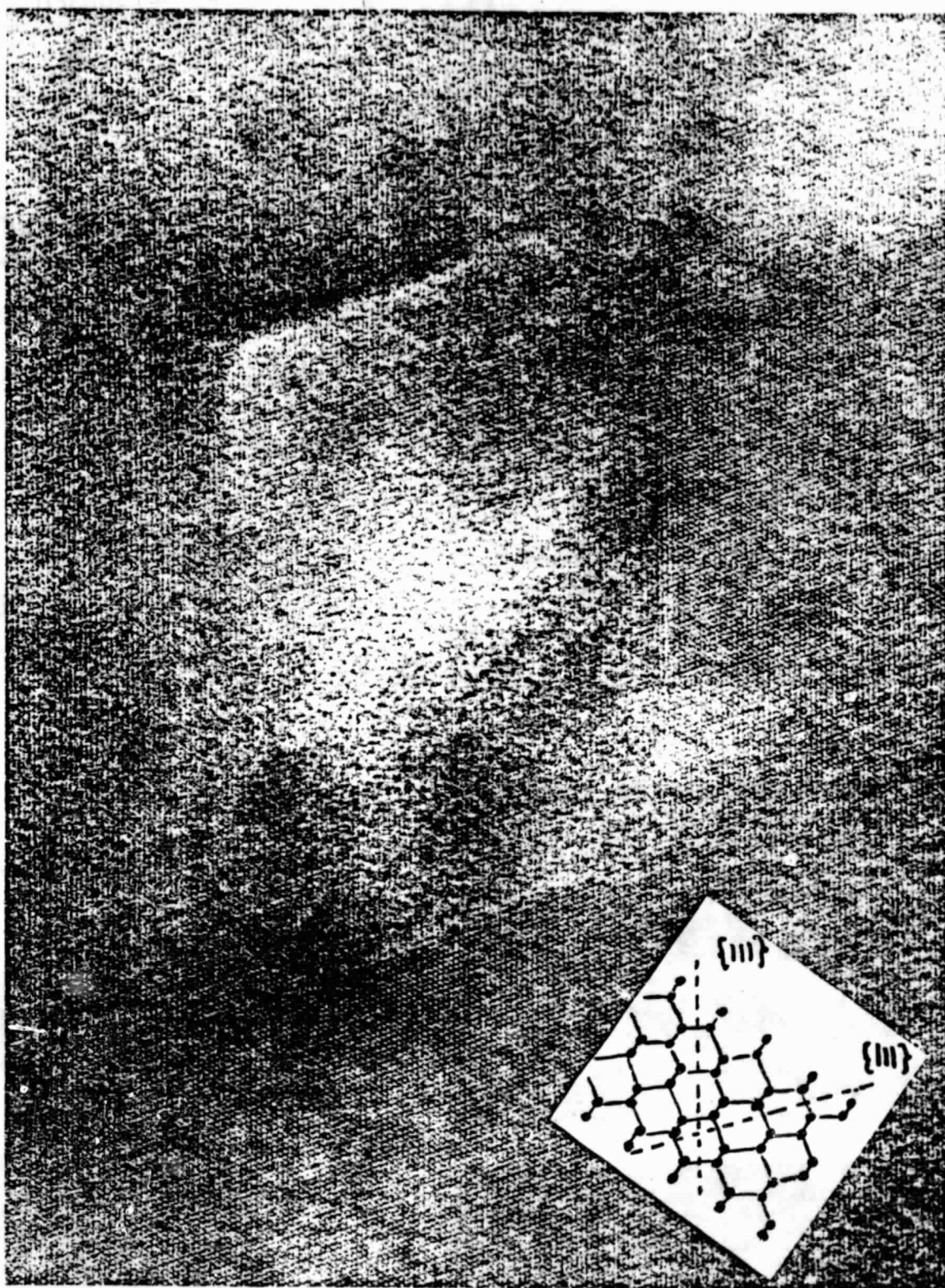
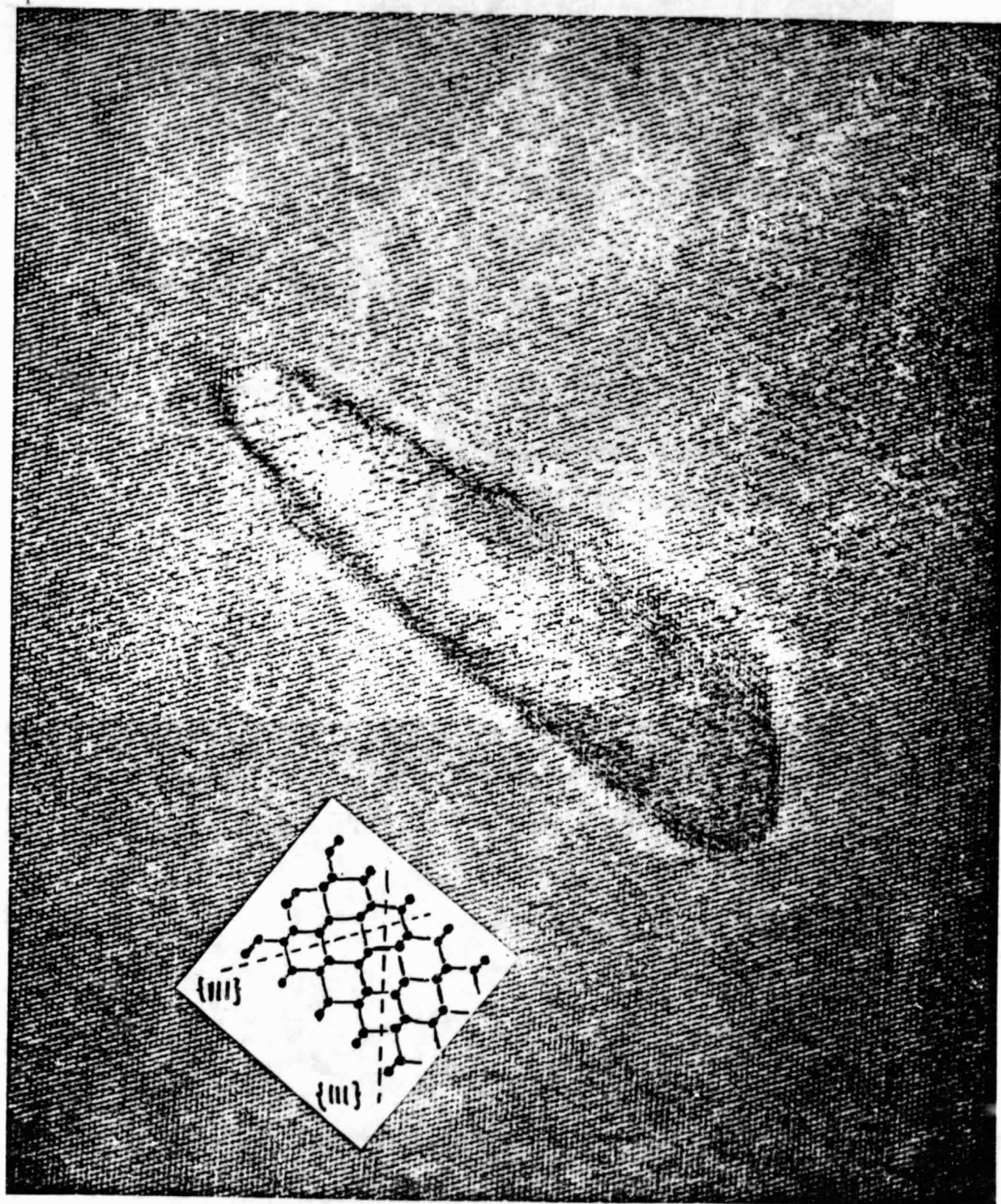


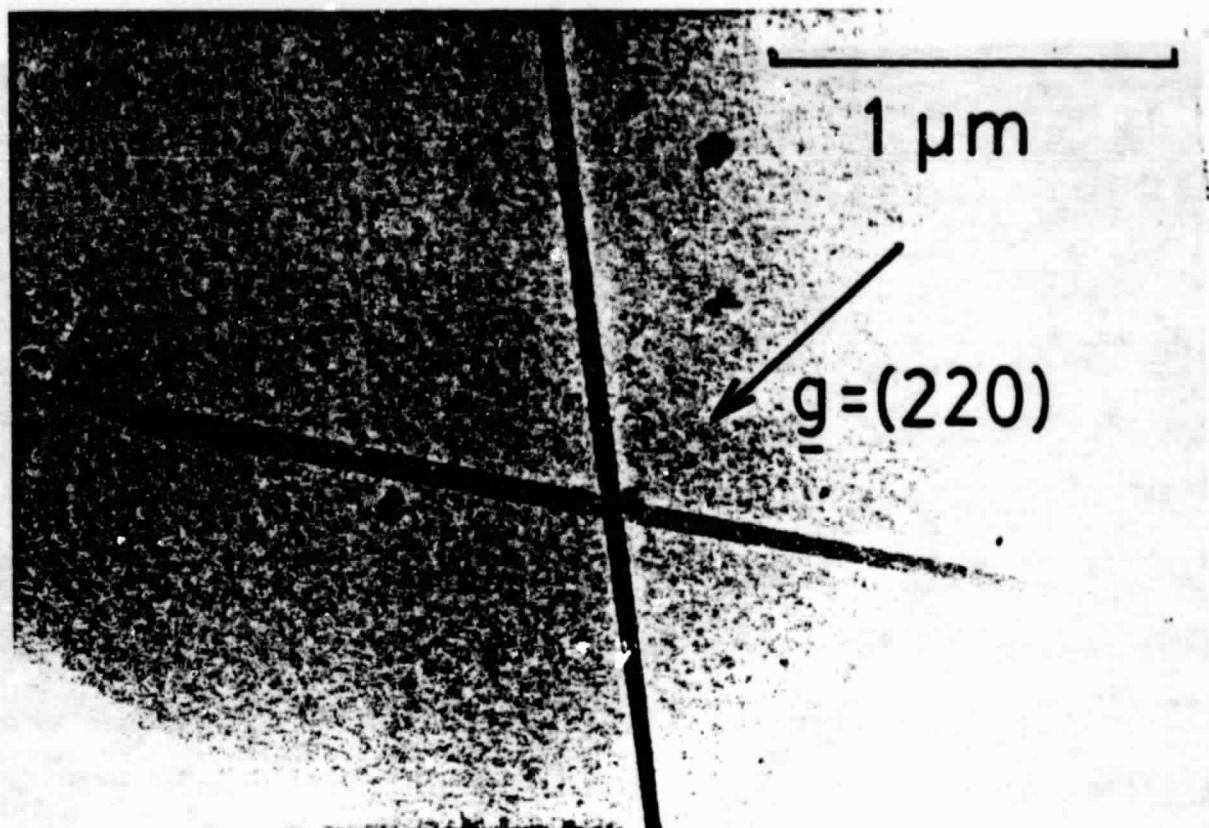
Fig. 8 a

ORIGINAL PAGE
BLACK AND WHITE PHOTOGRAPH



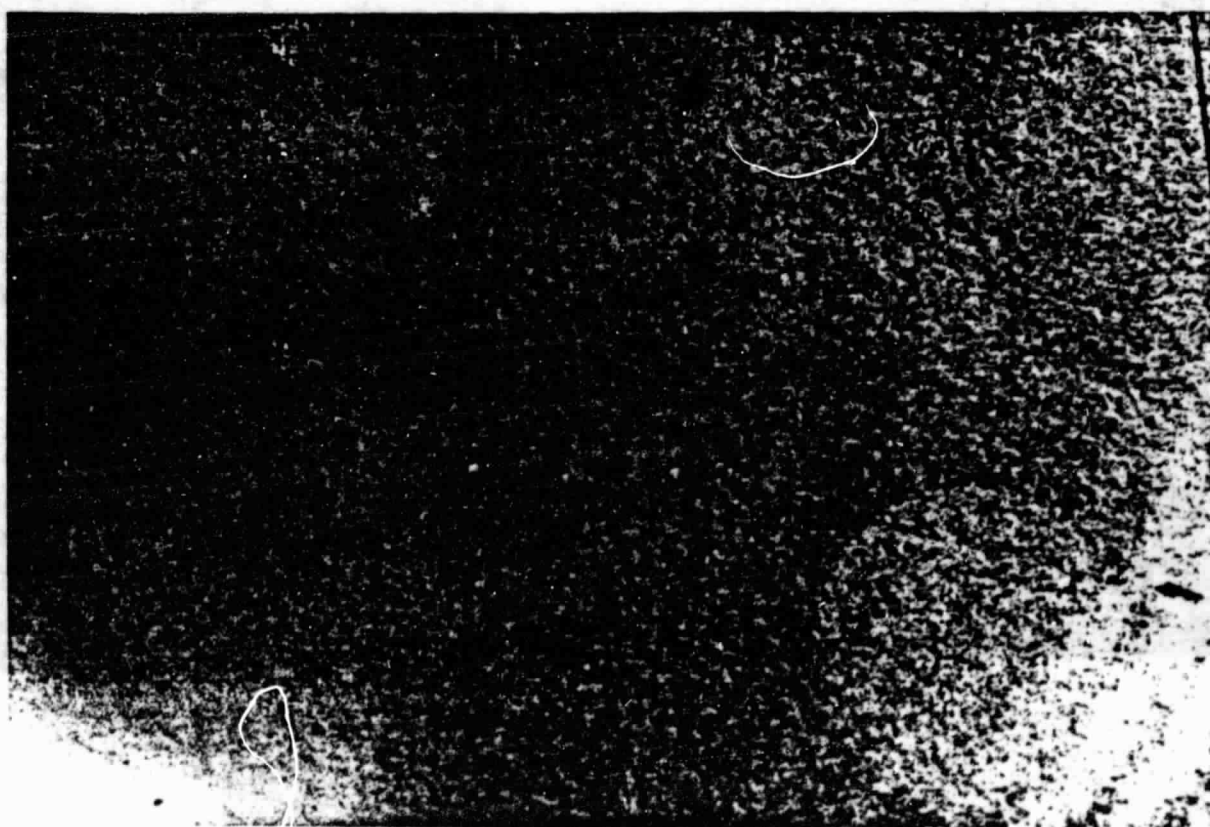
ORIGINAL PAGE
BLACK AND WHITE PHOTOGRAPH

Fig. 8 b



a

ORIGINAL PAGE
BLACK AND WHITE PHOTOGRAPH



b

Fig. 9

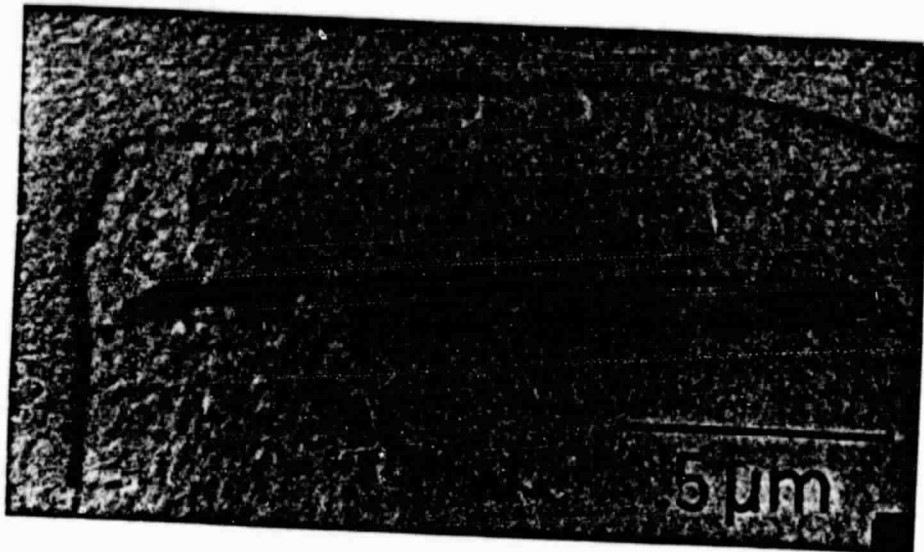


Fig. 10

ORIGINAL PAGE
BLACK AND WHITE PHOTOGRAPH

PRECEDING PAGE BLANK NOT FILMED

THE DEFECT STRUCTURE OF RTR SILICON ; PART II

Abstract

The defect structure of RTR ribbon #6-731, run 803 was studied by CTEM, EBIC and HVTEM. Prior to laser recrystallization the defect structure consists of closely spaced twin and grain boundaries. Precipitation of impurities occurs after laser recrystallization. The observation of electrically active defects in EBIC has been correlated with HVTEM studies "Pairs" of electrically active defects in twin boundaries are due to stacking faults connecting the twin boundaries.

1. Introduction

The following study supplements work previously performed on RTR material, sample identification #6-731, run 803 /1/. The additional studies, carried out on specimens prepared during the original reporting period are: (1) TEM examination of the CVD (chemical vapor deposition) polycrystalline substrate prior to laser recrystallization (2) EBIC studies of the recrystallized substrate and (3) correlation between EBIC and HVTEM observations. A summary of the results presented in Report #4, JPL Contract #554852 "Defect Structure of RTR Silicon Ribbon" will also be given.

2. Previous Work

Table 1 summarizes the defect structure data previously determined by conventional TEM /1/. The high density of precipitates, due presumably to contamination from the Mo substrate used for CVD, was thought to be responsible for the low reported efficiencies of RTR silicon ribbons /2/. In addition, high densities of dislocations and stacking fault loops were observed. Attempts to image these specimens by EBIC (electron beam-induced current) microscopy were unsuccessful. The difficulties encountered in preparing good Schottky diodes were attributed to the high density of precipitates. An interesting observation in the previous study was that the dislocations were not decorated by precipitates. It was proposed therefore that the lattice dislocations were formed after the precipitation process, possibly after the annealing treatment.

3. Experimental Techniques

Scanning electron microscopy in the EBIC mode /3/ was used to characterize the local electrical properties i.e. the minority carrier recombination, at the defects. High voltage transmission electron microscopy (HVTEM) was used to determine the geometrical nature of defects previously imaged by EBIC. Conventional transmission electron microscopy (CTEM) was used to characterize the CVD substrate prior to laser recrystallization.

4. Results

a) TEM Studies of CVD Polycrystalline Silicon Substrate

Figure 1 shows a typical micrograph of the CVD silicon substrate. A large number of closely spaced twin and grain boundaries is observed but only a few lattice dislocations. The most significant observation is the absence of precipitates. The polycrystalline silicon is deposited on a molybdenum substrate which is known to introduce large quantities of Mo into the silicon /4/. This effect should be pronounced in the material used in the present study since no SiO_2 or Si_3N_4 diffusion barrier was used between the Mo substrate and the silicon.

b) EBIC Studies

Although a Schottky diode suitable for EBIC was eventually fabricated on the recrystallized RTR silicon, the quality and resolution were not as good as specimens prepared from other ribbons (e.g. EFG).

Figure 2(a) shows a typical EBIC micrograph from the RTR ribbon. Note that the image is very "noisy". A higher magnification micrograph, Figure 2(b), of the area delineated in Figure 2(a) shows that the horizontal lines are traces of twin or microtwin boundaries and that the EBIC contrast arises from electrically active dislocations in the boundary. There are also a large number of electrically active defects in the matrix material.

c) Correlation of EBIC and HVTEM

The correlation of EBIC and HVTEM requires that the same area be imaged by both techniques. Specimens are mapped out in EBIC and ion milled from the back side until the regions of interest are contained in the electron transparent areas. The present correlation was only partly successful in that the resolution of the EBIC micrographs was not high enough to facilitate an exact 1:1 correspondence with individual dislocations observed in the HVTEM.

Figure 3 shows an EBIC micrograph of active defects distributed along twin boundaries. Part of the area indicated in Figure 3 was imaged by HVTEM, Figure 4.

The twin boundaries are visible through fringe contrast in Figure 4(a). Although the EBIC and HVTEM micrographs cannot be exactly matched one can nevertheless conclude that the density of active defects observed in EBIC is lower than the density of dislocations observed in HVTEM. This observation implies that not all of the dislocations are electrically active.

From HVTEM three distinct dislocation types can be distinguished. (1) Dislocations with no precipitate decoration (2) dislocations decorated with precipitates and (3) dislocations pinned by precipitates. Examples of each of these are shown in Figures 5(a)-5(c) respectively.

Figure 6 shows HVTEM micrographs of stacking faults connecting the two twin boundaries. The stacking faults are out of contrast in Figure 6(b) and the bounding dislocations can be seen. Although the overlapping fringes from the two faults makes it difficult to determine their nature it seems likely that one is intrinsic and one extrinsic. This arrangement preserves the stacking sequence on either side of the faults. Figure 7 is an EBIC micrograph of "pairs" of active defects along the twin boundary imaged in Figure 6. In view of the HVTEM results we propose that the "pairing" is caused by stacking faults between the twin planes and that the contrast is due to the active partials which bound these stacking faults.

5. Discussion

Since no precipitates are observed in the ribbons prior to laser recrystallization, it is reasonable to assume that preferential diffusion takes place along the twin and grain boundaries and that diffusion into the matrix material is limited (during CVD process). During recrystallization the Mo is precipitated out into the matrix. Previous observations /1/ that the lattice dislocations were not decorated by precipitates and that the precipitation process occurs prior to dislocation generation are supported to a certain extent by the present studies. Several dislocations however are decorated, suggesting that some must be generated prior or concomitantly with the precipitation process.

There is indirect evidence that the electrical activity of dislocations depends on the temperature at which they are formed /5/. Formation of dislocations in two temperature regimes (laser recrystallization, post anneal) could therefore explain the observed variability in electrical activity (and also precipitation) at dislocations.

The presence of connecting twins and stacking faults and the corresponding EBIC observations of "pairs" of electrically active defects are interesting fault combinations which also contribute to the reduced efficiencies in RTR ribbons.

References

1. H. Strunk and D. Ast "Defect Structure of RTR Ribbons" JPL Technical Report #4, Contract #954852 (1980).
2. H.I. Hoo, P.A. Iles and D.P. Tanner "Silicon Solar Cell Process Development, Fabrication and Analysis", JPL Technical Report, Contract #955084 Optical Coating Laboratory (1979).
3. H.J. Leamy, L.C. Kimerling and S.D. Ferris, Scanning Electron Microsc., 1, 717 (1978).
4. K.R. Sarma, R.N. Legge and R.W. Gurtler, J. Electronic Materials 2, 841 (1980).
5. H. Strunk, B. Cunningham and D. Ast "Defect Structure of EFG Silicon Ribbon" JPL Technical Report #6, Contract #954852 (1980).

Figure Captions

1. Typical array of twin and grain boundaries in CVD polycrystalline silicon prior to laser recrystallization.
2. (a) EBIC micrograph showing electrical activity along twin boundaries in laser recrystallized RTR silicon.
(b) Higher magnification EBIC micrograph of area shown in (a).
3. EBIC micrograph of electrically active defects in twin boundaries.
4. HVTEM micrographs of part of the area shown in EBIC micrograph of Figure 3. \underline{g} : diffraction vector.
5. HVTEM micrographs showing degrees of precipitation at dislocations (a) "clean" dislocations (b) decorated dislocations (c) pinned dislocations.
6. HVTEM micrographs of stacking faults connecting twin boundaries (a) stacking faults in contrast (b) twin boundaries in contrast.
7. EBIC micrograph of "pairs" of electrically active defects.

Table 1

Defect structure data extracted from TEM

| Defect type | Density | Size | Remarks |
|-----------------|--------------------------------------|--|---|
| dislocations | $10^6 - 10^7 \text{ cm}^{-2}$ | ---- | Density varies locally. No decoration by precipitates observed. |
| stacking faults | 10^{10} cm^{-3} | $3 \mu\text{m } \phi$ | Density estimated from investigated volume. Order of magnitude only. |
| twinned regions | ---- | thickness typ. 5-100 nm frequent length up to order of mm | Twins ending in matrix infrequent. |
| precipitates | $1.2 \times 10^{13} \text{ cm}^{-3}$ | typ. 10-20 nm wide ~5 nm thick | Quasi-homogeneously distributed in the ribbon. |



Figure 1

ORIGINAL PAGE
BLACK AND WHITE PHOTOGRAPH

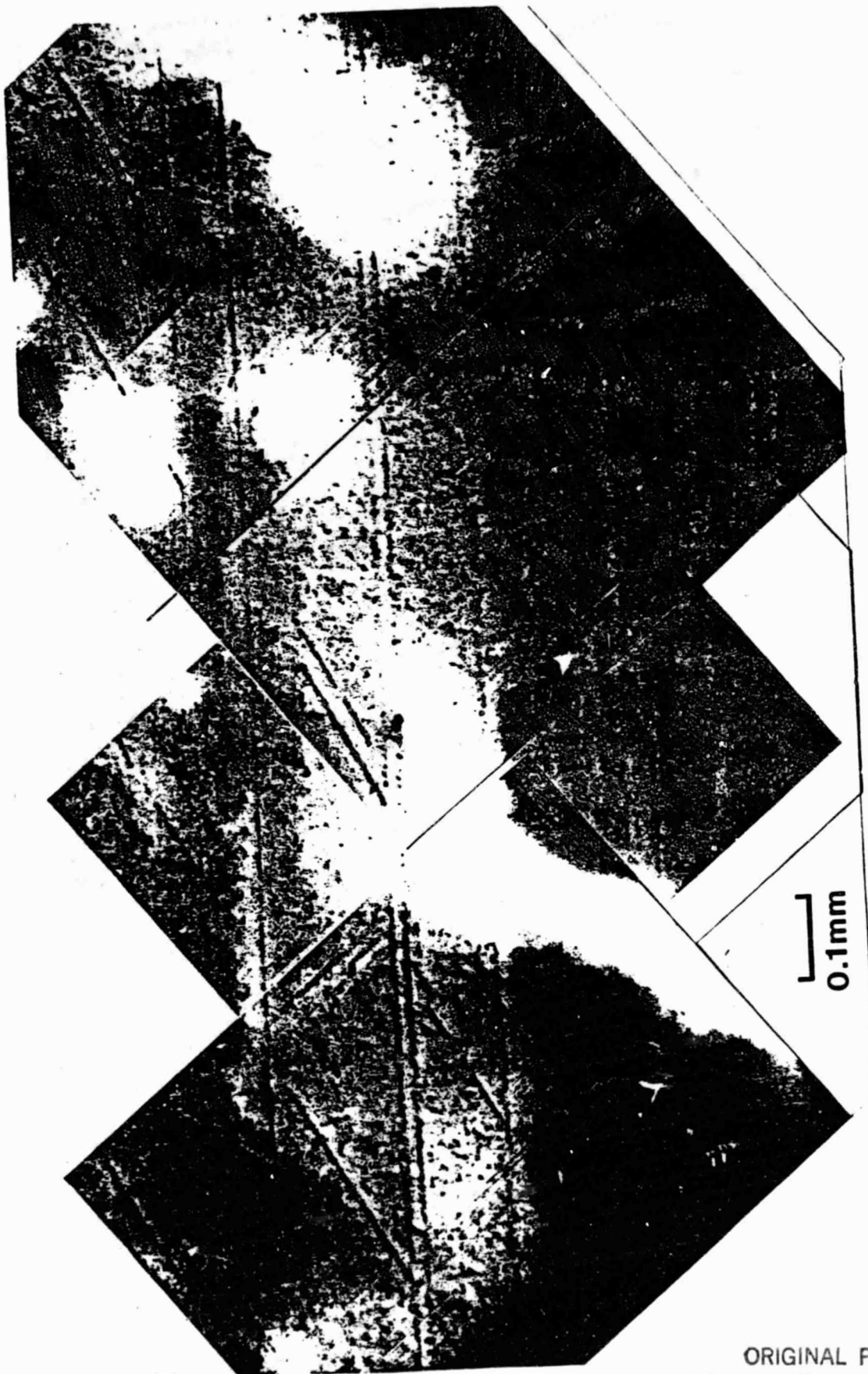


Figure 2(a)

ORIGINAL PAGE
BLACK AND WHITE PHOTOGRAPH

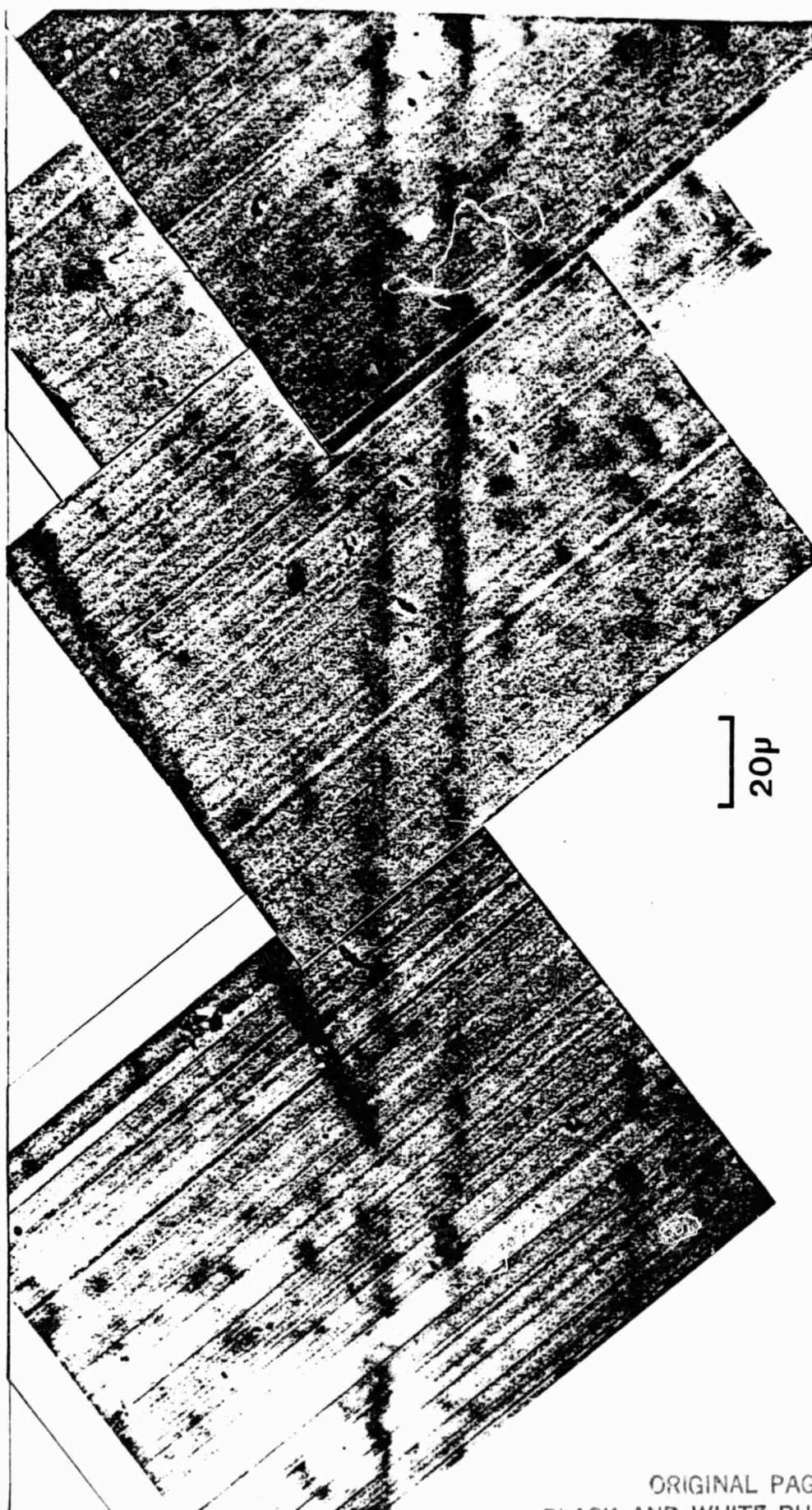


Figure 2(b)

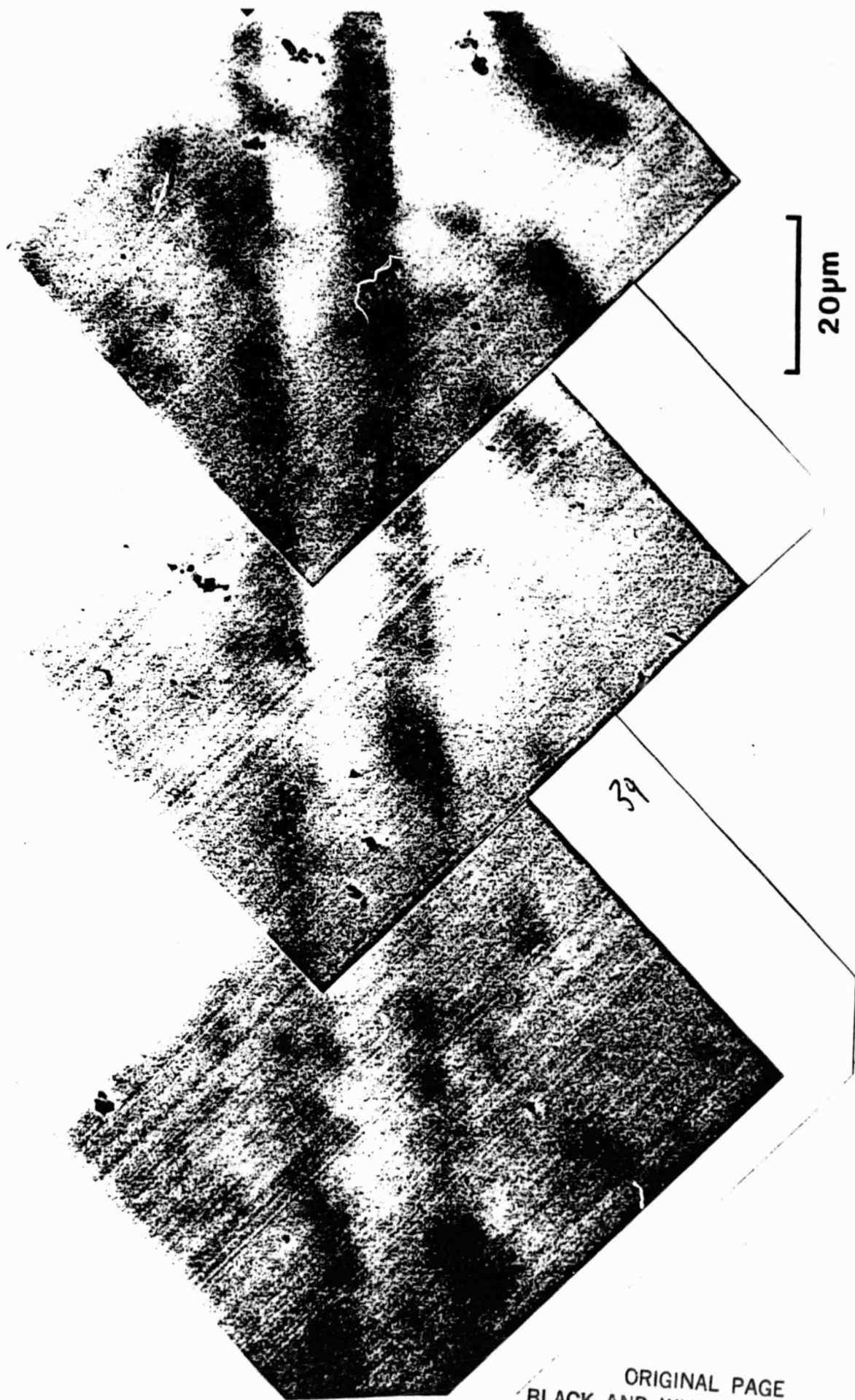


Figure 3

ORIGINAL PAGE
BLACK AND WHITE PHOTOGRAPH

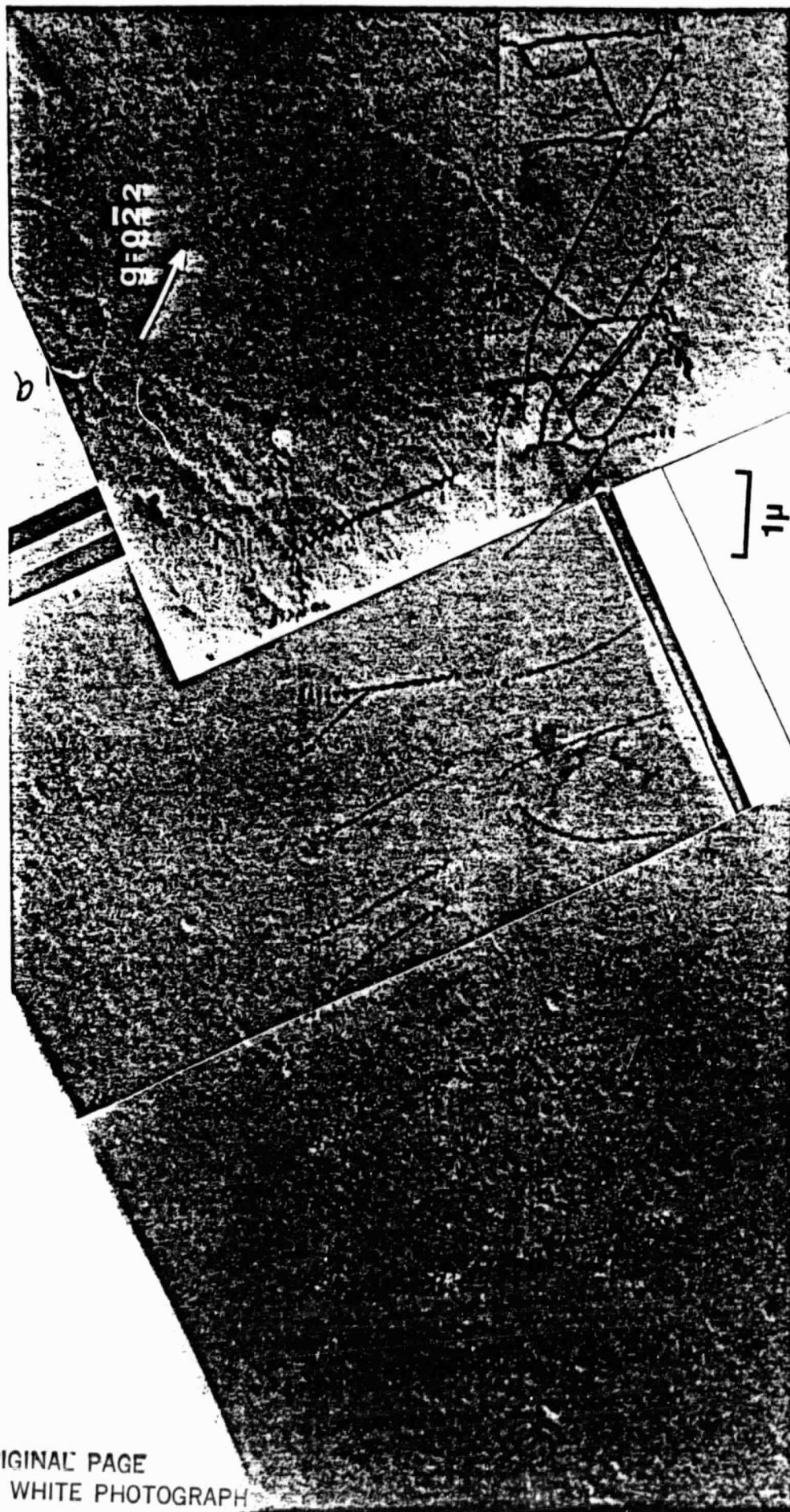


Figure 4

ORIGINAL PAGE
BLACK AND WHITE PHOTOGRAPH

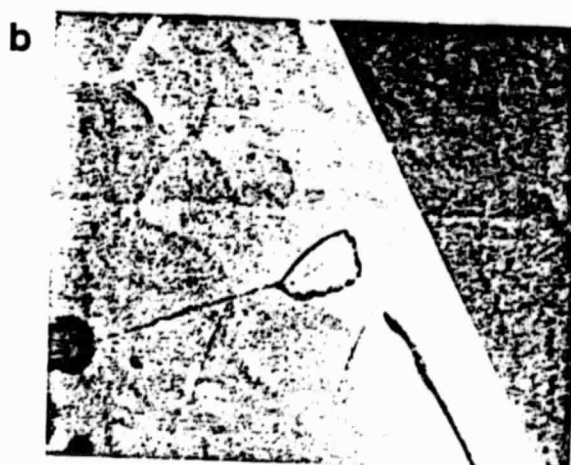


Figure 5

ORIGINAL PAGE
BLACK AND WHITE PHOTOGRAPH

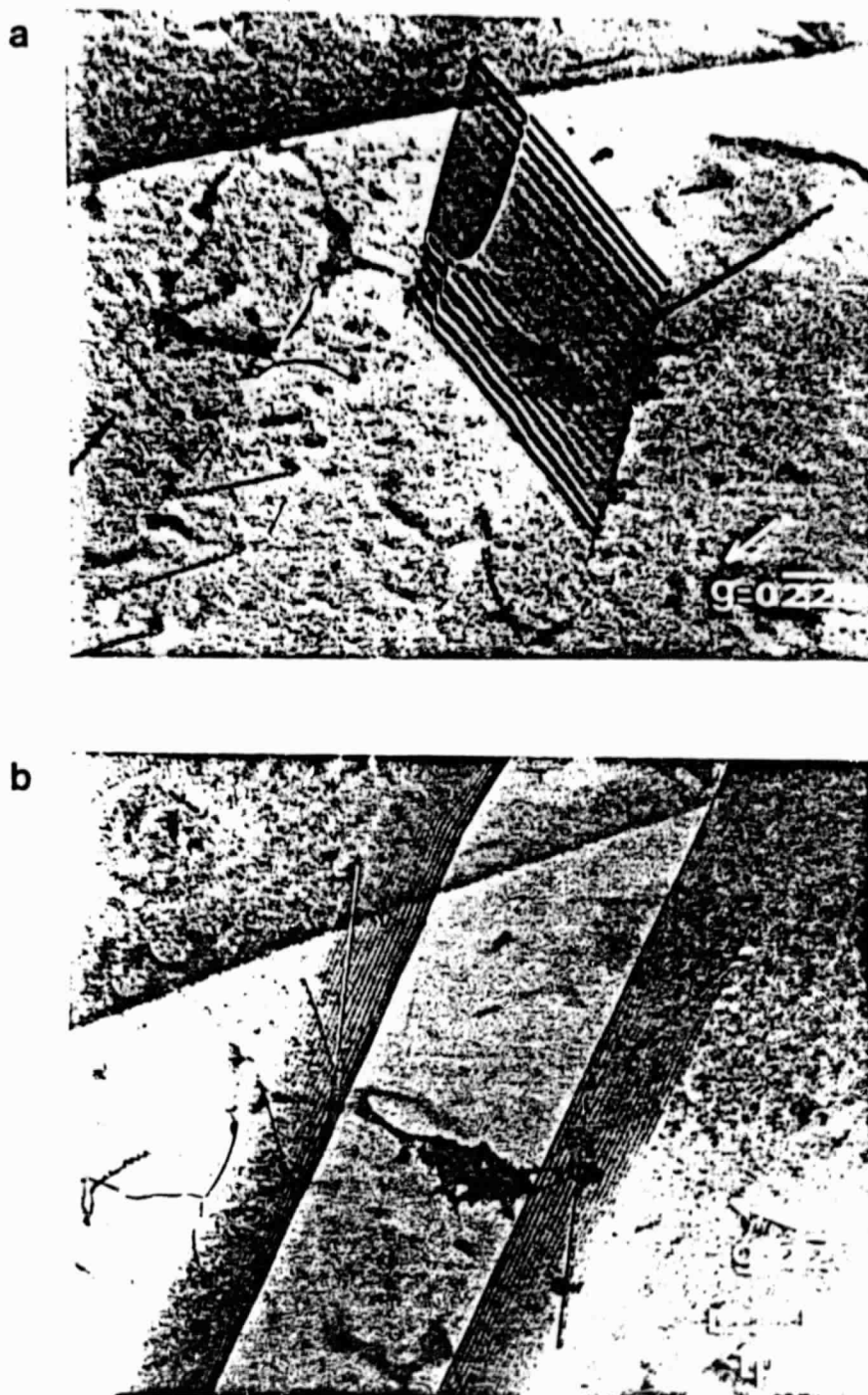
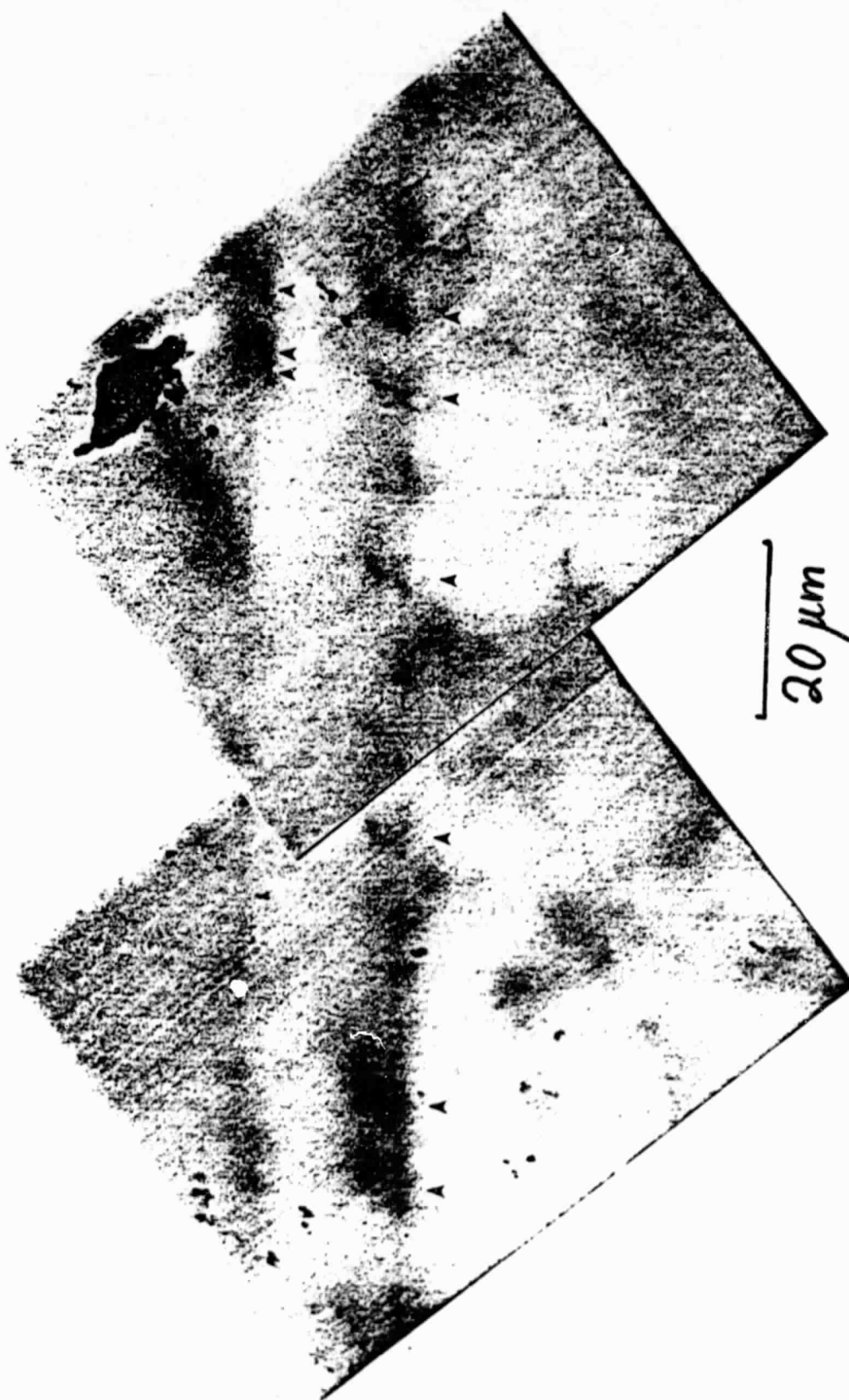


Figure 6

ORIGINAL PAGE
BLACK AND WHITE PHOTOGRAPH



ORIGINAL PAGE
BLACK AND WHITE PHOTOGRAPH

Figure 7

II) DEFECT STRUCTURE OF WEB SILICON RIBBON

ABSTRACT

Web silicon ribbon has recently emerged as a material for the production of high efficiency solar cells. Since defects introduced during growth may influence locally minority carrier recombination rates, there is now a need to examine the defect structure in detail and to correlate it with "electrical activity". This work describes initial observations made on web material by EBIC and HVEM.

Although EBIC investigations have shown that dislocations emerging at the web surface enhance minority carrier recombination rates, their density is low enough (typically 10^5 cm^{-2}) to have only a small effect on the efficiency of the material as a solar cell. Since a condition for dendritic web growth is that the dendrites contain at least two twin boundaries it is usual to find that some of these boundaries extend into the web. These boundaries are formed parallel to the (111) growth surface and are found to be sites of strong electrical activity.

HVEM has been used to study the defect structure at the twin boundary. Two types of dislocation networks lying on different {111} planes have been observed, presumably corresponding to two adjacent twin boundaries. One network consists of an hexagonal array of twin boundary partial dislocations interacting with Lomer-Cottrell locks. The other network is made up of both perfect and partial dislocations running in the $[2\bar{1}\bar{1}]$ growth direction.

1. Introduction

The growth of silicon ribbons by the dendritic web process was first discussed by Dermatis and Faust(1) and O'Hara and Bennett(2) in the early 1960's. The current interest in silicon web is due to its potential use as a substrate material for the economic production of high efficiency solar cells. Seidensticker(3) has shown that the characteristics of solar cells fabricated from dendritic web are virtually identical to those made from the more commonly grown Czochralski material.

Since crystalline defects in semiconductor materials frequently affect the electrical properties, e.g. minority carrier lifetime, the structure and electrical activity of the defects in silicon web were the subjects of the present investigation.

This report summarizes the results of a preliminary study of two Westinghouse dendritic web samples, identification numbers W180-3.4C and J135-3.6.

2. Experimental Techniques

Optical microscopy of chemically etched specimens was used to determine dislocation densities. Samples were mechanically polished, then Secco(4) etched for approximately 5 mins.

High voltage transmission electron microscopy (HVTEM) was used to characterize the crystallographic nature of the defects. The twin planes in web material are parallel to the surface (and at or near the center of the ribbon). The web thickness is only $\sim 150\mu\text{m}$ and, for this reason, it is difficult to prepare a specimen for TEM where the twin boundaries can be viewed end-on. Specimens for the present investigation were therefore thinned as symmetrically as possible from both surfaces with $\text{HNO}_3:\text{HF}:\text{HAc}$ (5:1:1) until a hole with tapered edges was formed. The centrally located twin boundaries were, however, generally not contained in the very thin ($d \lesssim 0.5\mu\text{m}$) annulus around the hole that can be inspected by

conventional (100 keV) transmission electron microscopy. The use of a high voltage microscope (1 MeV) with its large penetrating power of several μm proved to be essential to image the twin plane or planes at the approximate center of the ribbon.

The electronic properties of the material were studied using a scanning electron microscope (SEM) operating in the EBIC mode (electron beam induced current). In this mode the electron beam is used to inject minority carriers which are collected at the specimen surface to form the EBIC image. At regions of enhanced minority carrier recombination the collected current is less than at defect free regions. The images of these points therefore appear dark in the EBIC micrographs.

Finally, a multi-wire, real time Laue back reflection x-ray camera was used to determine twinning relationships in a variety of unthinned web material.

3. Results

a. Web-Dendrite Geometry

The crystallographic orientation of the web and dendrites is shown schematically in Figure 1. The dendrites must contain at least two planes before dendritic growth of a diamond lattice structure can occur(3) and, although it is not necessary, it is common to find some of these twin planes extending into the web. Both the W180-3.4C and J135-3.6 webs were Laue x-rayed to determine the orientation relationship between opposite growth faces. Figure 2 shows an x-ray pattern taken with the beam striking the W180-3.4C web end-on. The (111) twin relationship between opposite faces is evident showing that the web contains an odd number of twin planes. X-ray patterns from the J135-3.6 web determined that this sample contained an even number of twin planes.

b. Defects at the Web Surface

Silicon web J135-3.6 was etched and optical micrographs taken at various positions across the surface. These are shown in Figure 2 together with a sketch of the web surface indicating the areas corresponding to the micrographs. Figure 3 (j) shows the relationship between position and etch-pit density. The density is $\sim 5 \cdot 10^5$ in the center of the web dropping to $\sim 5 \cdot 10^4$ at the edges. It is generally accepted(5,6) that most of the dislocations in silicon webs originate from highly strained regions in the dendrites, caused by liquid entrapment during growth. Such a region is shown in Figure 4, with the slip plane traces clearly visible. The maximum of about $5 \cdot 10^5$ dislocations per cm^2 observed in Figure 3(j) is due to thermal stresses generated during growth causing most of the dislocations to slip into the center of the web. If the stresses generated at a dislocation source are insufficient to promote slip, then these dislocations will remain at regions close to the dendrites. This explains the secondary maxima observed in Figure 3(j).

Figure 5 shows an EBIC micrograph of the web surface. The dark spots on the micrograph are caused by enhanced minority carrier recombination at dislocations inclined to the surface. The density of electrically active defects observed in EBIC is the same as the etch-pit density observed in optical microscopy, suggesting that most, if not all, of the dislocations intersecting the web surface are electrically active. Solar cells with relatively high efficiencies have been fabricated from silicon web containing dislocation densities of the order of magnitude observed in the present study(7), indicating that either the electrical activity associated with these defects is not strong enough to significantly detract from cell performances or that the defect densities are at a tolerable level.

c. Electrical Activity at the Twin Planes

The electrical activity of the twin boundaries was studied by beveling and polishing a specimen (J135-3.6) at a shallow angle, $1-2^\circ$, to the growth surface. EBIC, see Figure 6, shows that a high density of dislocations is concentrated at the twin boundaries and that in this region strong minority carrier recombination processes occur. It is thought that the thermal stresses generated during growth also cause dislocations to slip to the interior of the web, where the twin planes act as obstacles to further slip processes. Figure 7 is an optical micrograph of the same area as the EBIC image after the specimen had been etched to remove the Schottky diode and delineate the defect. As in the case of dislocations at the web surface, there is a close agreement between the density of dark EBIC features in Figure 6 and the optical etch pit density in Figure 7. A direct correspondence between Figures 6 and 7 is not possible since the etching process removes several μm of material from the surface. Both EBIC and optical micrographs show that two twin boundaries exist in the web, i.e., a microtwin, and that the dislocation density on one side of the microtwin is higher than on the other.

The fine line marked A in Figure 6 is thought to be a small angle grain boundary; however, this has not yet been confirmed. The width and contrast features are not typical of surface scratches normally visible in EBIC micrographs and the contrast is probably due to the surface topology rather than to an associated electrical activity. Laue x-ray diffraction patterns from either side of the line failed to reveal any difference in orientation, indicating that, if the observed feature is indeed a low-angle boundary, the mismatch is $<1^\circ$. Similar features have been observed by the authors in other web specimens where they are visible on the surface faces.

Figure 8 shows an EBIC micrograph taken from silicon web material W180-3.4C, where the dislocations are almost surface parallel. The dislocations are centered around the active boundary shown in the middle of the micrograph. This is probably a twin boundary which has been forced out of the web during growth. The dislocations associated with it are also strongly electrically active.

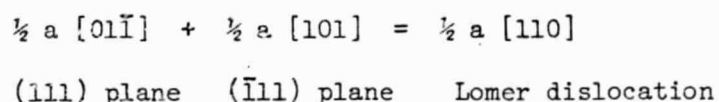
d. Defect Structure at the Twin Planes

Previous investigators(8) identified the defect structure of twin boundaries in silicon web as complicated arrays of dislocations displaying $\langle 110 \rangle$ Burgers vectors, with the dislocation lines primarily directed along $[2\bar{1}\bar{1}]$ and $\langle 110 \rangle$ directions. The present study has confirmed the existence of these dislocations and in addition has identified two sets of misfit dislocations. Figures 9(a) - 9(d) are HVEM micrographs of web J135-3.6 showing an hexagonal array of twin boundary dislocations imaged with different diffraction conditions. From contrast analysis the Burgers vectors of these dislocations were determined as being of the $\langle 211 \rangle$ type. Each set can be extinguished by using the appropriate $\{220\}$ reflection. The observed Burgers vectors are in agreement with the prediction of the Bollman theory(9), that intrinsic dislocations in coherent twin boundaries are Shockley partials, $b = 1/6 \langle 211 \rangle$. These dislocations take up a small twist component in the (111) twinning plane. The twin relationship could be easily verified from selected area diffraction. The twist component estimated from $\theta = \frac{|b|}{d}$ is in the order of 0.01° and is therefore too small to be detected by electron diffraction. The second set of misfit dislocations, Figure 10, consists of slightly curved dislocations running in the $[2\bar{1}\bar{1}]$ direction. They are also contained in a (111) twin plane and take up a small tilt component. Most of these dislocations are 60° partials having Burgers vectors $= 1/6[\bar{1}2\bar{1}]$, all of the same sign of b as revealed by $+g$, $-g$, while others are perfect dislocations with Burgers vectors of $\frac{1}{2}[0\bar{1}\bar{1}]$, 90°

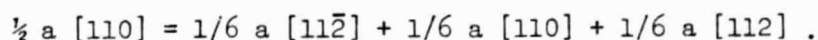
Based on the original Microfiche, multiple pages appear to be
missing from this document

and $\frac{1}{2}[1\bar{1}0]$, 30° . The diffraction vector in Figure 10(6) was chosen such that the partials were out of contrast. O'Hara and Schwuttke, using a large area scanning oscillator technique (SOT) identified the edge and 30° perfect dislocations but did not resolve the 60° partials. They also reported dislocations with Burgers vectors $[101]$ and $[110]$ type lying in the $[2\bar{1}\bar{1}]$ direction, although they also noted that such dislocations should not slip readily, as opposed to the ones reported above.

Figure 10 also shows straight dislocations running in the $\langle 110 \rangle$ directions, and part of an hexagonal network similar to that shown in Figure 9. Stereo micrographs show that these dislocations are not contained in the same (111) plane as the curved dislocations and must therefore belong to another twin plane, i.e., the other side of a microtwin. A strong interaction occurs between the dislocations running in the $\langle 110 \rangle$ directions and the network of partials. The straight dislocations have $\langle 110 \rangle$ type Burgers vectors and are edge sessile. They form when dislocations slipping on either $(1\bar{1}1)$, $(11\bar{1})$ or $(\bar{1}11)$ planes intersect dislocations in the twin planes and form Lomer sessile dislocations. O'Hara and Schwuttke proposed that the reaction for dislocations slipping on the $(\bar{1}11)$ plane would be



The $\frac{1}{2} a [110]$ Lomer dislocations, shown in Figure 10, lying along the $[1\bar{1}0]$ direction, can then dissociate into a Cottrell-Lomer lock by the following reaction.



It is likely that the dissociated partials are responsible for the interactions with the hexagonal network.

Similar reactions occur for dislocations slipping on the $(1\bar{1}1)$ and $(11\bar{1})$ planes with the resulting Lomer dislocations having Burgers vectors $\frac{1}{2}a [011]$ and $\frac{1}{2}a [101]$ and line directions $[01\bar{1}]$ and $[\bar{1}01]$ respectively. Whereas O'Hara and Schwuttke identified dislocations directed along $[1\bar{1}0]$ and $[10\bar{1}]$, the present investigation has identified Lomer dislocations lying in all three of the $\langle 110 \rangle$ directions contained in the (111) twin plane.

In both the etch and EBIC studies it was noted that the dislocation density was higher on one side of the microtwin than on the other. The HVEM studies have also shown that most of the dislocation reactions occur on one of the twin planes. It is likely that an inhomogeneous stress distribution is present in the material during growth, e.g. by buckling of the web.

4. Conclusions

The present study has shown that the defect structure in silicon web enhances minority-carrier recombination rates. The dislocations in the bulk of the material are electrically active. Empirically it is known that this activity does not significantly reduce the characteristics of solar cells. Since complete devices have not yet been investigated it is not known if the defect density is simply too low or if annealing reduces the electrical activity of dislocations(10). The surface parallel twin boundaries typical of this material are associated with a high density of dislocations. EBIC shows that these dislocations are sites of high minority carrier recombination and a reduction in solar cell efficiency is therefore expected when twin boundaries lie in the active region of a solar cell.

The defect structure of the twin planes has been investigated using HVEM and several dislocation-types not previously reported in this material have been identified.

REFERENCES

1. S. N. Dermatis and J. W. Faust, "Silicon Sheets for the Manufacture of Semiconductor Devices", I.E.E.E. Trans. Communications Electronics 05, 194 (1963).
2. S. O'Hara and A. I. Bennett, J. Appl. Phys. 35, 686 (1964).
3. R. G. Seidensticker, J. Cryst. Growth 39, 17 (1977).
4. F. Secco d'Aragona, J. Electrochem. Soc. 119, 948 (1972).
5. S. O'Hara, J. Appl. Phys. 35, 409 (1964).
6. D. L. Barrett, E. H. Myers, D. R. Hamilton and A. I. Bennett, J. Electrochem. Soc. 118, 952 (1971).
7. C. S. Duncan et al., "Silicon Web Process Development", JPL Technical Report, Contract No. NAS 954654, #78/1, Westinghouse R&D Center, 1978.
8. S. O'Hara and G. H. Schwuttke, J. Appl. Phys. 36, 2475 (1965).
9. W. Bollman, Crystal Defects and Crystalline Interfaces, Springer Verlag, New York (1970).
10. H. Alexander, J. Physique Colloq. 40, C6-1 (1979).

ORIGINAL PAGE IS
OF POOR QUALITY

FIGURE CAPTIONS

1. Schematic showing the crystallographic orientation of web-dendritic silicon.
2. Back reflection Laue x-ray pattern showing twin relationship in web material.
3. Optical micrographs of etch pits.
4. Optical micrograph of a dislocation source.
5. EBIC micrograph of a web surface.
6. EBIC micrograph of a bevelled surface showing electrical activity near twin boundaries.
7. Optical micrograph of same region as shown in Figure 6.
8. EBIC micrograph of surface-parallel dislocations.
9. HVTEM micrographs of a dislocation network, g : diffraction vector.
10. HVTEM micrographs (see text for details).

ORIGINAL PAGE IS
OF POOR QUALITY

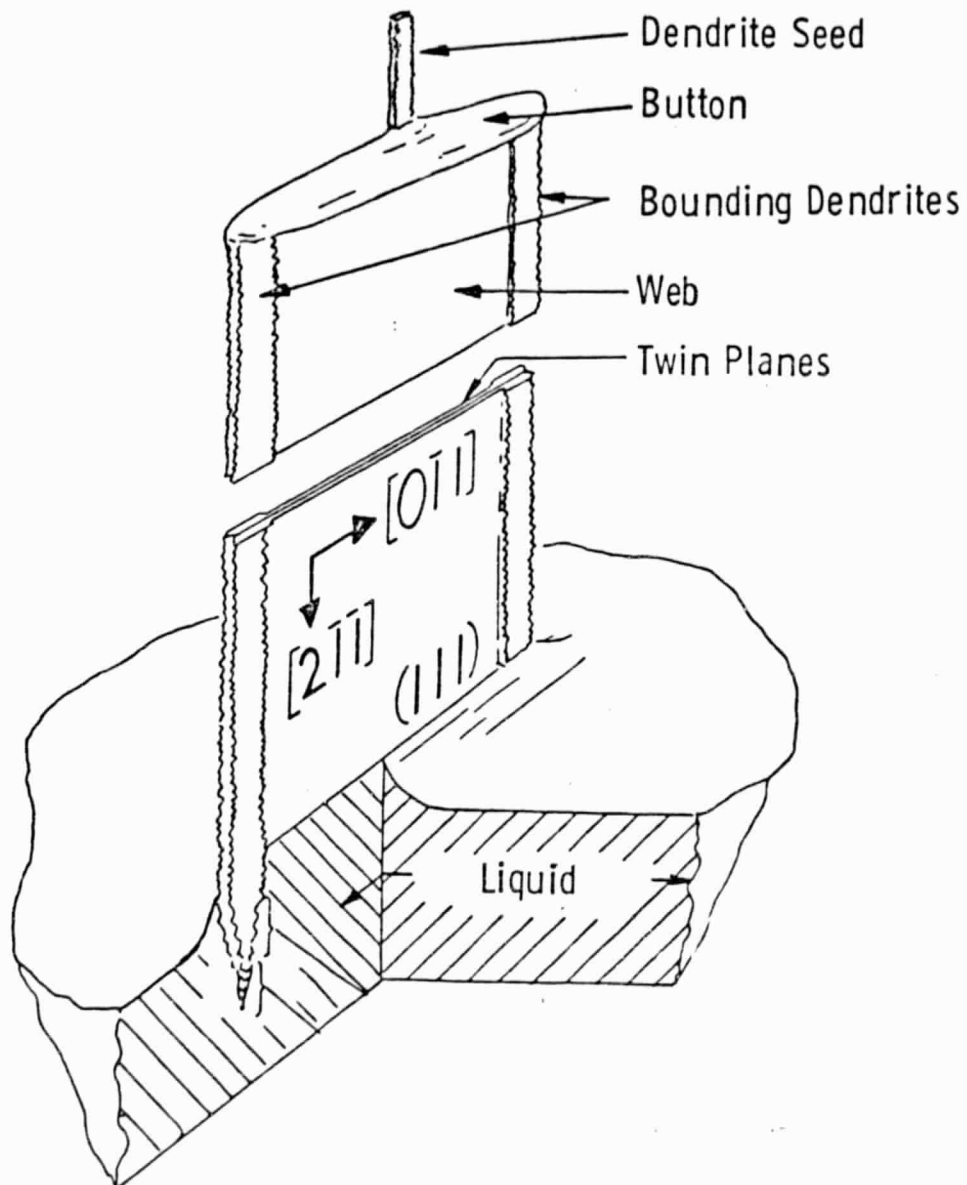


Figure 1 Schematic Section of Web Growth

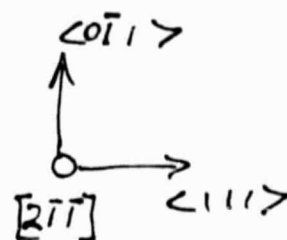
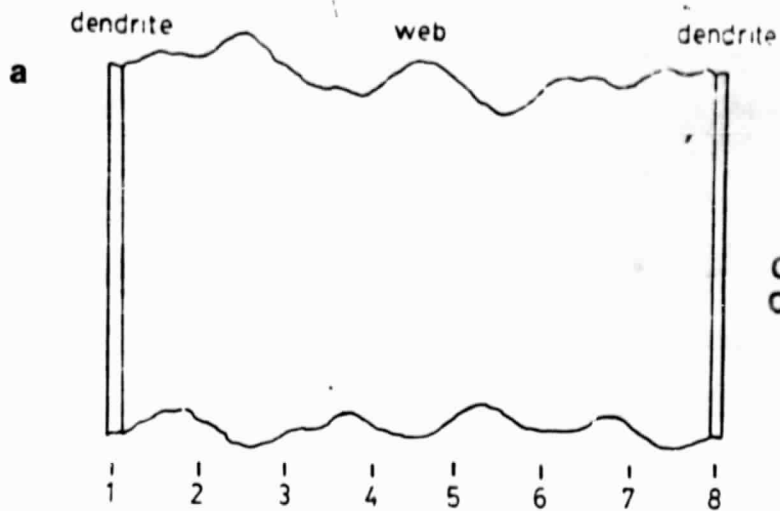


Figure 2 Laue X-ray pattern.

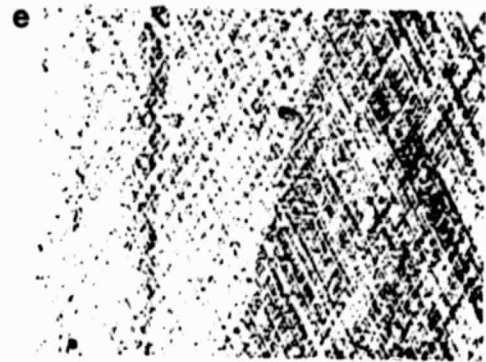
ORIGINAL PAGE
BLACK AND WHITE PHOTOGRAPH



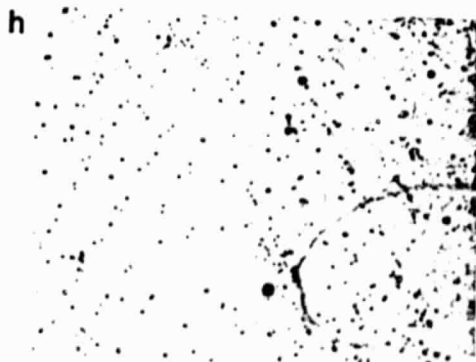
ORIGINAL PAGE IS
OF POOR QUALITY



3



4



7

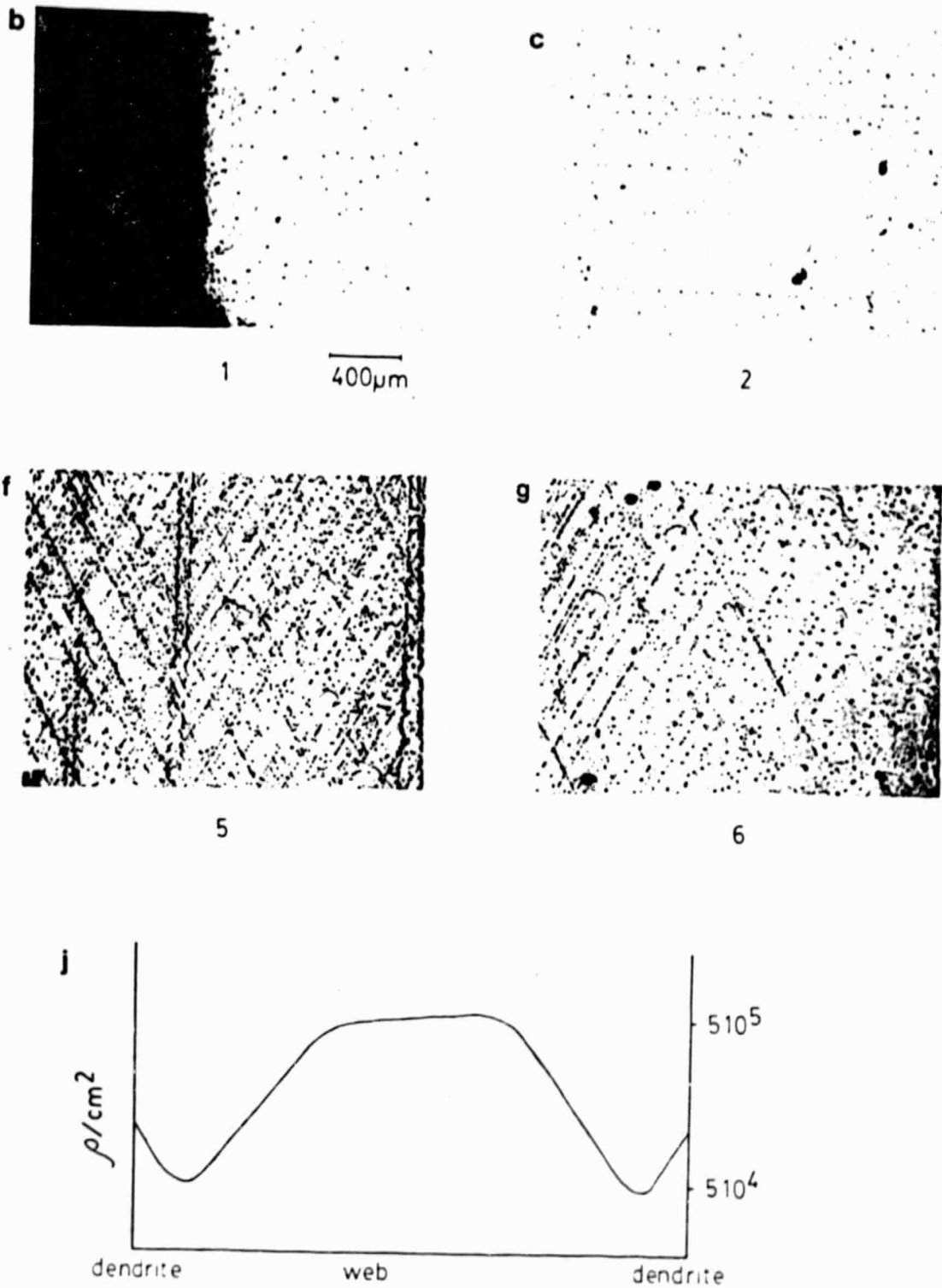


8

Dislocation etch pits in web-dendritic silicon

Fig.3

B Cunningham / DG Ast



Dislocation etch pits in web-dendritic silicon

Fig.3

B Cunningham / D G Ast

ORIGINAL PAGE IS
OF POOR QUALITY

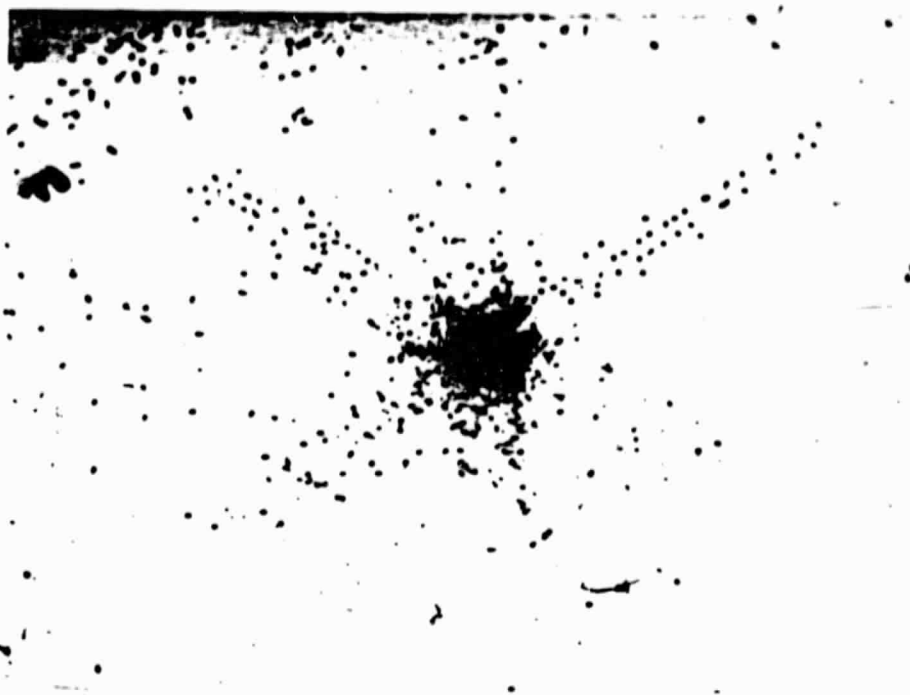



Fig. 4


100 μ m

ORIGINAL PAGE IS
OF POOR QUALITY



Fig.5



20μm



Fig. 7

100 μ m

**ORIGINAL PAGE IS
OF POOR QUALITY**



Fig. 6

50 μ m

ORIGINAL PAGE IS
OF POOR QUALITY



100μm

Fig. 8

ORIGINAL PAGE
BLACK AND WHITE PHOTOGRAPH



Fig. 9

ORIGINAL PAGE
BLACK AND WHITE PHOTOGRAPH

-62-

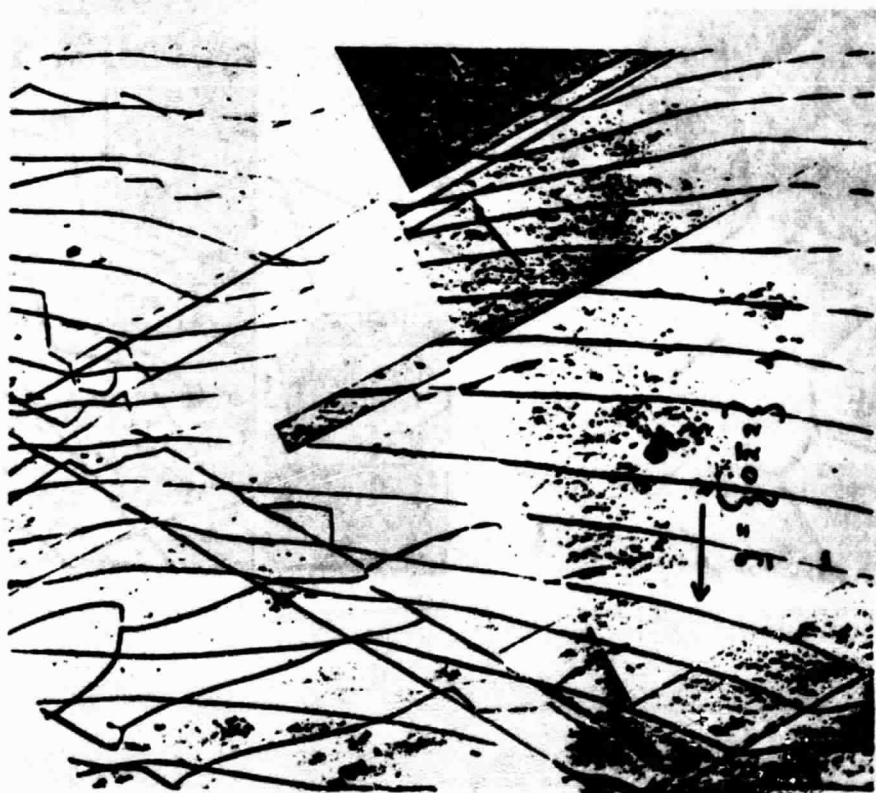
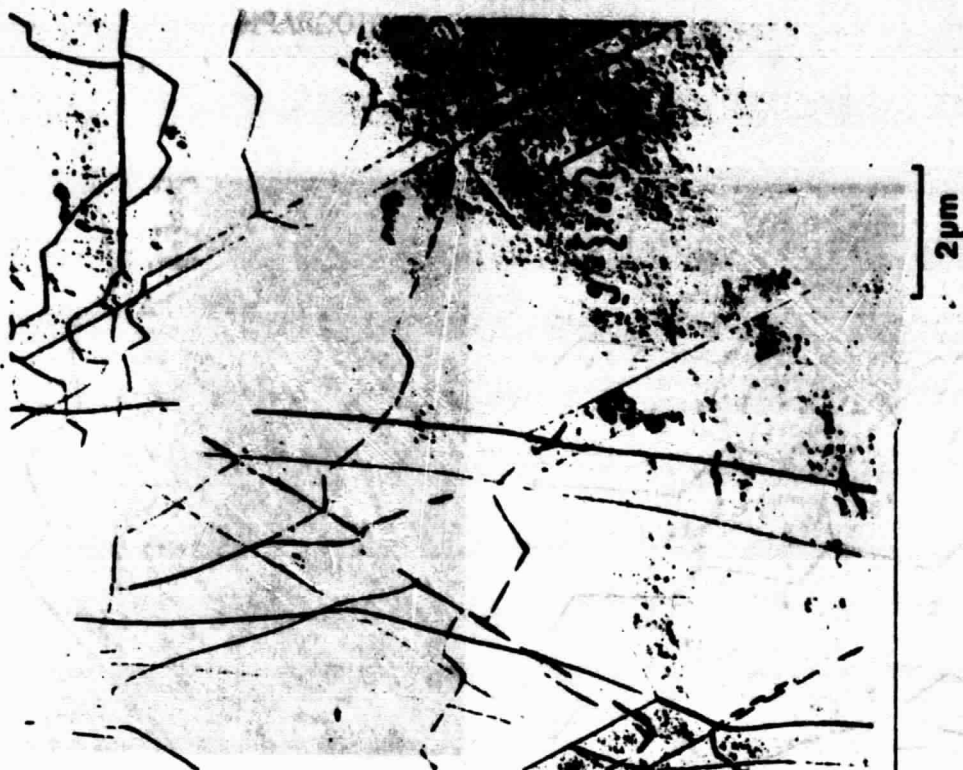


Fig. 10

ORIGINAL PAGE IS
OF POOR QUALITY

III) DEFECT STRUCTURE OF EFG SILICON RIBBON

ABSTRACT

The defect structure of EFG ribbons has been studied using EBIC, TEM and HVEM. By imaging the same areas in EBIC and HVEM a direct correlation between the crystallographic nature of defects and their electrical properties has been obtained. (i) Partial dislocations at coherent twin boundaries may or may not be electrically active. Since no microprecipitates were observed at these dislocations it is likely that the different electrical activity is a consequence of the different dislocation core structures. (ii) 2nd order twin joins were observed which followed the same direction as the coherent first order twins normally associated with EFG ribbons. These 2nd order twin joins are in all cases strongly electrically active.

EFG ribbons contain high concentrations of carbon. Since no evidence of precipitation was found with TEM it is suggested that the carbon may be incorporated into the higher order twin boundaries now known to exist in EFG ribbons.

1. INTRODUCTION

Rapid progress has recently been made in the production process of edge defined film-fed growth (EFG) silicon /1/. EFG ribbon is a promising material for the production of inexpensive solar cells and therefore an understanding of the relationship between the crystallographic nature of the defects and their electrical properties is desirable. This information can then hopefully be used to modify the ribbon growth process to reduce the density of defects which decrease the efficiencies of solar cells.

After a summary of the characteristic defect structure of various EFG silicon ribbons, results are presented which were obtained by correlating EBIC measurements and HVEM observations on selected defects.

2. EXPERIMENTAL TECHNIQUES

The electrical properties (i.e. enhanced minority carrier recombination) were investigated in the scanning electron microscope (SEM) operated in the electron beam-induced current (EBIC) mode. Schottky diodes were produced by evaporating a thin film of Al ($\sim 500 \text{ \AA}$) onto one surface /2/. EBIC images exhibit dark contrast at defects which act as recombination sites for minority carriers, with an EBIC resolution of $\sim 1\text{-}2 \mu\text{m}$. The EBIC technique can be extended to obtain quantitative information. The collected current can be measured as a function of specimen co-ordinates allowing the determination of 'recombination efficiencies' of specific defects /3/, minority carrier lifetime /4/ and trap level measurements /5/ are possible using high speed beam blanking techniques. These extensions of the EBIC technique are currently being introduced.

Defect structures were investigated by transmission electron microscopy (TEM). To obtain unbiased observations, specimens were broken off the ribbons at random, ground to a thickness of $\sim 50 \mu\text{m}$ and thinned for TEM examination by ion beam milling. Subsequent investigations were carried out in a Siemens Elmiskop 102 operating at an accelerating voltage of 125 kv (conventional TEM, CTEM).

To correlate electrical and structural properties of defects, areas were selected and mapped out in EBIC. Specimens 3mm in diameter were then cut out from the ribbon and ion-milled from the back-side (with the Schottky-diodes still at the surface) until the areas of interest were contained in the electron transparent regions. These specimens were subsequently examined in a high-voltage electron microscope (HVEM) operating at an accelerating voltage of 1MV. HVEM has the following advantages over CTEM because of the high penetration power of highly accelerated electrons (several μm as compared to 0.5 μm in CTEM):

- (i) The probability of finding the defects, previously mapped by EBIC, in the large transmittable area is high.
- (ii) Extended defects such as twin or other grain boundaries can easily be traced over long distances.
- (iii) The volumes investigated by HVEM and by EBIC are comparable.

Difficulties arise when comparing EBIC and HVEM micrographs because of the large difference in working magnifications (SEM-EBIC typically 1,000x, HVEM typically 10,000x). The comparison is facilitated by utilizing permanent surface marks, such as scratches, or etched topological features. In addition a series of low magnification EBIC micrographs (10x, 50x, 200x) helps to locate the areas of interest.

A brief discussion of the advantages of the present technique for the electrical characterization of defects, may be found in /6/.

3. INVESTIGATED EFG RIBBONS

The ribbons investigated in the present study are briefly described below:

- 1) JPL identification #5-871 run 18-112-1, 'small grain'. Displaced die, growth speed 3.0-3.4 cm/min. Undoped.
- 2) JPL identification #5-866 run 16-163, 'small grain'. Displaced bulbous ended die, growth speed 3.1 cm/min. Boron doped, resistivity 1 Ωcm .
- 3) JPL identification #5-1158. 'Large grain'. (reduced AT flow).
- 4) Mobil Tyco supplied... 'large grain' ribbon. (reduced AT flow).

4. CHARACTERISTIC DEFECT STRUCTURE OF EFG SILICON RIBBONS

4.1. Etch

Similar features were observed in all of the EFG ribbons examined, the only difference being the scale of the defects (e.g. 'large' and 'small' grain). Figs. 1(a) and (b) show typical etch patterns, which have already been described (e.g. /7/to/10/). Only a brief description will therefore be given here, with emphasis on features which are interesting in connection with the correlation work reported in Section 5.

On a large scale the observed pattern is generally inhomogeneous, on a small scale, however, frequently homogeneous. Figure 1(a) shows an area of parallel striations, which are generally attributed to the presence of twin boundaries. (see Section 5 for a detailed discussion). At the top of Figure 1(a) is a region containing a high density of dislocation etch pits. It should be noted that the density of dislocations varies appreciably from region to region. Whereas Figure 1(a) represents the 'standard' defect structure (i.e. equilibrium structure', e.g. /11/) which is frequently discussed, Figure 1(b) shows an example of a more complicated pattern. Areas such as this were found on all of the ribbons and covered appreciable areas of the surface. The irregularity in Figure 1(b) is caused by reactions between grain and/or twin boundaries and by an inhomogeneous distribution of dislocations. In several regions the dislocation etch pits are aligned along crystallographic directions suggesting that the dislocations had been generated by plastic processes (See Section 5).

The orientation of the grains at the surface varies; in order of falling frequency $\{110\}$, $\{112\}$ have been found, in partial agreement with earlier work /12,13/. An example of the variation in grain orientation is shown in Figure 2. Orientations are given with respect to the growth direction.

4.2. EBIC

Figure 3 is a low magnification EBIC micrograph showing the distribution of electrically active defects. In the upper part of the micrograph contrast lines apparently due to grain boundaries are visible. In addition black dots due to active dislocations are randomly distributed throughout the matrix. [Figure 4 is a higher magnification micrograph of the area described above.] Most of Figure 3 consists of almost horizontally aligned boundaries, some of these very dark (showing strong electrical activity), some weak in contrast or exhibiting 'dotted' contrast. Figure 5 shows an-

other example of dotted EBIC contrast where the effect is more pronounced. We will show in Section 5 that this pattern is related to the twinned structure of the material. Such a relationship was earlier inferred from comparison of etched surfaces and EBIC micrographs /3/ and by independent observations of twins in TEM /10/. An exact analysis, however, requires direct correlation between EBIC and TEM, as presented in Section 5.

4.3. TEM

Twins with a $\{111\}$ habit plane occur with a high frequency and are therefore generally observed by TEM. A typical twinned structure is shown in Figure 6. The thicknesses of micro-twins may vary from a few layers of $\{111\}$ planes up to tens of microns (which of course means single twin boundaries are observed in TEM). A micro-twin five layers thick is revealed by structural imaging in Figure 7. The 'small grain' ribbons contain a high density of microtwins (e.g. Figure 6) with thicknesses up to several 100 nm. 'Large grain' material contains isolated twin boundaries spaced several μm apart, resulting in a more proportionate distribution of 'twinned' and 'matrix' material.

Twin boundaries may contain partial dislocations (twin boundary dislocations) the density of which can vary from boundary to boundary. No relationship between twin boundary dislocation density and ribbon type has been found.

4.4. Results concerning the carbon content

Graphite dies are used in EFG ribbon growth. Two consequences result from this technique: (i) SiC - particles are present at the ribbon surface (e.g. /3/) and (ii) a high density of carbon ($\sim 10^{18} - 10^{19} \text{ cm}^{-3}$ /14/) is incorporated into the silicon material.

EBIC has been used to investigate the electrical activity of the defect structure nucleated at SiC particles. Figure 8 shows a typical arrangement with a high density of black dots, corresponding to dislocations, and a number of twin boundaries. Except for this high density of defects no other unusual effects were observed. This is particularly interesting since an excess of carbon may be expected near a SiC particle, thereby enhancing any carbon-induced impurity segregation. Such a segre-

gation is expected to cause increased minority carrier recombination. However, in the present study, the electrical activities of the defect structure near SiC particles, and of the 'equilibrium structure' are not noticeably different.

Recently a ribbon growth model was proposed to account for carbon concentrations above the solubility limit /15/. The model assumes eutectic growth and directional solidification of the ribbon, which leads to lamellae of a silicon-carbon 'phase' embedded in a carbon rich silicon matrix. Such a structure should give rise to special contrast effects in TEM. If the silicon-carbon phase is not coherent with the silicon matrix, which is likely due to the difference in the bond lengths of silicon and carbon atoms, strain contrast effects should be observed, at least at irregularities of the lamellae. Moreover, interference patterns, e.g. Moiré fringes, and/or, in the case of a long range order, diffraction effects would be expected. None of these effects has been observed in this study.

5. CORRELATION OF EBIC WITH HVEM OBSERVATIONS

Figure 9(c) shows part of an EBIC micrograph exhibiting a row of dots similar to those seen in Figure 3. Figure 9 (a) is a HVEM micrograph of the same area. A comparison of Figure 9 (a) and (c) confirms that the dots mark the trace of a microtwin approximately 200 nm thick, the boundaries of which are visible in fringe contrast. This microtwin is imaged in Figure 9 (b) with its boundaries invisible, revealing that partial dislocations are contained in both boundaries. A comparison of EBIC and HVEM micrographs shows a one to one correspondence between dots and dislocations. Ignoring the central spot for the moment, the EBIC dots have similar contrast and correspond to individual slightly curved dislocations. Diffraction contrast analysis reveals that the dislocations differ in Burgers vector (of type $1/6 \langle 112 \rangle$), and that their character is not of simple 30° or 90° type. These observations suggest that the dislocations are comparably effective sites for the recombination of minority carriers, irrespective of their crystallographic character. The central dot in Figure 9 (c) arises from the combined effect of a group of 3 partial dislocations which are too closely spaced to be resolved by EBIC. ($\sim 1-2 \mu\text{m}$).

Figure 10 (a) shows another example of dots in EBIC contrast. These dots, though similar to those shown in Figure 9 (c) are caused by a totally different structure. Figure 10 (b) is an etch pattern from the same area, showing that the observed contrast in Figure 10 (a) is due to the interaction of boundaries. The nature of the boundaries was determined by HVEM. As an example the area encircled in Figure 10 is shown in Figure 11. A three dimensional sketch of this area clarifying the relationships between the different areas is given in Figure 12. Analysis shows that T_1 is a microtwin $\sim 100\text{nm}$ thick, lying in the matrix M perpendicular to the growth surface. T_2 is in a different twin orientation to the matrix M with an inclined $\{111\}$ - habit plane. Thus the boundary between T_1 and T_2 joins two crystal grains with a misorientation caused by two non-parallel twinning operations. The geometric construction is depicted in Figure 13, projected along the $\langle 110 \rangle$ direction common to all three grains. Boundaries of this type have been termed 'second order twin joins' by Kohn /16/ and are $\Sigma 9$ boundaries in the CSL model /17/. In the present case the $\{111\}$ plane of T_1 matches a $\{115\}$ plane of T_2 . This unsymmetric configuration has been modelled by Kohn /18/, yet has not been observed so far to the author's knowledge. The dislocation model discussed by Hornstra /19/ could also be extended to describe this unsymmetric case, but would require a very high density such that the dislocation core regions would overlap. In Figure 11 (b) the specimen was tilted to show the boundaries of the microtwin T_1 . Dislocations that are contained in the $\{111\}/\{115\}$ boundary are clearly visible. These dislocations accommodate a small deviation from the $\{111\}/\{115\}$ orientation relationship and are commonly referred to as extrinsic boundary dislocations /20/. The Burgers vectors of these dislocations have not been analyzed.

Figure 14 shows a contrast experiment to determine the character of the partial dislocations present in the boundaries T_2/M . The specimen was tilted until these boundaries were almost perpendicular to the incident electron beam, allowing an easy determination of the crystallographic direction of the straight dislocation lines. The Burgers vectors were found from standard contrast analysis /21/. The dislocations

analyzed were Shockley partials of either 30° or 90° type, examples are indicated in Figure 14 (c).

The comparison of the HVEM micrographs (Figures 11 and 14) with the corresponding EBIC pattern (Figure 10) gives the following result: (i) The black dots in Figure 10 (a) correspond to the $\{111\}/\{11\bar{5}\}$ second order twin joins, which therefore represent efficient sites for minority carrier recombination. (ii) The straight 30° and 90° partial dislocations show no contrast in EBIC (although etched in Figure 10 (b)) and thus are virtually electrically inactive.

6. DISCUSSION

In recent years a large number of experimental results on the dislocation core structure in tetrahedrally co-ordinated semiconductors has appeared (e.g. /22/). High resolution electron microscopy has revealed the presence of dissociated and constricted perfect dislocations (e.g. /23, 24/). Dislocations introduced by plastic processes are generally dissociated /22/ and are, since dissociation is difficult to envisage on the shuffle-set, therefore assigned to the glide set (e.g. /22/). Indications for the existence of "shuffle set" dislocations /25/ in Ge, suggest that such dislocations also may exist in Si. Transformation from one set to the other can occur by the addition or removal of rows of point defects /26/; experimental evidence for such a process exists (e.g. /24/).

Theoretical models for dislocation core structures were first developed by Hornstra /27/, and these models have been extended and refined to include bond reconstruction (e.g. /23/). The electrical properties of dislocations with different core structures are likely to be different.

Experimental results obtained by combining EBIC with HVTEM will contribute to the discussion of these various models.

6.1. Dislocations at coherent twin boundaries

In the present investigations dislocations were observed with apparently two different levels of electrical activity: dislocations giving rise to an EBIC contrast, Figure 9 (c), and dislocations with no, or at least considerably lower electrical activity, Figure 11. Confirmation of these observations is required before a detailed inter-

pretation of the nature of dislocations can be presented. It is however interesting to speculate about the possible significance of the present results, with regard to the formation and core structures of dislocations.

The simplest approach to correlating crystallographic and electrical properties is to reduce the number of applicable models. To this end the present investigation is concerned with single partial dislocations and therefore the question of whether the dislocation is dissociated or constricted (as present with perfect dislocations) does not arise.

It is conceivable that the core structure of a dislocation will depend on how the dislocation is generated. The present observations, that the electrically active dislocations do not follow $\langle 110 \rangle$ directions, and are in fact sometimes curved, and that the non-active dislocations are aligned along a $\langle 110 \rangle$ Peierls valley, tends to support this view. During growth of EFG ribbons there are two temperature ranges in which dislocation generation processes may occur. During solidification, when diffusion can occur, twin boundaries grow and can accommodate partial dislocations by atomic steps in the boundaries. At lower temperatures thermal stresses are relieved by plastic processes and these dislocations can react with twin boundaries, in which case the lattice dislocations dissociate into twin-boundary partial dislocations. Diffusion plays only a minor role in this case. Whether a distinction between grown-in and deformation induced dislocations is possible and what type of dislocations are formed by each process has yet to be determined.

6.2. The $\{111\} \{115\}$ second order twin join

The present study has shown that the detected $\{111\} \{115\}$ second order twin join is strongly electrically active. Since extrinsic dislocations are contained in the investigated boundary it cannot be explicitly stated that the electrical activity is an intrinsic property of the boundary. However considering the complicated arrangement of atoms and bonds at the boundary (e.g. Figure 13) it is likely that the extrinsic dislocations have only an additional effect, if at all, on the electrical activity.

Since the second order twin join is confined to the $\{111\}$ matrix planes it is of

considerable interest in the discussion of the so-called equilibrium structure /11/⁻⁷²⁻ of EFG (and comparably grown) ribbons. This structure has been identified from etch investigations to be generally present in EFG ribbons and to consist of parallel coherent twin boundaries which extend on {111} matrix planes along the growth direction. Consequently, once a second order twin join is formed on a {111} matrix plane it can extend over long distances parallel to the equilibrium structure without further reactions. Second order twin join therefore have to be regarded as an inherent part of the defect structure of EFG ribbons. Thus the equilibrium structure consists of a large number of electrically inactive coherent twin boundaries intermingled with electrically active second (or even higher) order twin joins. This conclusion is consistent with thus far unexplained EBIC observations (e.g. /3, 10/, that only some of the linear boundaries revealed by etching are electrically active.

6.3. CARBON DISTRIBUTION IN EFG-RIBBONS

It has been found that the grain size of EFG ribbons generally decreases with increasing (overall) carbon concentration /15/. Since this concentration is beyond the carbon solubility limit in silicon the distribution of C has to be considered. The present experiments give no indication for a lamellae two-phase structure as suggested in the eutectic growth model /15/. The TEM observation of {115} {111} second order twin joins suggests the possibility that the carbon is preferentially incorporated into such joins, as well as into higher order twin and other grain boundaries. This explanation seems reasonable since the atomic arrangement at these boundaries is considerably disturbed (independent of the model used to describe the joins) thereby allowing the incorporation of a high density of carbon atoms. The correlation-higher carbon concentration smaller grain size is natural in this context since decreasing grain size increases the possibility of twin boundary interactions. How an intentional increase in the concentration of incorporated carbon atoms (by changing the growth conditions of the EFG ribbon) causes more boundaries to form, and how the carbon atoms influence the electrical activity of the higher order twin joins are topics of future research.

. CONCLUSIONS

1. The correlation of HVTEM and EBIC is a valuable tool for the investigation of the defect structure of semiconducting materials, e.g. EFG ribbons.
2. The existence of the $\{115\}$ $\{111\}$ second order twin join has been proven for the first time. It may occur relatively frequently in the ribbon due to twin boundary interactions and lies along the same direction as the first order twin boundaries.
3. The $\{115\}$ $\{111\}$ twin joins were observed to be electrically active, whereas coherent $\{111\}$ $\{111\}$ twin boundaries were inactive.
4. Partial dislocations at coherent twin boundary can be electrically active. No microprecipitates were observed at these dislocations suggesting that the electrical activity is not impurity controlled but a consequence of the dislocation core structure per se.
5. It is suggested that the carbon atoms present in EFG ribbons in high concentrations are preferentially adsorbed to the higher order twin joins.

ORIGINAL PAGE IS
OF POOR QUALITY

REFERENCES

1. J.P. Kalejs, B.H. Mackintosh and T. Surek, J. Cryst. Growth, 50 175 (1980).
2. T. Sullivan and D.G. Ast, J.P.L. Technical Report, #3 Contract No. 954852 (1979).
3. J.S. Hanoka, Solar Cells, 1, 123 (1979).
4. D.E. Ioannov, J. Appl. Phys. D: Appl. Phys., 13, 611 (1980).
5. L.C. Kimerling and J.R. Patel, Appl. Phys. Lett., 34, 73 (1979).
6. H. Strunk and D.G. Ast, Proc. 38th EMSA, 38 323, (1980).
7. H. Föll and D.G. Ast, J.P.L. Technical Report #1 Contract No. 954852 (1978).
8. C.V.H.N. Rao, M.C. Cretella, F.V. Wald and K.V. Ravi, J. Cryst. Growth 50, 311 (1980).
9. C.V. Hari Rao, H.E. Bates and K.V. Ravi, J. Appl. Phys., 47, 2614 (1976).
10. K. Yang, G.H. Schwuttke and T.F. Ciszek, J. Cryst. Growth 50, 301 (1980).
11. K.V. Ravi, J. Cryst. Growth, 39, 1 (1977).
12. G.H. Schwuttke, T.F. Ciszek and A. Kran, J.P.L. Technical Report #3, Contract No. 954144 (March 1976).
13. L.C. Garone, C.V. Hari Rao, A.D. Morrison, T. Surek and K.V. Ravi, Appl. Phys. Lett. 29, 511 (1976).
14. F.V. Wald, Private communication (1980).
15. F. Wald, Electrochemical Soc. Meeting, St. Louis, May 1980.
16. J.A. Kohn, Am. Mineral, 41, 778 (1956).
17. W. Bollmann, Crystal Defects and Crystalline Interfaces, Springer-Verlag (1970).
18. J.A. Kohn, Am. Mineral., 43, 263 (1958).
19. J. Hornstra, Physica, 25, 409 (1959).
20. R.W. Balluffi, Y. Komen and T. Schober, Surf. Sci., 31, 68 (1972).
21. P.B. Hirsch, A. Howie, R.B. Nicholson, D.W. Pashley and M.J. Whelan, Electron Microscopy of Thin Crystals, London: Butterworth (1965).
22. Proc. Int. Symp., Dislocations in Tetrahedrally Co-ordinated Semiconductors, J. Physique Colloq - C6, 40, (1979).
23. P.B. Hirsch, J. Microsc., 118, 3 (1980).
24. H. Alexander, J. Physique Colloq - C6, 40, 1 (1979).
25. A. Bourret and J. Desseaux, J. Physique Colloq-C6, 40, 7 (1979).
26. J.P. Hirth and J. Lothe, Theory of Dislocations, McGraw Hill, New York (1968) pp 359-362.
27. J. Hornstra, J. Phys. Chem. Sol., 5, 129 (1958).

FIGURE CAPTIONS

1. Optical micrographs of etched ribbon surface Ribbon #2.
2. Optical micrograph of ribbon surface showing variation in grain orientations. Open circles mark areas analyzed by Laue X-ray and also orientations with respect to standard 001 stereographic projection (Courtesy of F. Stafford).
3. EBIC micrograph of typical EFG structure. Ribbon #2.
4. Higher magnification EBIC micrograph of area at top right of Figure 3.
5. EBIC micrograph showing dotted contrast along linear boundaries. Ribbon #3.
6. TEM micrograph (125 kv) of microtwins in E.F.G. ribbon. Ribbon #1.
7. High resolution structural image of a microtwin five atomic layers thick. (125 kv).
8. EBIC micrograph showing contrast near a SiC particle. Ribbon #4.
9. a) Bright field HVEM image of a microtwin containing dislocations. b) Same area with twin out of contrast. c) EBIC micrograph from the same area. g = diffraction vector - Ribbon #4.
10. a) EBIC micrograph showing dotted contrast. b) Optical micrograph of the same area showing interaction of microtwins. Ribbon #2.
11. a) Bright field HVEM micrograph of twin boundaries shown in Figure 10. b) Same area with one set of twin boundaries out of contrast.
12. Schematic sketch of the arrangement of twin boundaries shown in Figure 11.
13. Projection along the common $\langle 110 \rangle$ direction of twins indicated in Figure 12 showing the arrangement of atoms at the (111) (115) twin join.
14. HVEM micrographs of the same area as Figure 11. These were used to determine the nature of the dislocations in the twin boundaries, examples of which are marked in c).

ORIGINAL PAGE IS
OF POOR QUALITY



ORIGINAL PAGE
BLACK AND WHITE PHOTOGRAPH

200μm



Figure. 1

400μm



Figure. 2

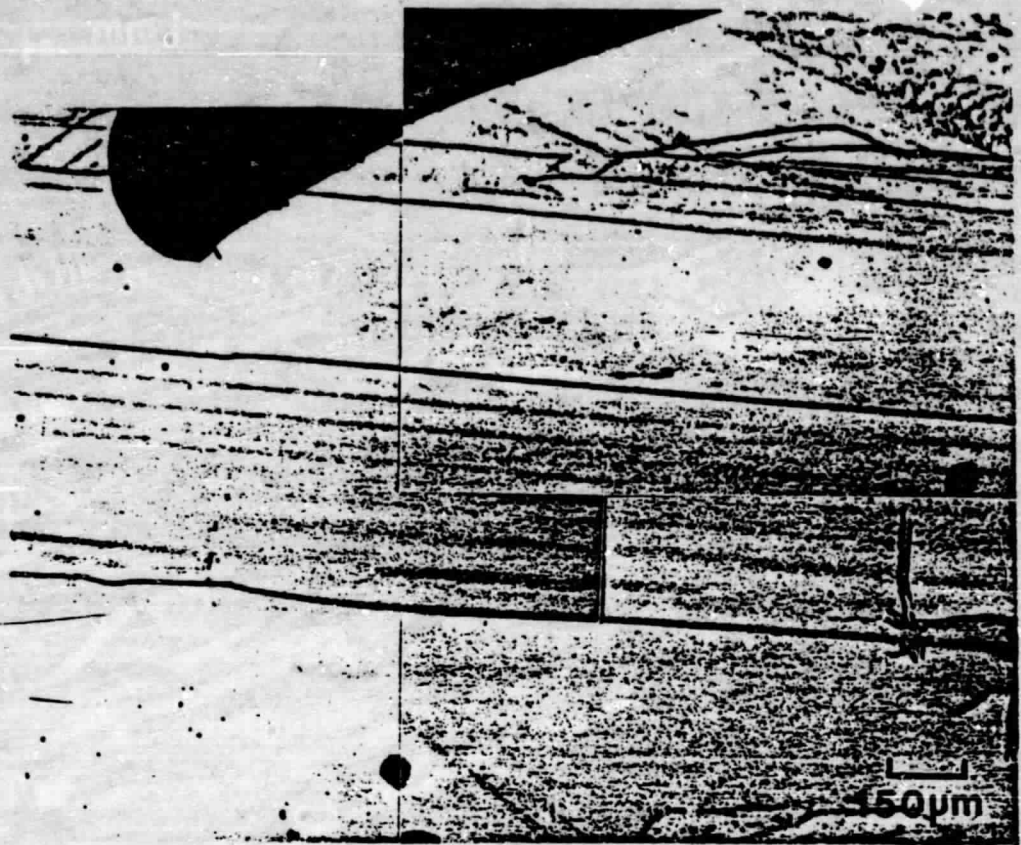


Figure. 3



Figure. 4

ORIGINAL PAGE
BLACK AND WHITE PHOTOGRAPH

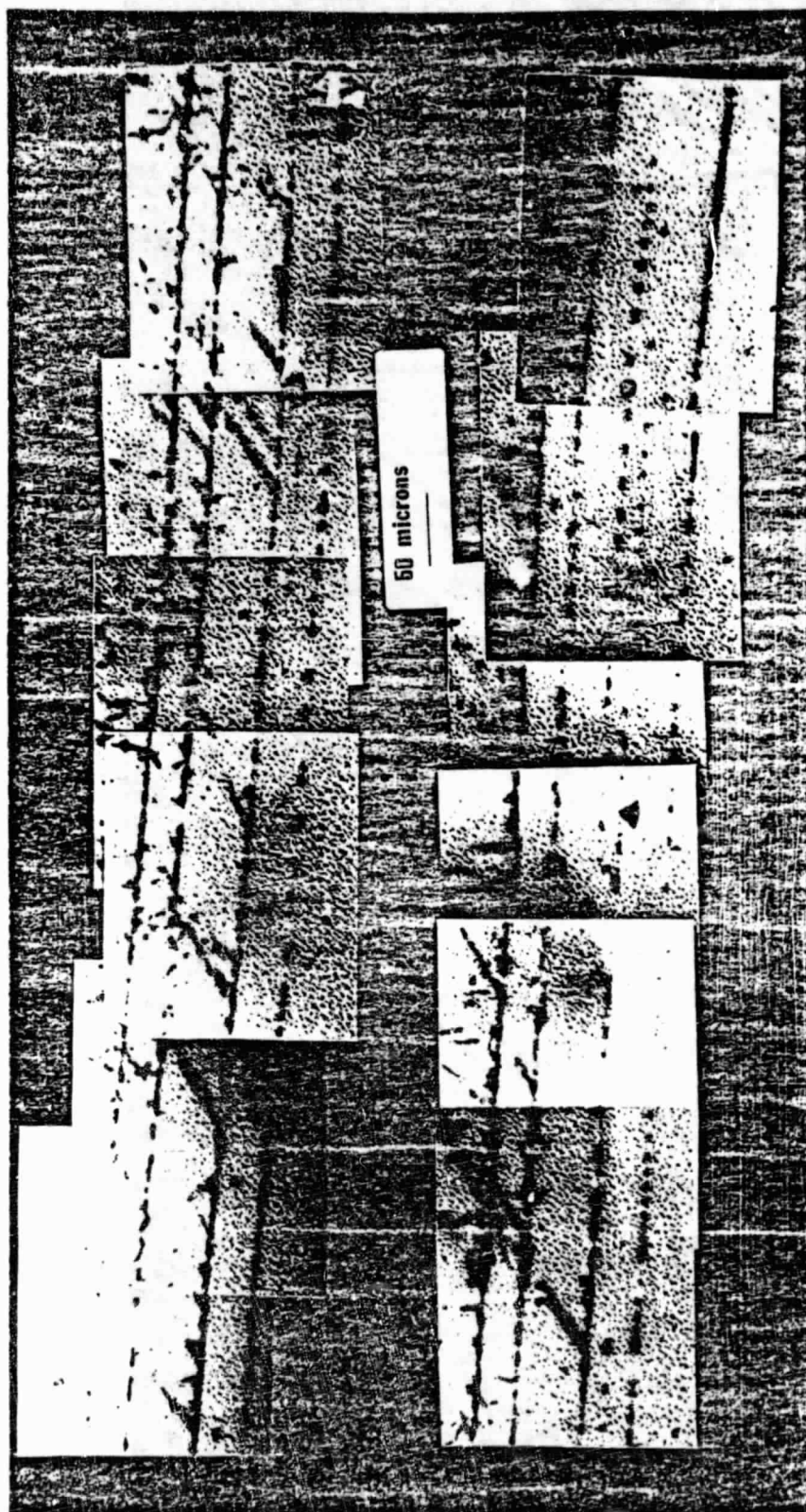


Figure. 5

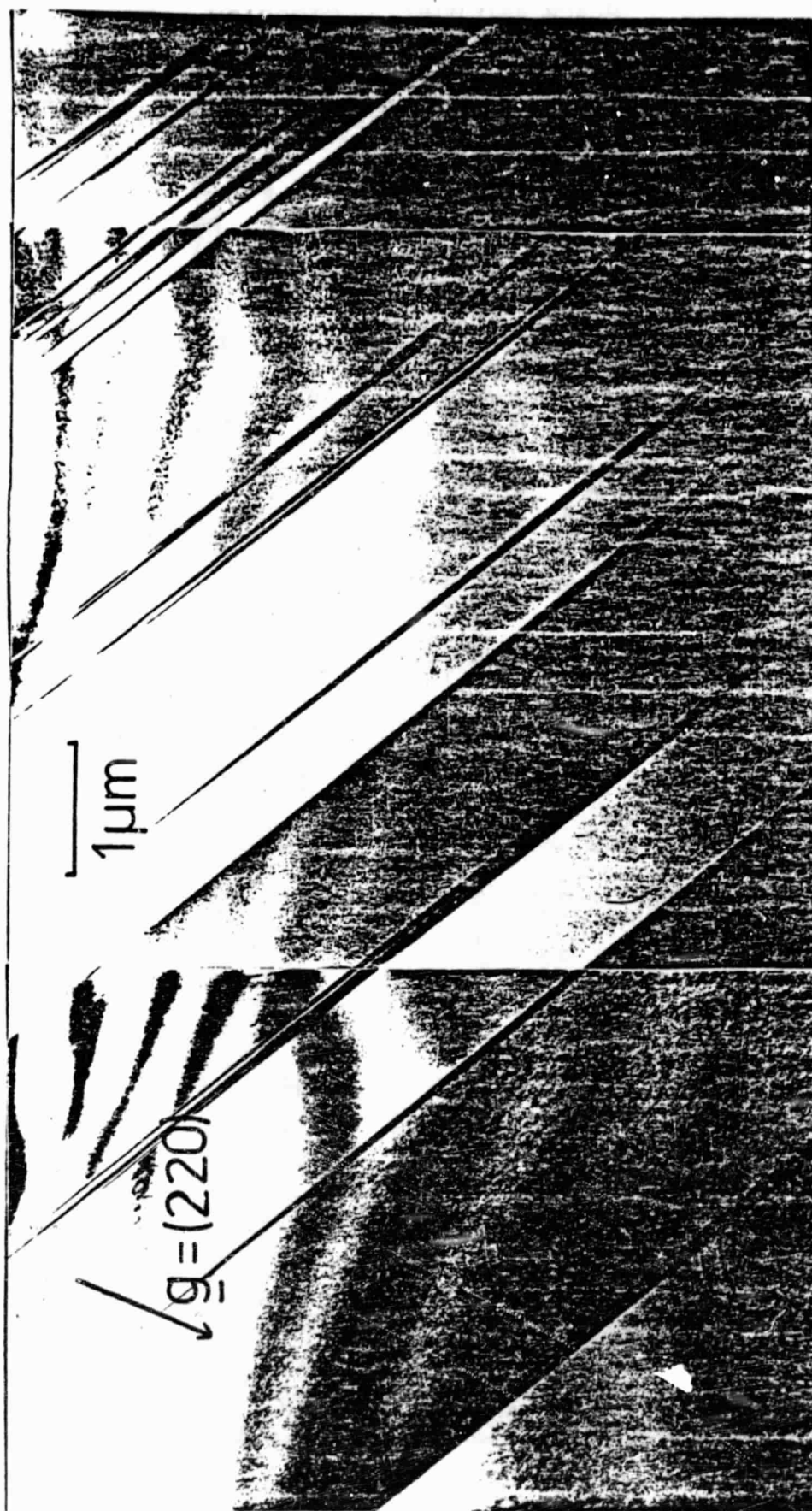


Figure. 6

ORIGINAL PAGE
BLACK AND WHITE PHOTOGRAPH

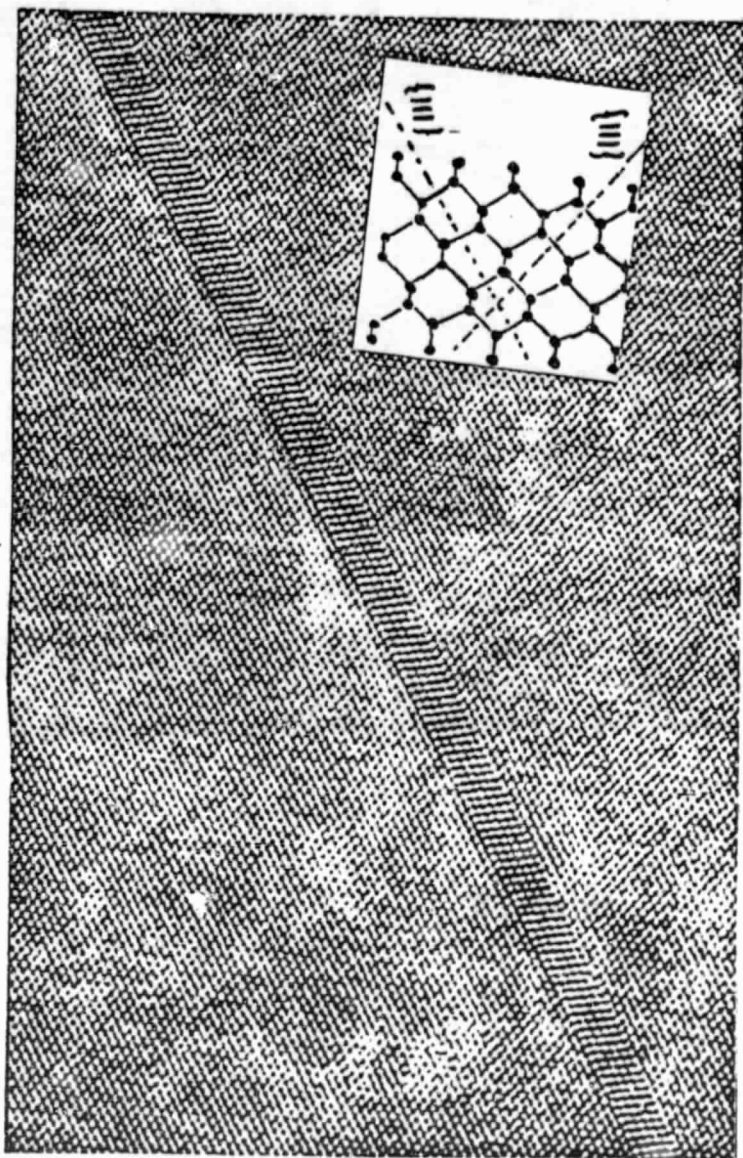


Figure. 7

ORIGINAL PAGE
BLACK AND WHITE PHOTOGRAPH

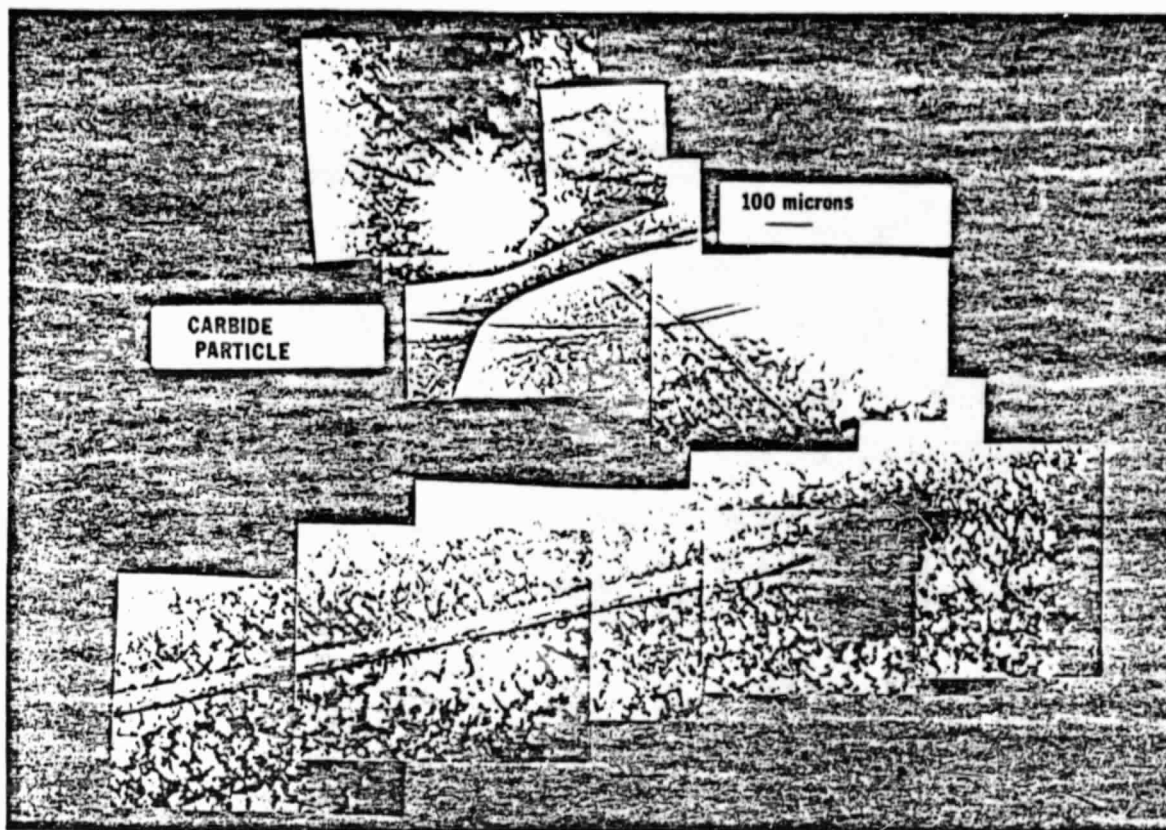
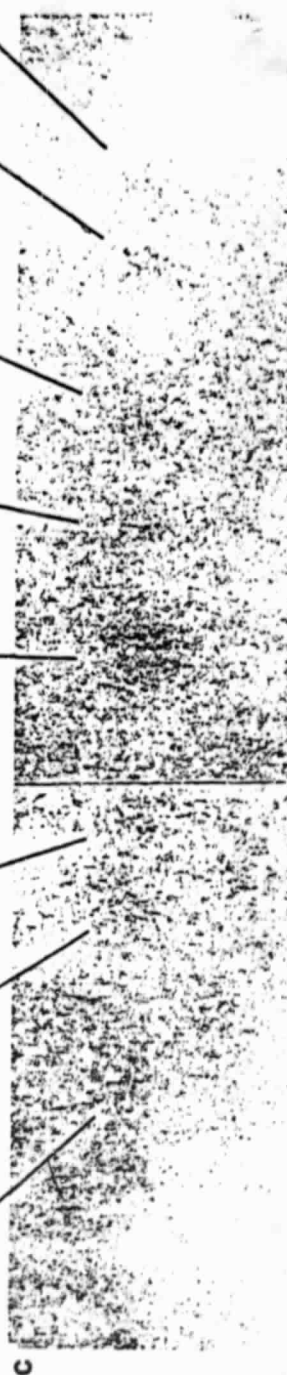
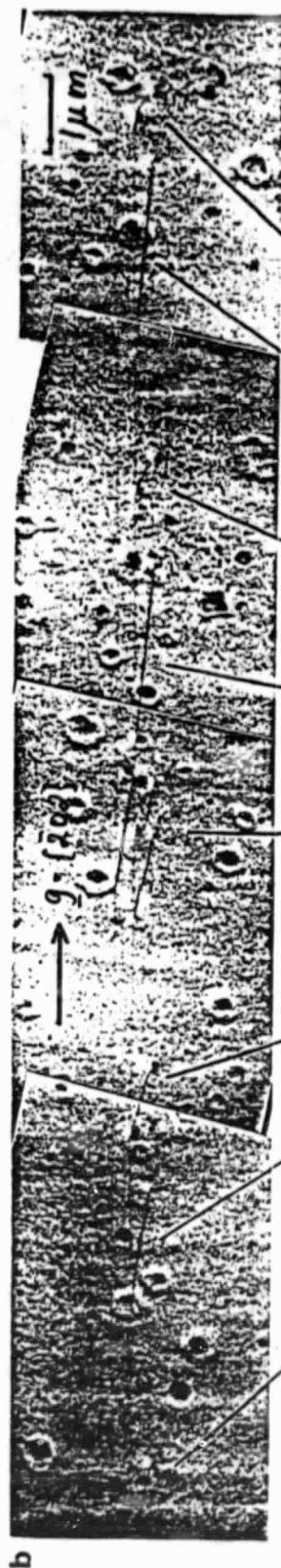


Figure. 8



ORIGINAL PAGE
BLACK AND WHITE PHOTOGRAPH

Figure. 9

ORIGINAL PAGE
BLACK AND WHITE PHOTOGRAPH

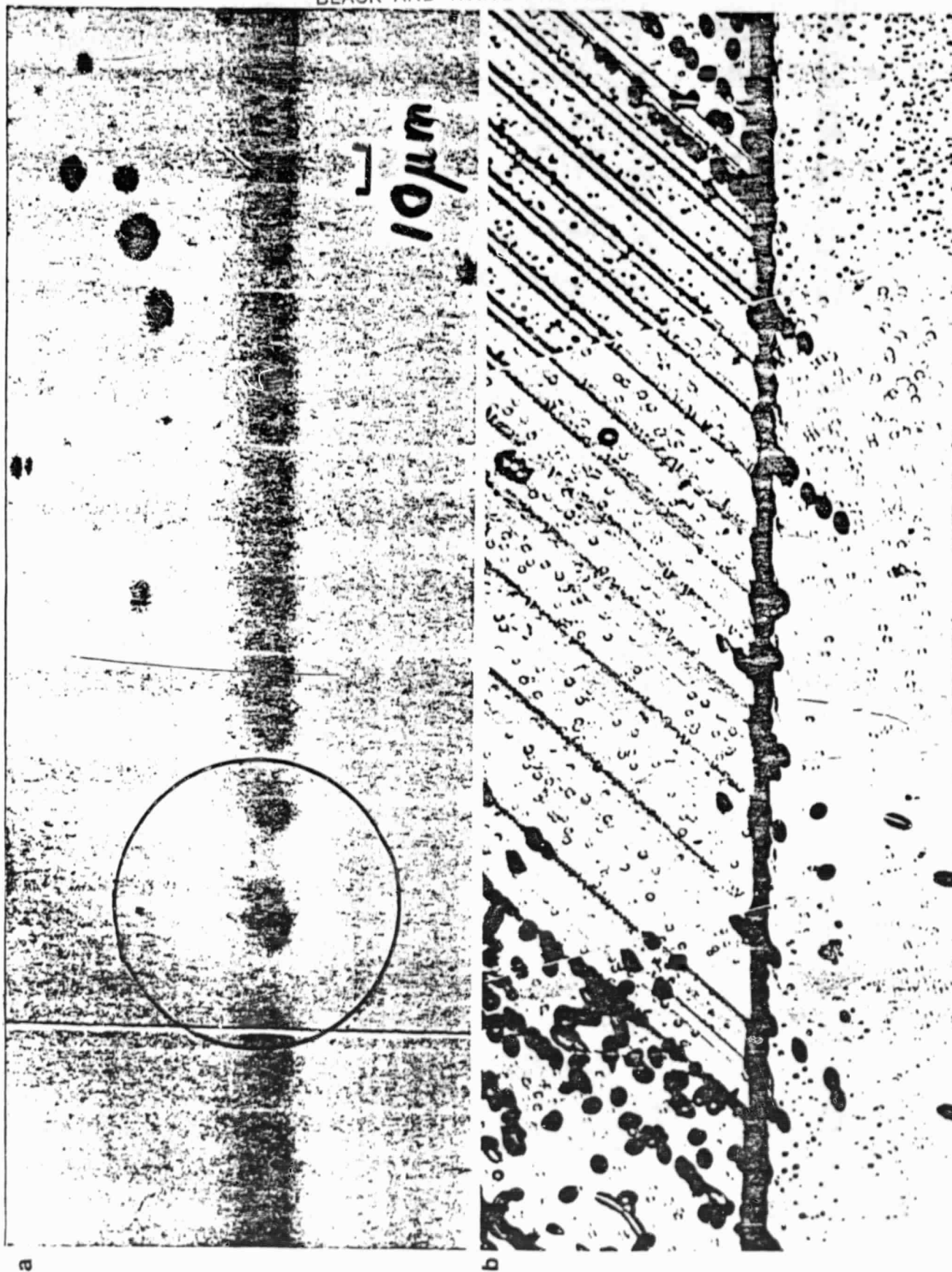


Figure. 10

ORIGINAL PAGE
BLACK AND WHITE PHOTOGRAPH

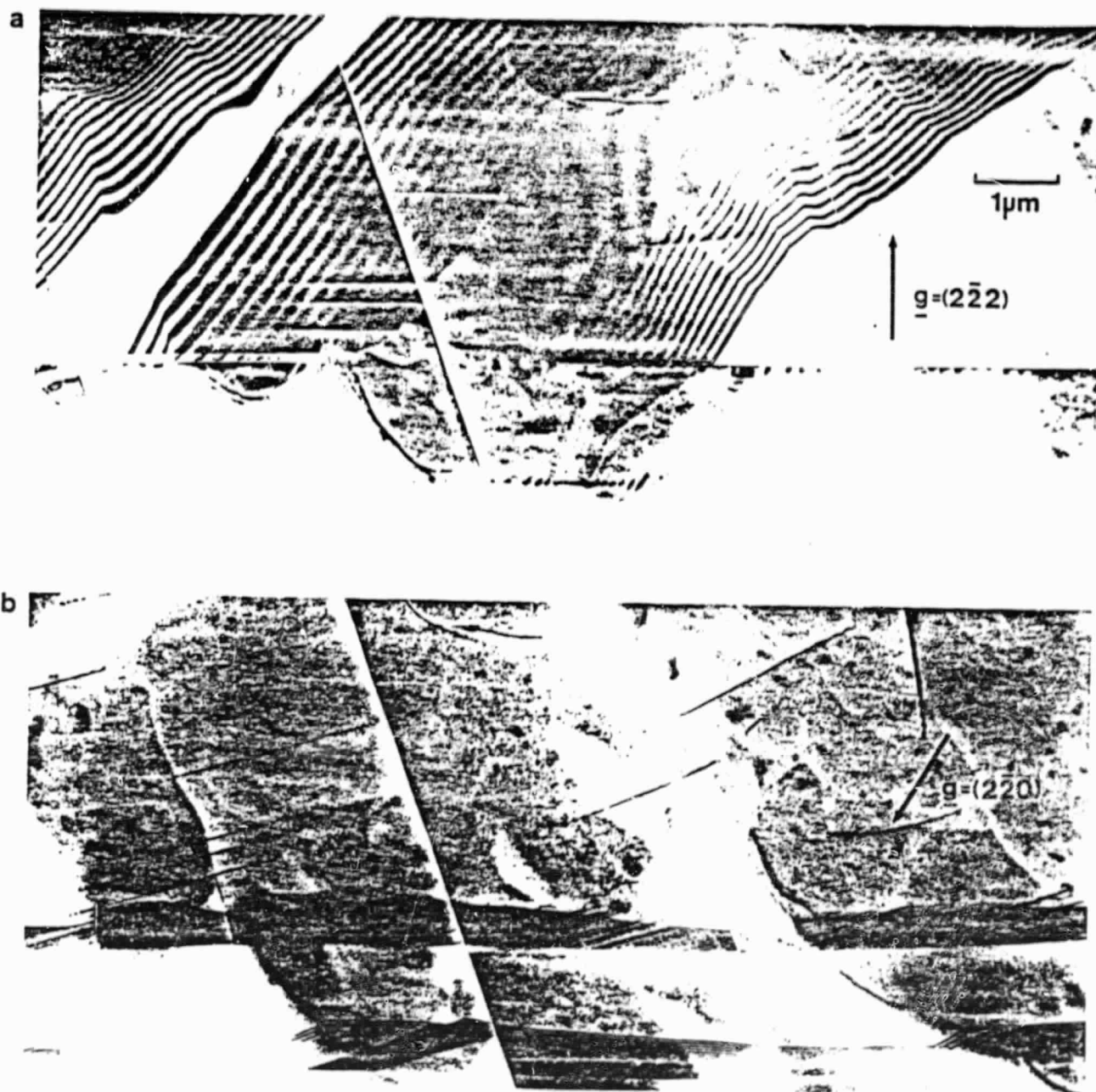


Figure.11

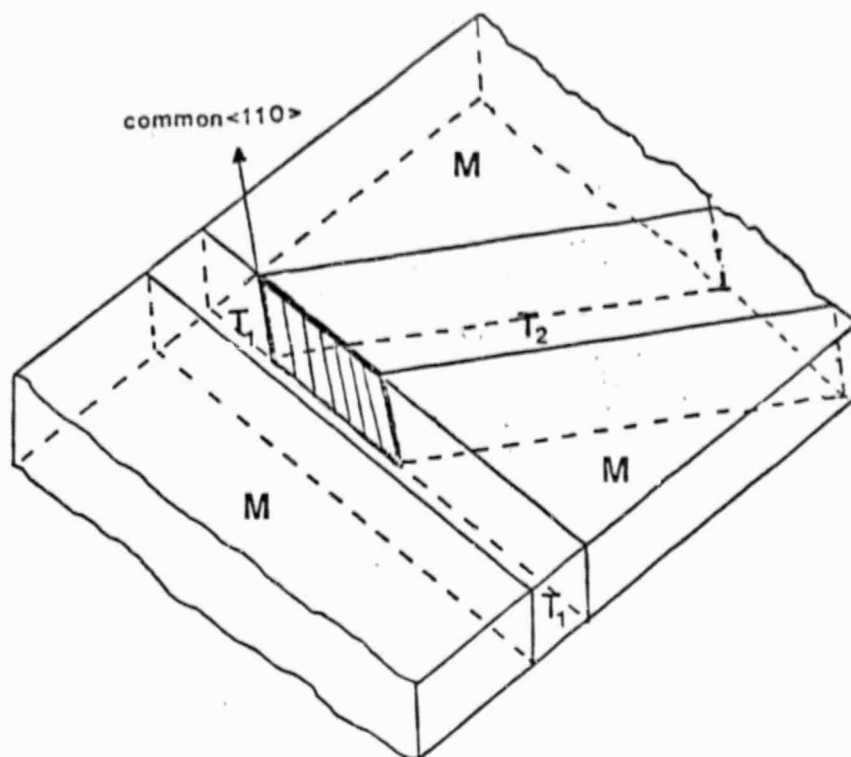


Figure.12

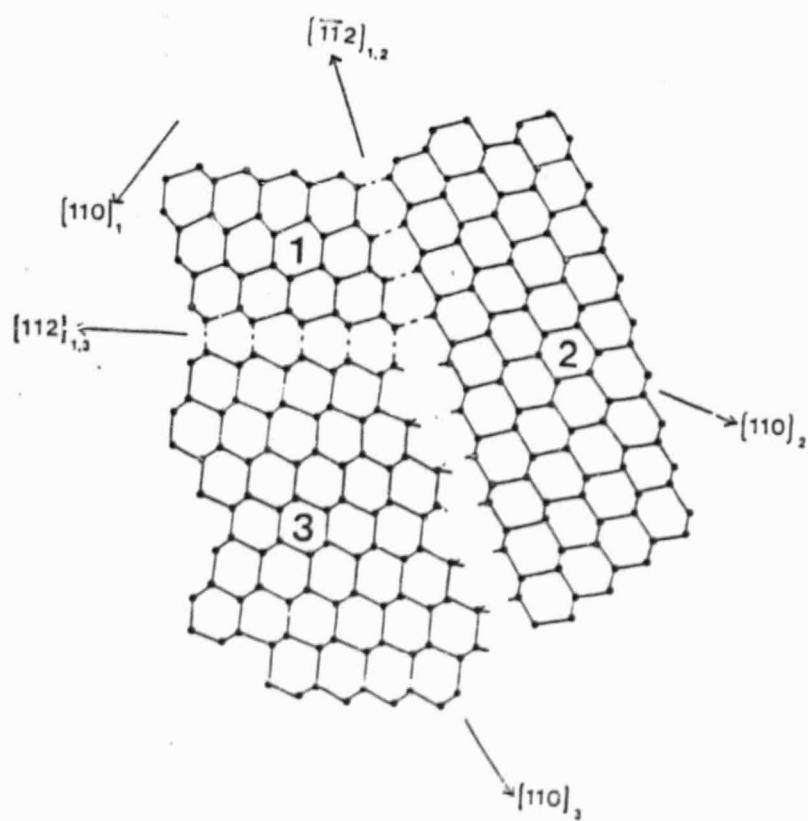


Figure. 13

ORIGINAL PAGE
BLACK AND WHITE PHOTOGRAPH

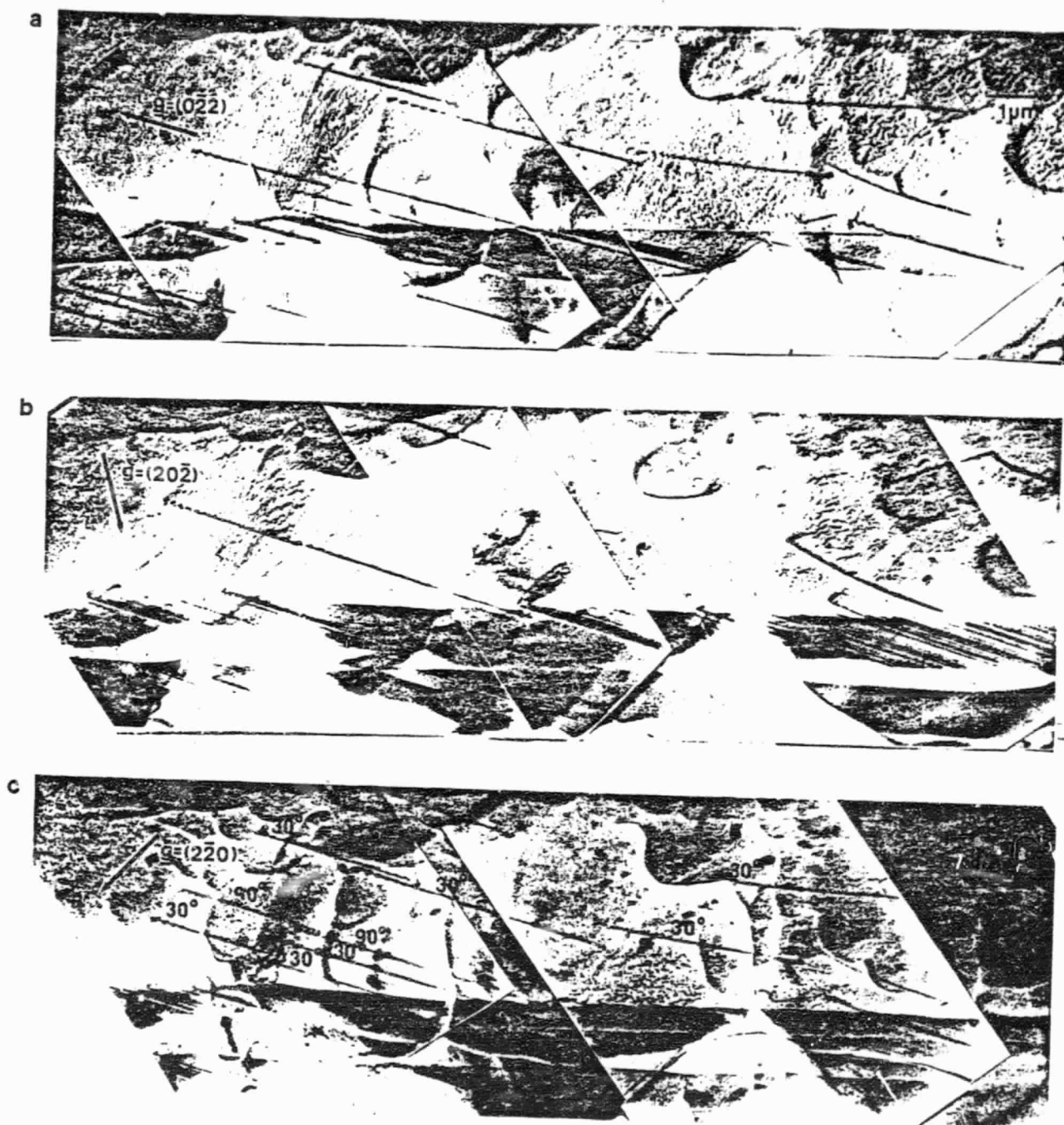


Figure.14

APPENDIX

ORIGINAL PAGE IS
OF POOR QUALITY

Electron Diffraction and Microscopy Studies
of the Structure of Grain Boundaries in Silicon
C.B. Carter, H. Föll, D.G. Ast and S. L. Sass
Department of Materials Science and Engineering
and Materials Science Center

Cornell University
Ithaca, New York 14853

ABSTRACT

The diffraction effects expected from the periodic structure of twist boundaries in Si were determined by an examination of the reciprocal lattice of these boundaries. Methods of analysis were developed to distinguish between the real diffraction spots due to the periodic boundary structure and those due to double diffraction effects. The electron microscope images from the boundaries studied in Si bicrystals frequently were complex and contained Moiré fringes which provided no information on the actual boundary structure. By analyzing the electron diffraction patterns from these boundaries for the presence of new diffraction spots it was possible to show that all the $\Sigma 1$ [001], $\Sigma 1$ [111] and $\Sigma 3$ [111] twist boundaries examined have a periodic structure.

ORIGINAL PAGE IS
OF POOR QUALITY

1. Introduction

Recently Föll and Ast (1979) reported the results of a transmission electron microscope study of the structure of twist and tilt boundaries in silicon bicrystals which had been produced by hot-pressing single crystal chips of silicon. The pressure-sintering technique allows systematic studies to be made of well-characterized boundaries where, for example, the boundary plane is fixed and the misorientation angle is varied. This technique was first developed for gold bicrystals by Schober and Balluffi (1969, 1970), but unlike the boundaries in gold which are parallel to the surface of the thin foil, those in silicon are cut to be inclined or normal to the foil surface.

[The boundaries in gold can be made to rotate to the edge-on orientation (Schober and Balluffi (1971)) or be prepared in this orientation (Cosandey, Komem and Bauer (1978)).]

Föll and Ast showed that small angle twist boundaries in silicon consist of periodic arrays of screw dislocations as observed in the study of similar boundaries in gold. It was also observed that as the misorientation angle increased the visibility of the dislocation array decreased, as expected from diffraction contrast theory (Thölen 1970). Fringe contrast with spacings as small as 1.3 nm could be detected in the images of a $\Sigma 1$ [001] boundary. Lattice fringe imaging suggests that such images are due to a Moiré (interference) effect and not to the actual boundary structure.

Carter, Donald and Sass (1979) have recently examined the geometry of the reciprocal lattice associated with an inclined grain boundary in a thin foil and demonstrated that the diffraction pattern from the grain boundary region can provide unambiguous information on the periodic nature of the boundary. It was also shown that both the real extra reflections due to the boundary structure and the additional spots in the diffraction pattern arising from double diffraction could give rise to misleading artifacts in the image.

The present paper applies the electron diffraction technique to the study of the structure of three different types of twist grain boundaries in silicon, namely $\Sigma 1$ [001]; $\Sigma 1$ [111] and $\Sigma 3$ [111]. In addition the study provides a start to the cataloguing of diffraction effects characteristic of various types of known boundaries, for example, a twist boundary with a small superimposed tilt component. The aim of the latter part of this study is to facilitate the characterization of boundaries with unknown parameters using diffraction information.

2. Experimental Techniques

The bicrystals of silicon were manufactured using the hot-pressing technique described by Föll and Ast (1979). The technique is similar to that developed for gold by Schober and Balluffi and involves hot-pressing, at 1200°C and pressures of 0.1 Mpa, two or more slices of silicon in a hydrogen atmosphere. The silicon used was n-type and the slices were polished to give a mirror finish. Specimens were prepared for electron microscopy by cutting the bicrystal(s) at an angle of 25° to the boundary plane. After chemical thinning or ion milling the specimens were examined using a Siemens Elmiskop 102 electron microscope operating at 125 kV.

The majority of the observations which will be discussed in this paper were made by tilting the specimen in the microscope so that the electron beam was nearly normal to the boundary plane. This is different from the approach used by Carter, Donald and Sass (1979), where the foil normal was kept almost parallel to the electron beam. The current procedure has the advantage that no correction need be made in order to relate the periodicities observed in the image with those present in the boundary. Throughout this work the boundaries will be referred to as [001] or [111] twist boundaries to signify that the boundary plane is very close to the (001) or (111) planes, respectively, although if a tilt component is present this will not strictly be the case.

3. Experimental Results and Discussion

3.1 [001] Twist boundaries

3.1.1 Geometry of the reciprocal lattice

The structure of a small angle [001] twist boundary is expected to consist of two sets of orthogonal screw dislocations with Burgers vector, $\vec{b} = a/2 \langle 110 \rangle$ and spacing, p , as shown schematically in Fig. 1 (a), where the foil has been tilted so that the electron beam is parallel to \vec{n} , the normal to the boundary plane. The reciprocal lattice associated with such a boundary, which is inclined to the foil surface, is shown schematically in Fig. 1 (b). The dislocation network gives rise to an array of relrods parallel to \vec{n} , on a square lattice with spacing $1/p$, which contains the matrix reflections [Guan and Sass (1973a,b)]. The boundary is the same as that considered by Guan and Sass (1973a,b) except that \vec{m} , the foil normal, is not coincident with \vec{n} . Regions of the diffraction pattern close to the pairs of $2\bar{2}0$ and 400 reflections are shown in Figs. 1 c and d respectively, for small values and different signs of the excitation error, s_g . The spots labelled M_1, M_2 are associated with the two crystals and their positions relative to the related N_1, N_2 spots depend on the magnitude and sign of s_g : if the sign of s_g is reversed the M spots will move to the other side of their respective N spots. (It should be noted that for this geometry it is the M spot which moves as s_g is varied and not the N spot [cf. Carter, Donald and Sass (1979)]). The misorientation angle is related to the spacing of primary dislocations in Fig. 1 (a) by the formula (Read 1953)

$$\sin \theta/2 = \frac{|\vec{b}|}{2p} \quad (1)$$

As the misorientation angle increases, the magnitude of p decreases, until it no longer is physically realistic to talk about individual primary dislocations and p will be the O-lattice spacing [Bollmann (1970)].

In the next section it will be demonstrated that the ability to separate the N and M spots allows the extra spots arising from the periodic structure of

where the grain boundary is parallel to the foil surface, the N_1 , N_2 and M_1 , M_2 spots always superimpose, and because of this it is difficult to eliminate all possibility of double diffraction causing additional spots (Sass, Tan and Balluffi, (1975); Sass and Balluffi, (1976)). Carter, Donald and Sass (1979) demonstrated that double diffraction can be a factor even for inclined boundaries and can lead to the presence of spurious spots in many regions of the diffraction pattern.

3.1.2 Double diffraction analysis

Double diffraction becomes important when a strong matrix reflection, excited in the upper crystal, is rescattered by the lower crystal. In order to determine the new spots that can result from this process, it is necessary to translate 000 to the positions of the strong matrix reflections, which act as new incident beams. When this is done, other matrix reflections can be moved close to the Ewald sphere, resulting in new diffraction spots. In order to determine the influence of this process on the observed diffraction pattern, it is necessary to examine the three dimensional representation of the reciprocal lattice for the inclined grain boundary shown in Fig. 2.

In this figure the geometry of diffraction is shown for the [001] twist boundary in Fig. 1 (a). The situation illustrated is with the pair of $2\bar{2}0$ reflections on the Ewald sphere ($s_g = 0$). If crystal 1 is the upper crystal then the $2\bar{2}0_1$ reflection can be rescattered by the lower crystal. To determine what new spots can result from double diffraction, translate 000 to position $2\bar{2}0_1$ as shown by the solid arrow; 040_1 then moves to superimpose on $2\bar{2}0_1$, while 040_2 moves to the position shown by the dashed arrow and yields spots M_D and N_D . Since the reflections from the two crystals and the grain boundary lie on the same reciprocal lattice (related to the coincidence site lattice [Sass, Tan and Balluffi (1975), Sass

and Balluffi (1976)]), reflection 040_2 is moved to a position that is on the square reciprocal lattice of the boundary. If that position is cut by the Ewald sphere such that $s_g \neq 0$ then it can easily be seen that if N_D and M_D are both present, it is not possible to decide if N_D is real. Also when $s_g = 0$, M_D and N_D superimpose and it is not possible to decide if the observed spot is real or due to double diffraction. If, however, when $s_g \neq 0$ the N_D spot is observed to occur without an accompanying M_D spot, then it must be real i.e. associated with the grain boundary structure. It can thus be seen that double diffraction can produce arrays of relrods parallel to \vec{n} and \vec{m} , that yield spots lying on two lattices, one containing M_1 and M_2 (called the M lattice) and the other containing N_1 and N_2 (called the N lattice). The real grain boundary relrods, which are parallel to \vec{n} , will yield spots that lie on a lattice containing N_1 and N_2 . It is the presence of additional spots on the N lattice, *which are not paired to spots on the M lattice*, which is evidence for the periodic nature of the grain boundary structure.

It can further be seen for the geometry of Fig. 2, that while the observed N lattice will be square, the observed M lattice will be distorted away from being square. However if the angle between \vec{m} and \vec{n} is relatively small, as is the case here, then it will not be possible to detect easily the deviation of the M lattice away from being square.

3.1.3 Observations

To illustrate the features observed from an actual boundary of the type discussed above, a nominally $\Sigma 1$ [001] twist boundary will be examined in some detail. All of the boundaries to be discussed here were slightly off the ideal boundary plane and thus contained a measurable tilt component. This was because the faces of the single crystals could not be polished to be exactly (001) or (111). The influence of the tilt component on the experimental observations will be discussed later in this section.

Fig. 3 is a bright-field multibeam image (Föll and Ast, 1979) of a nearly pure twist $\Sigma 1$ [001] boundary with a 2.0° misorientation angle, which shows a square network associated with the two sets of screw dislocations which have a 10 nm spacing. Frequently the bright field images are much more complicated, as is illustrated in Fig. 4 (a), which shows a complex array of fringes with 3.0 nm spacing from a 3.0° boundary. A weak-beam dark-field image of this same area, recorded using the $\bar{2}20$ region of the diffraction pattern, is shown in Fig. 4 (b): one set of screw dislocations appears as a series of narrow lines with 6.0 nm spacing while the other set is out of contrast. The screw dislocation lines in Fig. 4 (b) are occasionally displaced (every ~ 45 nm) and these shifts are believed due to dislocations with an edge component which accommodate a small tilt of $\sim 1/4^\circ$ in the boundary. The direction and magnitude of the tilt component can be accurately determined for small angles by recording the diffraction patterns of both crystals on the same photographic plate. Two electron diffraction patterns from this boundary, also recorded close to the nearly common 001 pole, are shown in Fig. 4 (c and d), together with enlarged insets of several areas of the patterns. (The two patterns are related by a tilt approximately about the $2\bar{2}0$ axis.) Several of the insets in these figures are shown schematically and it can be seen that, in each case, the spots either lie on a fine lattice (o) or on a coarse lattice (•) and that the spacing of the coarse lattice is twice that of the fine lattice. The positions of the • spots relative to the o spots reverse when the sign of s_g is reversed (cf I and II) and this behavior agrees with the predictions in Fig. 1 (c and d): with the symbols o and • corresponding to the N and M lattices, respectively. The spacing of the N spots yields a twist angle of 3.1° which, according to equation 1, corresponds to an array of screw dislocations with spacing 7.1 nm, which is somewhat larger than the value of 6.0 nm measured from the dark field image in Fig. 4 (b).

It is frequently observed that spots on the N lattice do not have companion spots on the M lattice. This observation is in agreement with the predicted behavior of the extra spots from the grain boundary described in Fig. 2 and is direct evidence for the periodic nature of the boundary structure. The complex fringe pattern seen in Fig. 4 (a) is most likely the result of interference among the many reflections seen in the insets in Fig. 4 (c,d), which have been brought into the vicinity of the origin by double diffraction. Since many of the reflections in Fig. 4 (c,d) are the result of double diffraction, the image must contain Moiré fringes which provide no information about the boundary structure. It appears then that the diffraction pattern is the best source of unambiguous information about the actual boundary structure.

Conclusive proof that the extra spots on the N lattice result from relaxations in the grain boundary, and are not present when two single crystals are simply touching, can be obtained by studying the diffraction patterns from the interface shown in Fig. 5(a) which has a misorientation similar to those of the boundaries in Figs. 3 and 4. In the region shown, the area A of the interface is a grain boundary, since the weak-beam image shows images of one of the sets of screw dislocations with a measured separation of 7.0 nm; the dislocation line displacement occurs more frequently than in Fig. 4 (b) (18 nm spacing) and must be associated with a larger tilt component. The neighboring area B shows no evidence for a dislocation array; with only a fine set of fringes typical of a Moiré effect present with a measured 3.5 nm periodicity. This value is half that of the expected dislocation spacing predicted from Eqn. 1 for this boundary. Superimposed on both areas are thickness fringes associated with the inclination of the interface to the foil surface. The observed features can be explained by noting that where dislocations are not present the two crystals do not actually touch but are separated by a thin amorphous or glassy phase which is presumably SiO_2 . The amorphous region

is an artifact produced by the sintering technique used to manufacture the bicrystal.

Figs. 5 (b and c) show selected area diffraction patterns taken from the grain boundary and amorphous interface regions, respectively. The misorientation angle determined from the diffraction pattern is 3.1° which, according to equation 1, is consistent with a dislocation spacing of 7.1 nm. By comparing the diffraction patterns in the vicinity of the same matrix reflections from the two regions, it can be seen that the area of structured grain boundary gives rise to pairs of closely-spaced extra spots (arrowed) in addition to N and M spots while the non-structured interface gives rise to no extra spots. This is a direct proof that the extra reflections result from the grain boundary region. This observation demonstrates that the detection of M and N spots by themselves only shows that an inclined interface is present and gives no information on the structure of the interface. The pair of extra reflections lie along a line which has a different direction than that of the line joining the M and N spots, and which is normal to the array of lines across which the screw dislocations are displaced.

The origin of the pairs of extra spots in Fig. 5 (b) can be most clearly demonstrated by examination of the boundary shown in Fig. 6 (a), which is a 220 weak-beam image of another region of the same nominally $\Sigma 1$ [001] twist boundary in Fig. 5, misinterpreted by an extremely low angle grain boundary. In area A the structure of the boundary is similar to that shown in Fig. 5 (a) with the set of screw dislocations in contrast being periodically displaced by a coarse set of dislocations; in area B the coarse network is now parallel to one set of screw dislocations.

The diffraction patterns from regions A and B are shown in Figs. 6 (b and c), respectively: in both cases in the 220 region a pair of extra spots is

present between the N spots, and the direction of the line joining the two spots is normal to the coarse dislocation array in the region from which the diffraction pattern is taken. The separation of both sets of spots corresponds to a distance in real space of ~ 19 nm. It can therefore be seen, in this example, that the occurrence of a pair of closely spaced grain boundary reflections is related to the presence of a periodic array of dislocations with partly edge character which accommodates a tilt component superimposed on the twist boundary. It is interesting to note that Guan and Sass (1979) made a similar observation, on a large angle tilt boundary upon which was superimposed a small twist component, of the splitting of single grain boundary reflections into pairs.

Both the twist and the tilt components impose their own periodicity on the boundary. If, as is likely, these are not simple multiples of one another, the true periodicity of the boundary may be very large (100 nm or more). It seems more meaningful then to separate out the different components when discussing such a boundary, instead of concentrating on the correct (and possibly large) unit cell. An example of just such a boundary with a large unit cell in a polycrystalline foil was discussed by Carter, Donald and Sass (1979a, Fig. 3).

With previous analyses and observations as background, attention can now be focussed on a larger angle ($\sim 8^\circ$) twist boundary where the structure cannot be determined from the image. A bright-field image of this boundary recorded with both crystals set close to the 001 pole, is shown in Fig. 7 (a), together with an enlarged area in Fig. 7 (b) to show the faint square fringe pattern present. The fringes lie along the mean $\langle 110 \rangle$ directions and have a spacing of 1.3 nm (another set of fine fringes parallel to the mean $[100]$ direction is also present with a spacing of 0.9 nm). Another image of this boundary recorded slightly off the 001 pole is shown in Fig. 7 (c) and one set of fringes with 1.3 nm spacing and another set with 12.5 nm spacing are observed. A diffraction pattern from this area of the boundary is shown in Fig. 7 (d) together with insets of selected areas at greater magnification. Once again it can be seen

that there are pairs of extra reflections present which are located midway between the two N spots and that the line connecting these extra pairs of spots is not parallel to the NM direction. From the diffraction pattern it can be seen that when s_g changes sign, the M spots move from one side of the N spots to the other, while the extra pair of spots remains midway between the N spots. As a result of the analyses based on Figs. 1 to 6, it can be concluded from the presence of the extra pairs of spots which are symmetrically located midway between the N spots, both that the 8° twist boundary has a periodic structure and that a tilt component is present. The angle of misorientation is determined from the diffraction pattern to be 8.2° and the periodicity of the relaxation is expected to be 2.6 nm according to equation 1 (where \vec{b} is taken to be $a/2\langle 110 \rangle$). The 1.3 nm fringe spacing observed in Fig. 7 (a,b) must, therefore, be due to interference between the pair of M spots or the pair of N spots which are separated by a distance which is twice the spacing between an N spot and the midpoint of the pair of extra spots. The separation between the pair of extra spots corresponds to a periodicity of 12.8 nm which is close to the observed spacing of 12.5 nm. It is also observed that the direction of the line connecting the extra pair of spots is normal to the coarse fringe periodicity. For the boundary considered in Fig. 7 it can be concluded that, apart from the coarse fringe contrast associated with the tilt component, there is no other information in the image about the structure of the twist boundary.

It is interesting to note that the extra reflections from the 8° boundary are apparently much weaker relative to the matrix reflections than corresponding reflections from a similar boundary in Au [see Fig. 4 (b) of Guan and Sass (1973a)]. This difference may be due partly to the magnitude of the atomic displacements associated with the twist boundary in Si being smaller than in Au. Bristowe and Sass (1980) have found, from computer modelling studies, that the atomic displacements for twist boundaries with a given misorientation angle, vary

depending on the f.c.c. metal considered, and are particularly large for Au. Au is a much stronger scatterer of electrons than is Si which may also explain why the grain boundary spots appear stronger in Au than in Si.

Attempts were made to examine a boundary in the vicinity of the $\Sigma 5$ [001] misorientation ($\theta = 36.87^\circ$), but although evidence for secondary dislocations and a tilt component was obtained from the image (Carter, Föll, Ast and Sass, 1979), the diffraction pattern showed no extra effects related to the presence of a periodic structure. The volume of the grain boundary region is expected to decrease with increasing misorientation, since its thickness is expected to decrease with increasing misorientation [Cottrell (1953)]. If this is the case then it might be expected that the magnitude of scattering from a large angle boundary would be less than that from a small angle boundary. Indeed it was noted above that the intensity of the grain boundary reflections was quite low for the 8° boundary and, therefore, it is reasonable to expect that the intensity from the 37° boundary would be even lower, which may explain why it was not detected.

3.2 [111] Twist boundaries

3.2.1 Geometry of the reciprocal lattice

Three [111] twist boundaries are shown schematically in Figs. 8 (a, b, c.) Fig. 8 (a) shows a $\Sigma 1$ boundary consisting of an hexagonal array of pure screw dislocations with Burgers vector $a/2\langle 110 \rangle$ while Fig. 8 (b) shows the situation commonly observed in this boundary in silicon, which has a relatively low stacking fault energy; the configuration consists of nodes containing alternating extrinsic and intrinsic stacking faults. Fig. 8 (c) shows a $\Sigma 3$ [111] twist boundary with the same misorientation from exact coincidence as for the $\Sigma 1$ boundaries in Fig. 8 (a,b). This boundary can be formed by imagining the stacking fault energy to be zero in fig. 8 (b) and then adding a pure $\Sigma 3$ twin boundary to remove all the stacking faults.

Equation 1 can be used to relate the spacing of the dislocations shown in

Fig. 8 (a) to the angle of misorientation. In order to do this, two sets of orthogonal, pure screw dislocations must be chosen and these need have no relation to the actual dislocations present in the boundary. Equation 1 can be written as:

$$\sin \theta/2 = \frac{a}{y} \frac{\sqrt{3}}{4\sqrt{2}} \quad (2)$$

where a is the lattice constant, and y , the shortest periodicity for this boundary, is defined in Fig. 8 (a). The periodicity, y , is in the $\langle 110 \rangle$ direction and is thus expected to give rise to extra spots in the 220 region of the 111 plane in reciprocal space as shown in Fig. 8 (d). The extra spots will be a distance $1/y$ from the N spots and lie along $\langle 110 \rangle$ directions in a hexagonal array. The projected structure of the boundary has hexagonal symmetry and the formation of extended nodes will not alter this symmetry.

For the same misorientation the $\Sigma 3$ boundary will have a smaller unit cell in projection than the $\Sigma 1$ boundary as illustrated in Fig. 8 (c). Equation 2 will still hold but the shortest periodicity is now $x (=y/\sqrt{3})$ and is in the $\langle 112 \rangle$ direction. This structure will give rise to extra spots as shown in Fig. 8 (e); the distance between the extra spots is now equal to the distance between the N spots and the hexagonal array from the grain boundary structure is actually based on these N spots.

3.2.2 Observations

(a) $\Sigma 1$

Fig. 9 (a) shows a bright-field image from a $\theta=5.2^\circ$ boundary viewed at normal incidence; a fine hexagonal fringe pattern with spacing of 2.0 nm is clearly visible in the enlargement in Fig. 9 (b). The corresponding diffraction pattern is shown in Fig. 9 (c) where the approximately equal intensity of each spot of the pairs of 220 spots indicates that any tilt component which is present in this boundary is very small, as confirmed by observations on the Kikuchi lines. Examination of the enlarged 220 region in the inset shows that weak and strong extra spots are present close to the matrix spots but, because of the small value of s for the low index reflections, it is not possible to distinguish the M and N

spots. This information is necessary since the appearance of both strong and weak extra spots suggests that double diffraction may be influencing the diffraction pattern. The foil was then tilted away from the 111 orientation in order to weaken some of the matrix reflections, and the diffraction pattern shown in Fig. 9 (d) was recorded. In several of the enlarged insets the M spots can be clearly distinguished from the N spots and it can be seen that extra spots are present on the hexagonal N lattice in the positions predicted by Fig. 8 (d). The presence of these extra spots shows that the boundary has a periodic structure.

A 5.2° deviation from $\Sigma 1$ would give a Moiré fringe spacing of 2.2 nm for 220-type reflections, while the actual boundary periodicity is expected to be 3.7 nm. The appearance, direction and 2.0 nm spacing of the hexagonal fringe pattern in Fig. 9 (a,b) confirms that it is a Moiré effect resulting from the interference of pairs of 220-type reflections and other double diffraction spots with the same spacing. Thus the image contains no information on the structure of the boundary, which has been shown to be periodic from the diffraction pattern. It is interesting to note that many of the strong extra spots present in the vicinity of each pair of 220-type spots in Fig. 9 (c), disappear with the small tilt to Fig. 9 (d), indicating that they and similar reflections close to the origin are due largely to double diffraction. It is these reflections in the vicinity of the origin that are producing the strong fringe contrast in Fig. 9 (a,b).

In certain of the insets in Fig. 9 (d), where s_g is relatively large and the N spots are easily identified, the M_1 and M_2 spots are split into pairs (See the white arrows). Close examination shows that the M spots are actually split in two different directions. By comparing the diffraction patterns and the image it can be seen that the direction of the line joining a particular pair of spots is normal to the thickness fringes in the corresponding grain. This suggests that the splitting of the M spots is due to the foil not having parallel surfaces

but instead being wedge-shaped. Each matrix reflection can be considered to have two \vec{m} relrods passing through it, with a relrod being normal to each of the foil surfaces (de Ridder, Van Landuyt, Gevers and Amelinckx 1970). This effect is only likely to be observed experimentally when both the wedge angle and s_g are relatively large. This observation does emphasize the importance of being able to identify the N sp² which are not influenced by the surface of the thin foil but depend only on the plane of the boundary.

Careful examination of the diffraction patterns in Figs. 9 (c and d) shows the presence of forbidden spots (see F), which are indexed as $1/3(224)$ -type. These spots were not observed in the single crystal diffraction patterns taken from the Si crystals adjacent to the boundary and, therefore, they must be associated with the grain boundary region. These spots are also observed from the 1° twist boundary shown in Fig. 10 (a). This boundary shows a complex array of images of Shockley partial dislocations and Moiré fringes due to unsintered regions. In region A the boundary consists of extended nodes similar to those shown in Fig. 8 (b); one set of partial dislocations is out of contrast having $\vec{g} \cdot \vec{b} = 0$. Figure 10 (b) shows a tilt sequence of diffraction patterns going from (110) to (111) to (112). The forbidden spots are clearly seen in the (111) pattern (see white arrow) and after tilting through a large angle about the $2\bar{2}0$ axis to the (112) orientation, it can be seen that the forbidden spots are still present, though their positions have changed slightly. Further tilt to the (110) orientation causes the forbidden spots to move into the positions of Si reflections. Thus it is seen that the forbidden spots close to 000 are due to elongation into relrods of the 111-type reflections. Since the 111-type reflections above and below the (111) reciprocal lattice plane, lie on lines normal to this plane which pass through $1/3(224)$ -type positions, it can be deduced that the relrods are normal to the (111) plane.

Information on the origin of the forbidden $1/3(224)$ -type reflections was obtained from a study of the small angle twist boundary with a large tilt component in

Fig. 11 (a,b). The weak-beam image in Fig. 11 (a) clearly shows a rectangular network of dislocations and, in agreement with this, the extra diffraction spots present in Fig. 11 (b) lie on a rectangular lattice (which is slightly distorted). The rectangular network is apparently the result of the interaction of the edge dislocation array due to the tilt component with the hexagonal dislocation array of the twist boundary. In other twist boundaries which have only a small tilt component stacking faults are probably present at the dislocation nodes (see e.g. area A of Fig. 10 and Fig. 10 of Föll and Ast 1979). There is no evidence for stacking faults being present in the boundary in Fig. 11 while stacking faults were identified for the boundary in Fig. 10. The absence of both stacking faults and forbidden reflections for the boundary in Fig. 11 and their presence for the other (111) twist boundaries suggests that the presence of stacking faults and forbidden reflections from the boundaries are linked together [these forbidden reflections can also occur when the specimen is very thin (Lynch 1971)]. Since the stacking fault is extremely thin, it is expected that the Si reflections will be elongated to give relrods normal to the fault (see e.g. Clarebrough and Forwood 1976). Thus the relrods associated with forbidden spots in Figs. 9 and 10 are believed due to the elongation into relrods normal to the boundary plane, of the 111 Si reflections above and below the 111 reciprocal lattice plane. As further confirmation of the link between stacking fault and relrod, it should be noted that the forbidden reflections are absent from all the [100] observations in Figs. 3 to 7, where there is also no evidence in the image for the presence of stacking faults. As noted before, the grain boundary displacement field will give rise to relrods, whose length is inversely related to the magnitude of the thickness of the boundary (Carter, Donald and Sass, 1980). It can be concluded that the relrods due to the grain boundary are considerably shorter than the relrods due to the stacking faults, since in the case of the [001] twist boundary, the 111 reflections do not exhibit long relrods, while

in the case of the $[111]$ twist boundary with stacking faults present, the 111 reflections do exhibit long relrods. The observed diffraction patterns from the $[111]$ twist boundaries behave as if the effects due to the stacking faults are present in addition to the effects due to the grain boundary. This is an interesting experimental observation because the stacking faults are an integral periodic part of the grain boundary structure, and it might have been expected that the length of the relrods would be influenced by the overall displacement field of the boundary, not just the local effects at the stacking faults.

It is interesting to note in the (111) pattern in Fig. 10 (b) that, in addition to the forbidden spots, there are also diffuse spots in an approximately hexagonal array around the Si matrix spots. On tilting about the $2\bar{2}0$ axis it is seen that the diffuse spots along this axis remain, indicating that they do not result from double diffraction and must be real. The disappearance of the diffuse spots lying along other $\langle 110 \rangle$ directions in the 111 plane indicates that they are not due to relrods. It is suggested that these spots, which lie on a reciprocal lattice with one-quarter the spacing of the Si reciprocal lattice, may be associated with the coherent precipitates occasionally found in these boundaries (see Fig. 14 (b), Föll and Ast 1979).

(b) $\Sigma 3$

Fig. 12 (a,b) shows a weak-beam dark-field image and the diffraction pattern from a $\Sigma 3$ boundary with $\sim 1.7^\circ$ misorientation. The image shows a fine fringe pattern which exhibits hexagonal symmetry in different regions. The inset in the diffraction pattern shows an array of spots lying on the N lattice in the positions predicted in Fig. 8 (e). Since these extra spots are not associated in general with M spots, it can be concluded that they are not due to double diffraction (see section 3.1.2) and their presence, therefore, demonstrates that the boundary structure is periodic. Measurements on the diffraction pattern yield a spacing of 6.4 nm. It is difficult to determine the periodicity from the image,

since it is not uniform in appearance. The fringes running parallel to [220] appear to have a somewhat smaller spacing of 5.0 nm. An interesting point to note is that the Moiré fringes associated with a small deviation from exact $\Sigma 3$ coincidence will have the same spacing as the screw dislocations if these are present, although of course the presence of the Moiré fringes would not give any information on the structure of the boundary. The forbidden weak $1/3(224)$ -type spots are again observed (see white arrow), and in this case are believed to be related to the presence of the twin interface (see e.g. Clarebrough and Forwood 1976).

4. Conclusions

The images from twist grain boundaries contained in Si bicrystals are frequently complex and contain Moiré fringes that provide no information on the actual boundary structure. An analysis of the reciprocal lattice associated with these boundaries has made it possible to separate out real extra reflections resulting from the periodic structure of the boundary, from spurious effects due to double diffraction. It was possible to show that all the $\Sigma 1$ [001], $\Sigma 1$ [111] and $\Sigma 3$ [111] twist boundaries examined had periodic structures. The $\Sigma 5$ [001] boundary gave rise to no detectable diffraction effects, however, the presence in the image of a periodic array of secondary dislocations demonstrated the periodic nature of the boundary. It is possible to detect small tilt components in these boundaries by the splitting into pairs of the extra reflections from the boundary.

Acknowledgements

The authors would like to thank Dr. B. Kolbesen from Siemens AG Germany for providing the silicon used in this study.

This work was supported by the National Science Foundation under Grant No. DMR 76-24180 and through the Materials Science Center of Cornell University, and by the Department of Energy under Contract No. E-1-76-S-02-2894.

References

- Bollmann W., 1970, Crystal Defects and Crystalline Interfaces
(New York: Springer-Verlag)
- Bristowe, P.D. and Sass, S.L., 1980, Acta. Met. in press
- Carter, C.B., Donald, A.M. and Sass, S.L. 1979 Phil. Mag. A39, 533
- Carter, C.B., Donald, A.M. and Sass, S.L., 1980, Phil. Mag. in press
- Carter, C.B., Föll, H., Ast, D.G., and Sass, S.L., Proc. 37th Annual Meeting EMSA, 1979.
(Claitor's Publishing Div., Baton Rouge, La.) P. 686
- Clarebrough, L.M. and Forwood, C.T., 1976, Phys. Stat. Sol. (a) 33, 355
- Cosandey, F., Komem, Y. and Bauer, C.L. 1978 Phys. Stat. Sol. (a) 48, 555
- Cottrell, A.H., Dislocations and Plastic Flow in Crystals, 1953, p. 83
(Oxford University Press).
- Föll, H. and Ast, D.G., 1979, Phil. Mag. A39, 589.
- De Ridder, R., Van Landuyt, J., Gevers, R. and Amelinckx, S., 1970, Phys. Stat. Sol. 42, 645.
- Guan, D.Y. and Sass, S.L., 1973 a,b, Phil. Mag. 27, 1211, 1225
- Guan, D.Y. and Sass, S.L., 1979, Phil. Mag. A39, 293
- Lynch, D.F., 1971, Acta.Cryst. A27, 399
- Read, W.T. 1953, Dislocations in Crystals (McGraw-Hill)
- Sass, S.L. and Balluffi, R.W., 1976, Phil. Mag. 33, 703.
- Sass, S. L., Tan, T.Y. and Balluffi, R.W., 1975, Phil. Mag. 31, 559
- Schober, T. and Balluffi, R.W., 1969, Phil. Mag. 20, 511
- Schober, T. and Balluffi, R.W., 1970, Phil. Mag. 21, 109
- Schober, T. and Balluffi, R.W., 1971, Phys. Stat. Sol. (b) 44, 103
- Thölén, A.R., 1970, Phys. Stat. Sol. (a) 2, 537

List of Figure Captions

Figure 1

- a) Illustrating the geometry of a bicrystal containing a twist grain boundary which is inclined to the foil surface. The screw dislocation spacing is p , the foil normal is \vec{m} , and the grain boundary normal is \vec{n} .
- b) The schematic reciprocal lattice for the bicrystal in (a). The extra grain boundary relrods are indicated by rods passing through filled in spheres.
- c) The electron diffraction patterns expected in the $2\bar{2}0$ region, for opposite signs of s_g .
- d) The electron diffraction patterns expected in the 400 region for opposite signs of s_g .

Figure 2

- a) The intersection of the Ewald sphere with the reciprocal lattice in Fig. 1 (b), which illustrates the effect of a double diffraction process on the appearance of the electron diffraction pattern in the vicinity of the 220 region. M_D and N_D are produced by a double diffraction process involving the $2\bar{2}0$ and 040 regions of reciprocal space.
- b) The electron diffraction pattern produced in the 220 region of (a). The grain boundary reflection shown results from a grain boundary relrod midway between 220_2 and 220_1 which was not included in (a) in order to avoid confusion in the diagram.

Figure 3

Bright-field multibeam image of 2° $[001]$ twist boundary.

Figure 4

Observations on a $\sim 3^\circ$ $[001]$ twist boundary.

- a) Bright-field image
- b) Weak-beam dark-field image of the same area as in (a), formed with $2\bar{2}0$ reflections.

c,d) Electron diffraction patterns from the boundary in (a,b).

The two patterns are related by a tilt about the $2\bar{2}0$ axis.

Figure 5

Observations on a $\sim 3^\circ$ [001] twist boundary

- a) Weak-beam dark-field image formed with $2\bar{2}0$ reflections.
- b) Diffraction pattern from area A which exhibits dislocation like contrast.
- c) Diffraction pattern from area B which exhibits fringe contrast.

Figure 6

Observations on another region of the $\sim 3^\circ$ [001] twist boundary shown in

Figure 5.

- a) Weak-beam dark-field image formed with 220 reflections.
- b,c) Diffraction patterns from areas A and B respectively. Note that the direction of the arrowed pair of reflections is normal to the set of lines across which the screw dislocations are displaced. Three pairs of extra spots are present in each inset.

Figure 7

Observations on a $\sim 8^\circ$ [001] twist boundary.

- a) Bright-field image.
- b) Enlargement of (a) showing a square fringe pattern with a 1.3 nm spacing.
- c) Different part of the same boundary in (a,b) after a small change in the foil orientation. The inset shows a fringe pattern with 1.3 nm spacing.
- d) Diffraction pattern obtained from the area shown in (c) but for different imaging conditions.

Figure 8

The geometry of three [111] twist boundaries.

- a) $\Sigma 1$, large stacking fault energy.
- b) $\Sigma 1$, medium stacking fault energy (as found for Si).
- c) $\Sigma 1$, zero stacking fault energy or $\Sigma 3$, with the same angle of misorientation.
- d) 220 region of the diffraction pattern expected for (a) and (b).

- e) 220 region of the diffraction pattern expected for (c).

Figure 9

Observations on a $\sim 5.2^\circ$ [111] $\Sigma 1$ twist boundary.

- a) Bright-field image.
- b) Enlargement of (a).
- c) Diffraction pattern corresponding to (a,b).
- d) Diffraction pattern from the same area as (a), with the foil tilted to weaken the 220-type reflections.

Figure 10

Observations on a $\sim 1^\circ$ [111] $\Sigma 1$ twist boundary.

- a) Weak-beam dark-field image formed with $\bar{2}02$ reflections.
- b,c,d) Series of diffraction patterns related by a tilt about the $[1\bar{1}0]$ axis from the boundary in (a). The arrows in (c,d) point out reflections at the $1/3(224)$ -type positions.

Figure 11

Observations on a small angle [111] $\Sigma 1$ twist boundary with a large tilt component.

- a) Weak-beam dark-field image formed with $2\bar{2}0$ reflections.
- b) Diffraction pattern corresponding to (a).

Figure 12

Observations on a $\sim 1.7^\circ$ [111] $\Sigma 3$ twist boundary.

- a) Weak-beam dark-field image formed with $2\bar{2}0$ reflections.
- b) Diffraction pattern corresponding to (a).

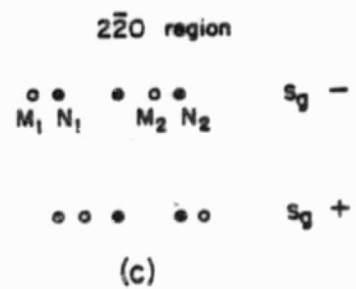
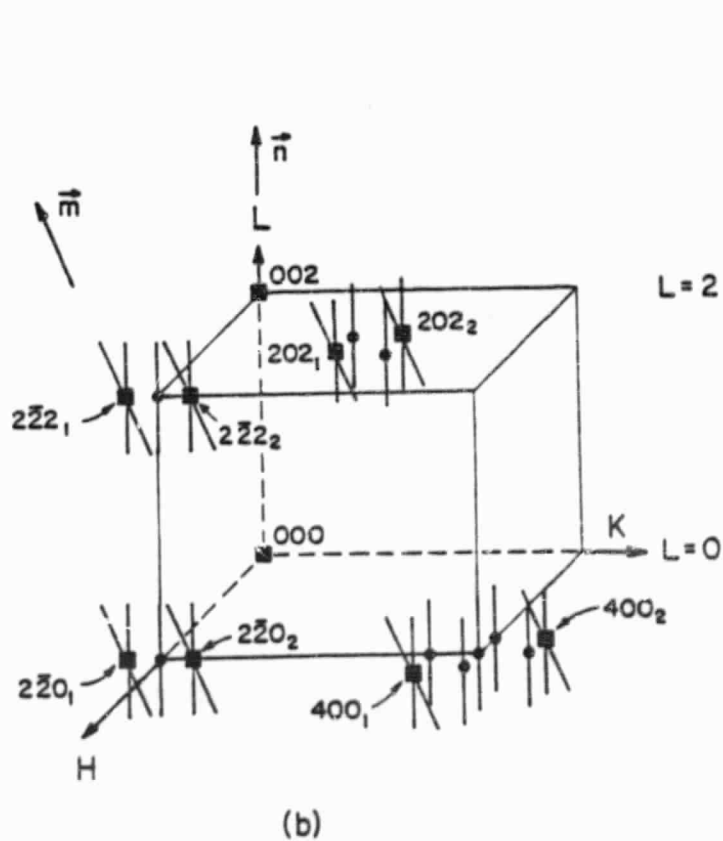
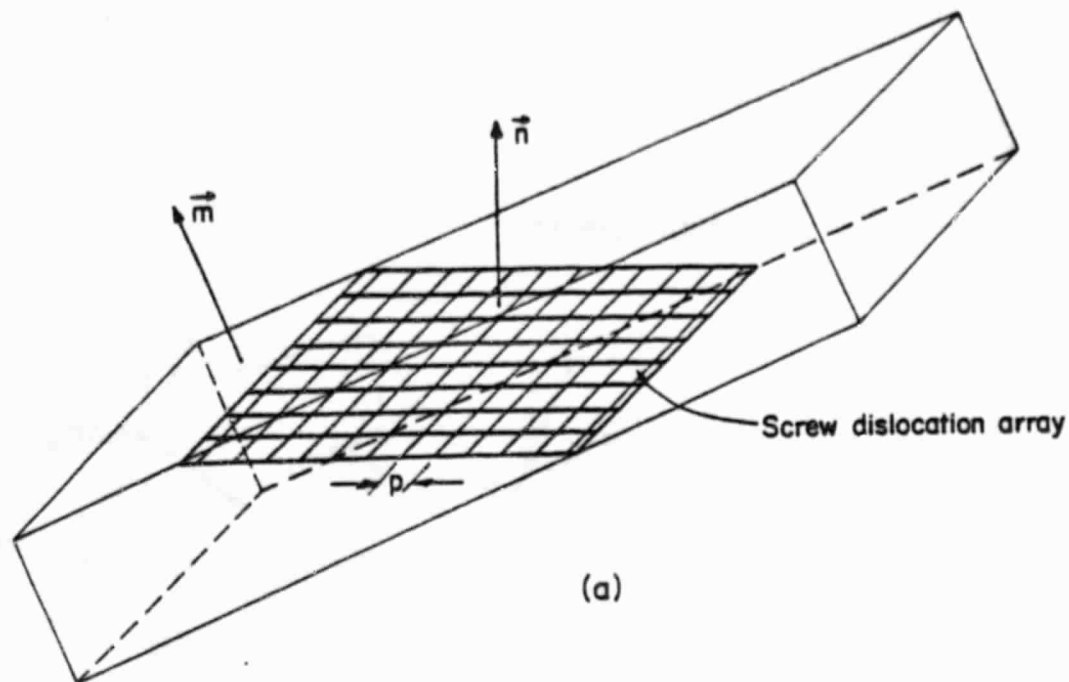


Figure 1

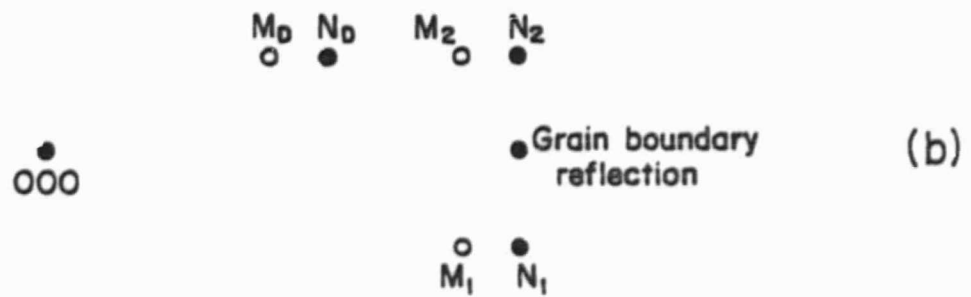
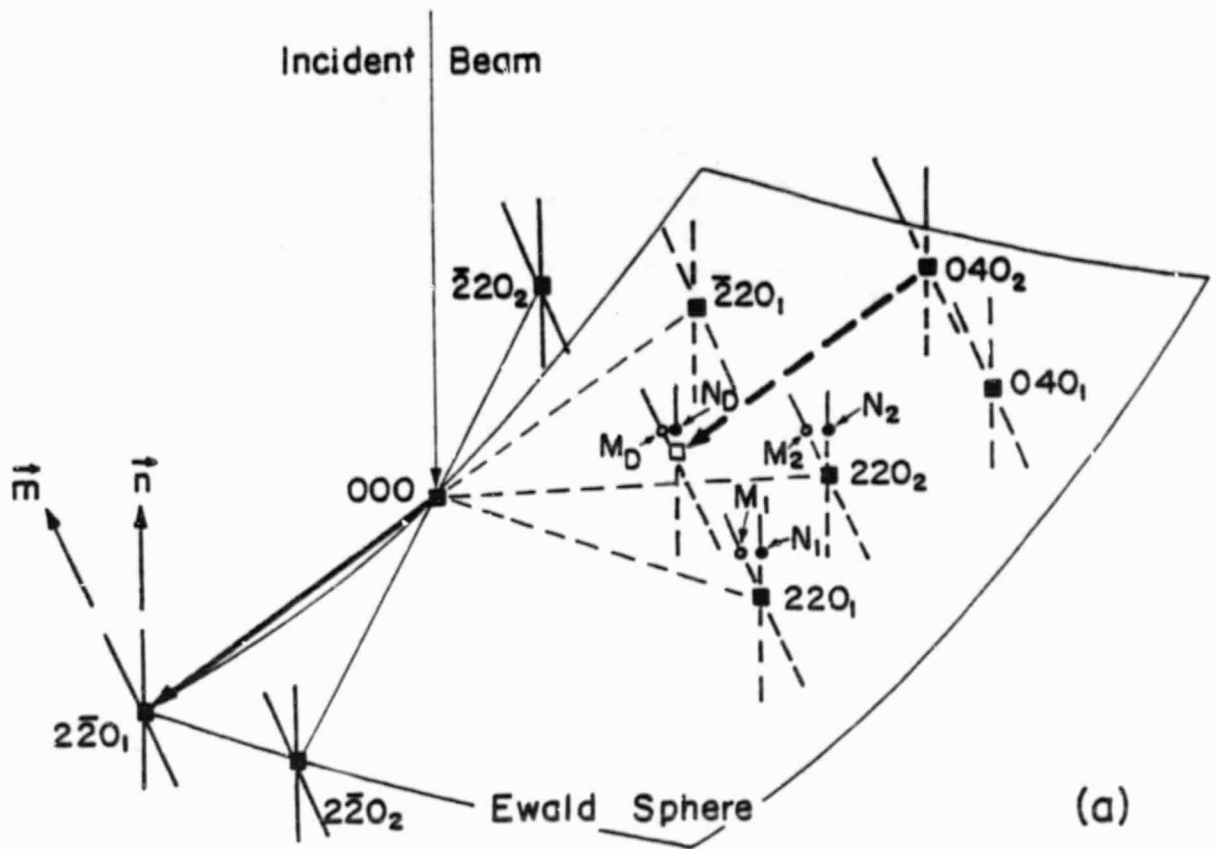


Figure 2

ORIGINAL PAGE IS
OF POOR QUALITY

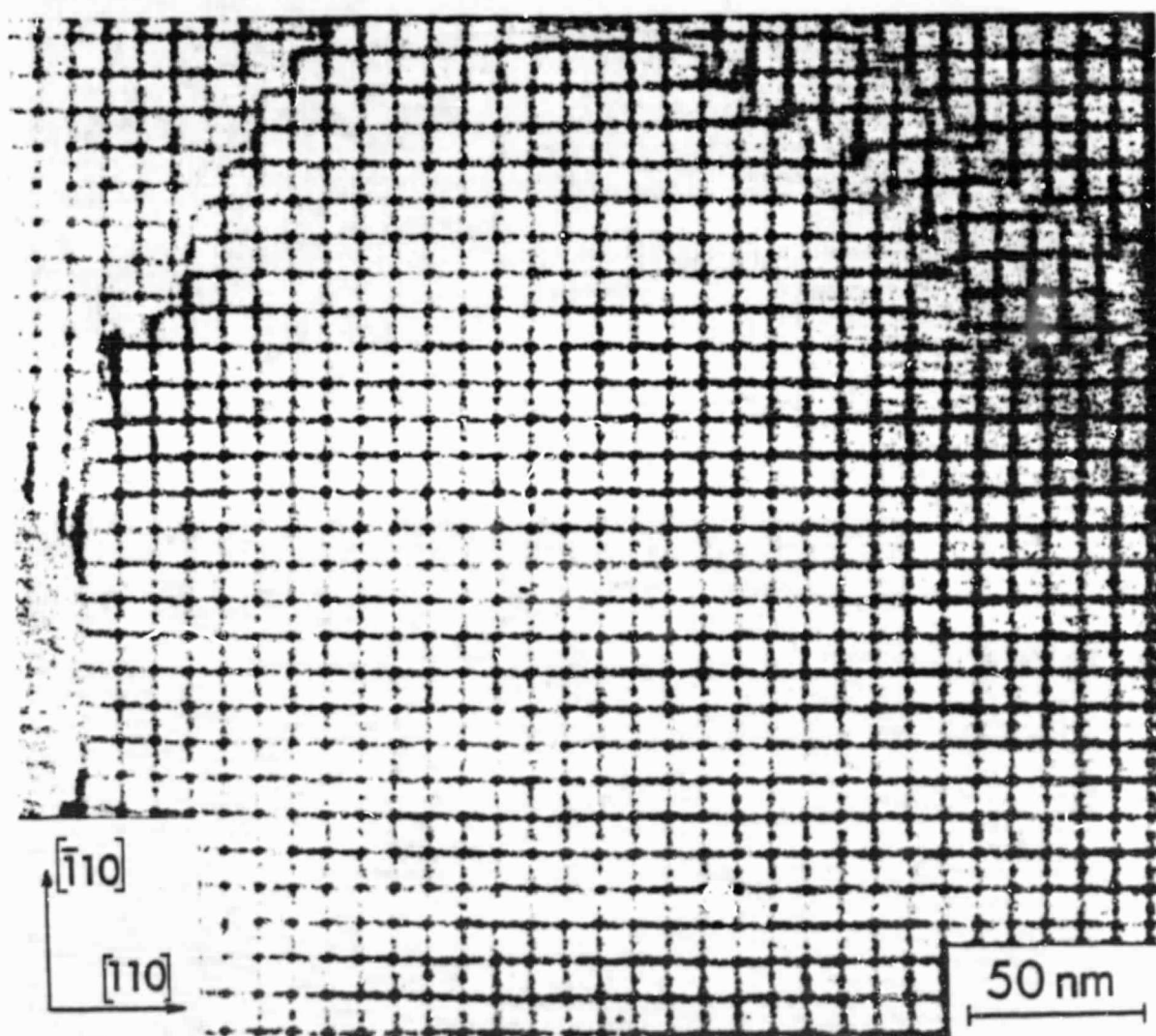
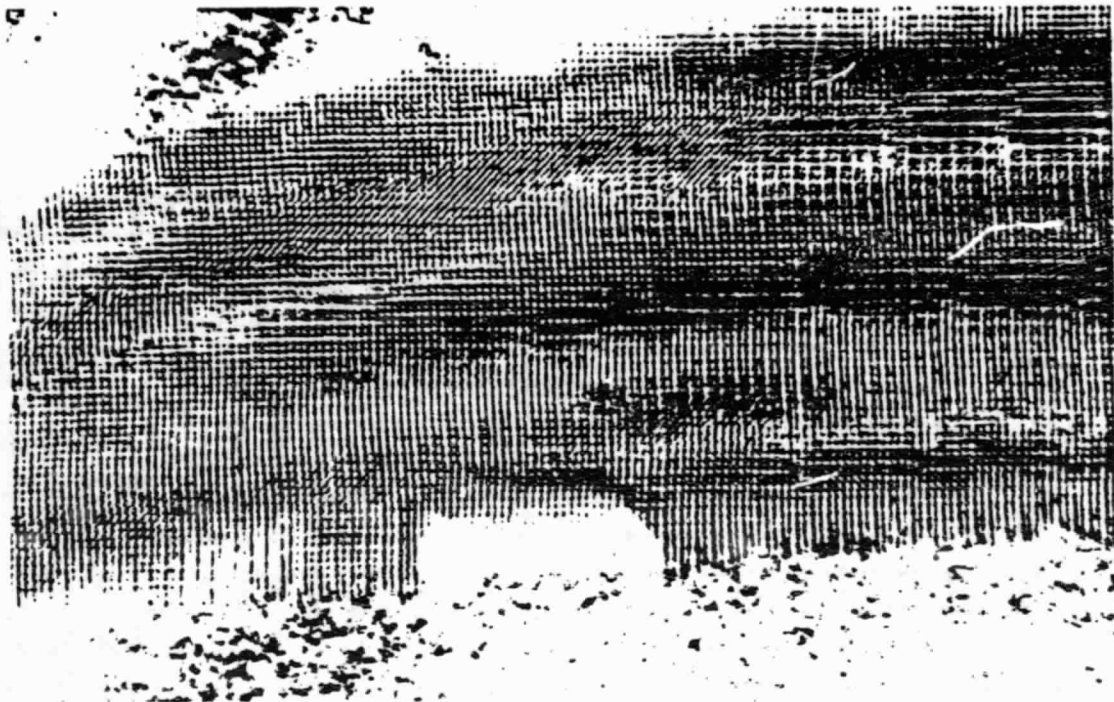
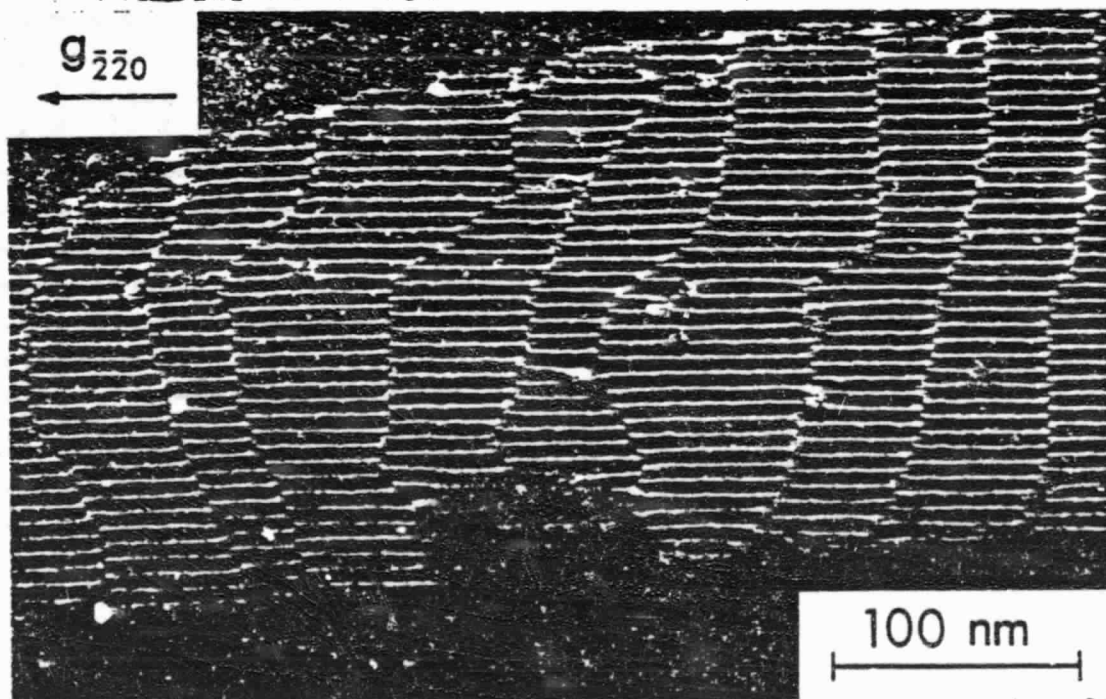


Figure 3

ORIGINAL PAGE
BLACK AND WHITE PHOTOGRAPH



(a)



(b)

Figure 4

ORIGINAL PAGE
BLACK AND WHITE PHOTOGRAPH

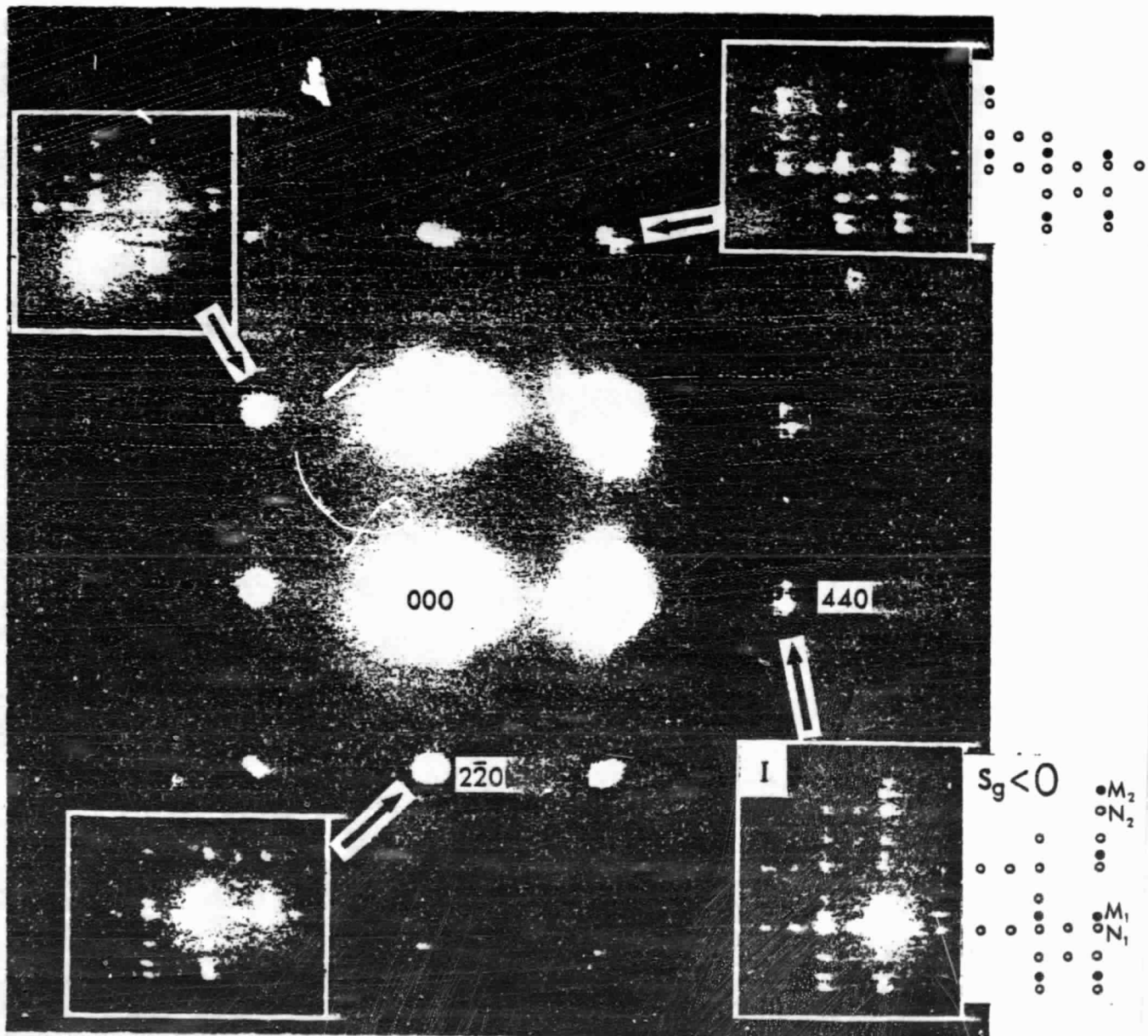


Figure 4(c)

ORIGINAL PAGE
BLACK AND WHITE PHOTOGRAPH

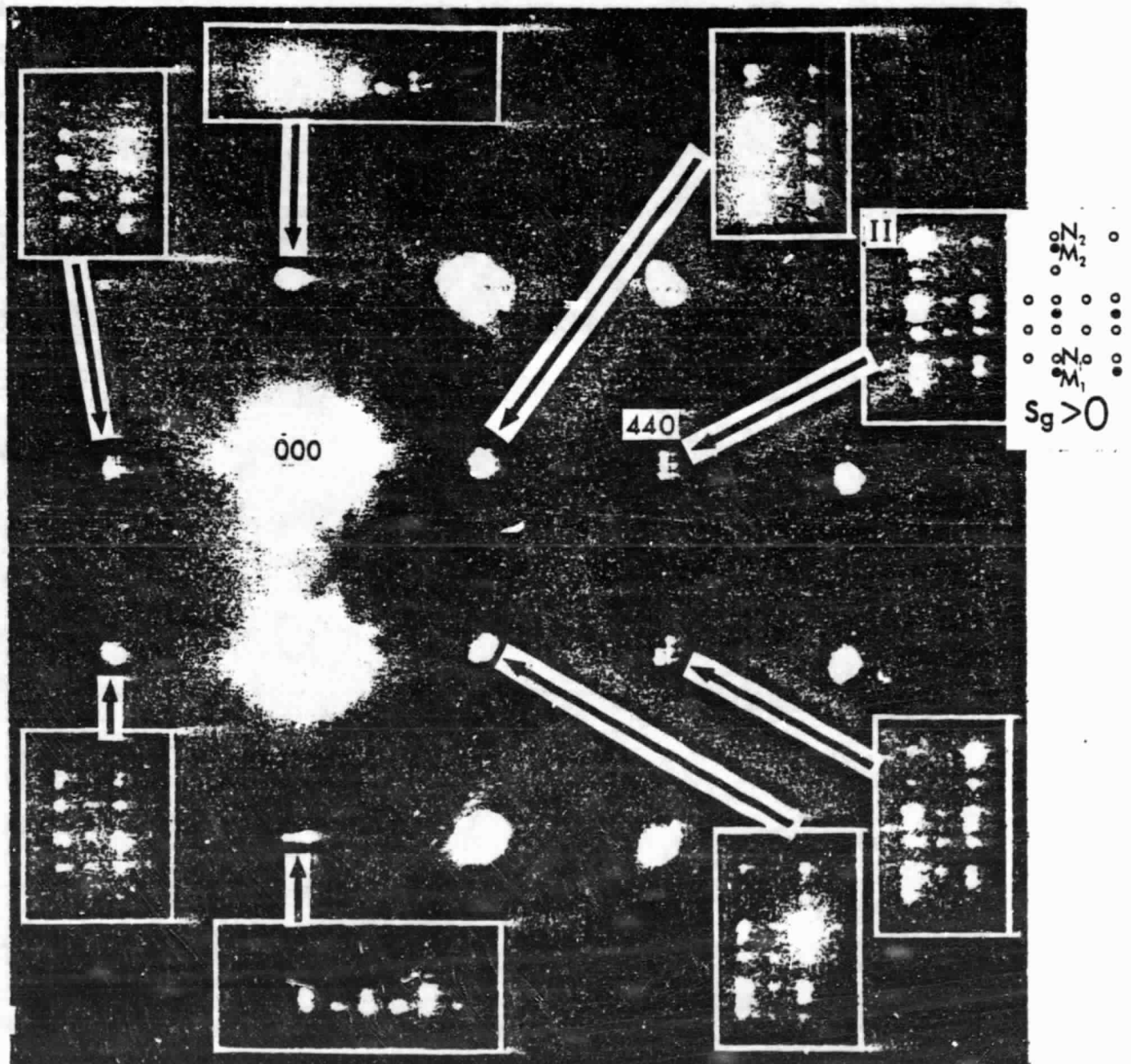


Figure 4(d)

A 28

ORIGINAL PAGE
BLACK AND WHITE PHOTOGRAPH

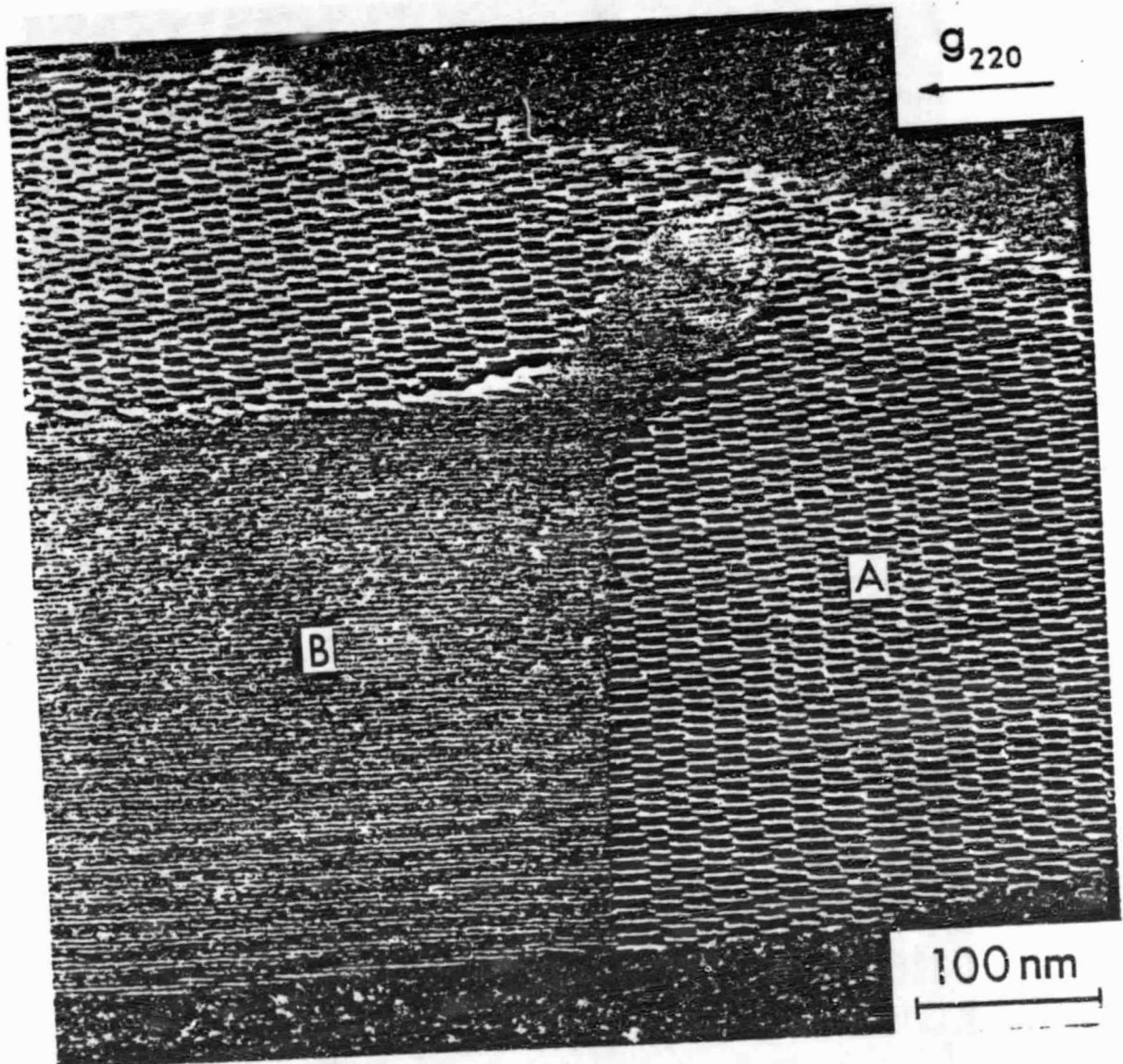
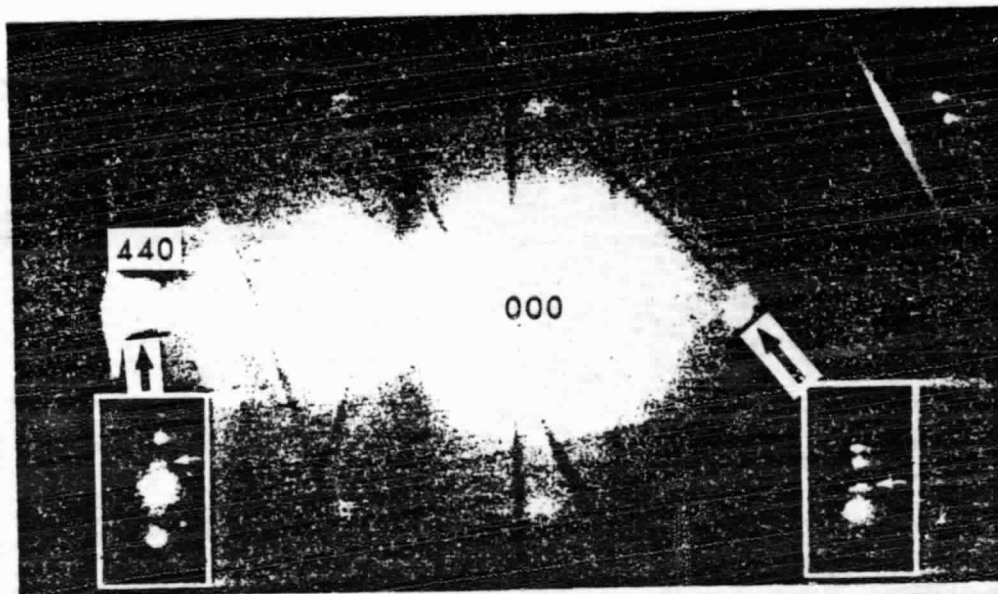
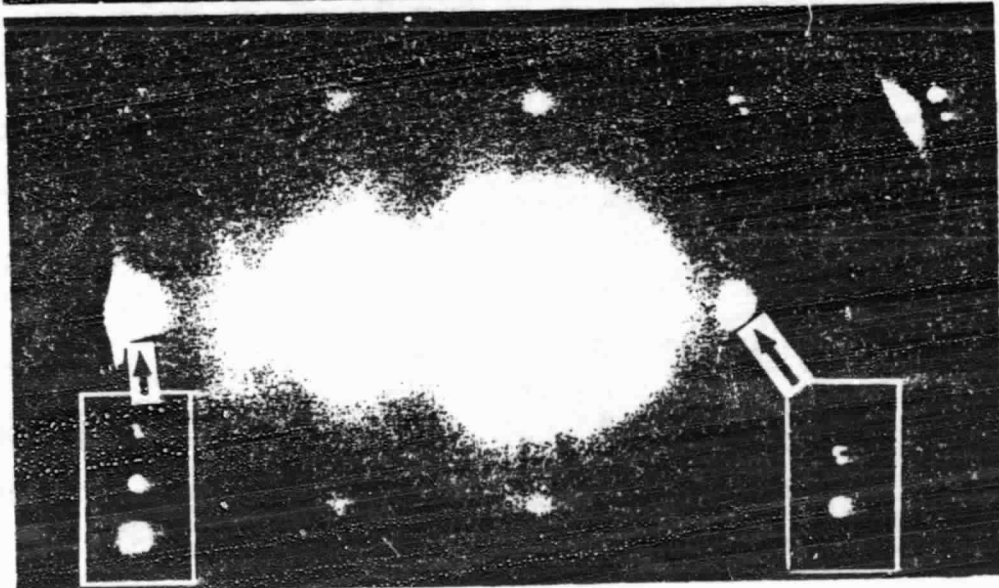


Figure 5(a)

ORIGINAL PAGE
BLACK AND WHITE PHOTOGRAPH



(b)



(c)

Figure 5

ORIGINAL PAGE
BLACK AND WHITE PHOTOGRAPH

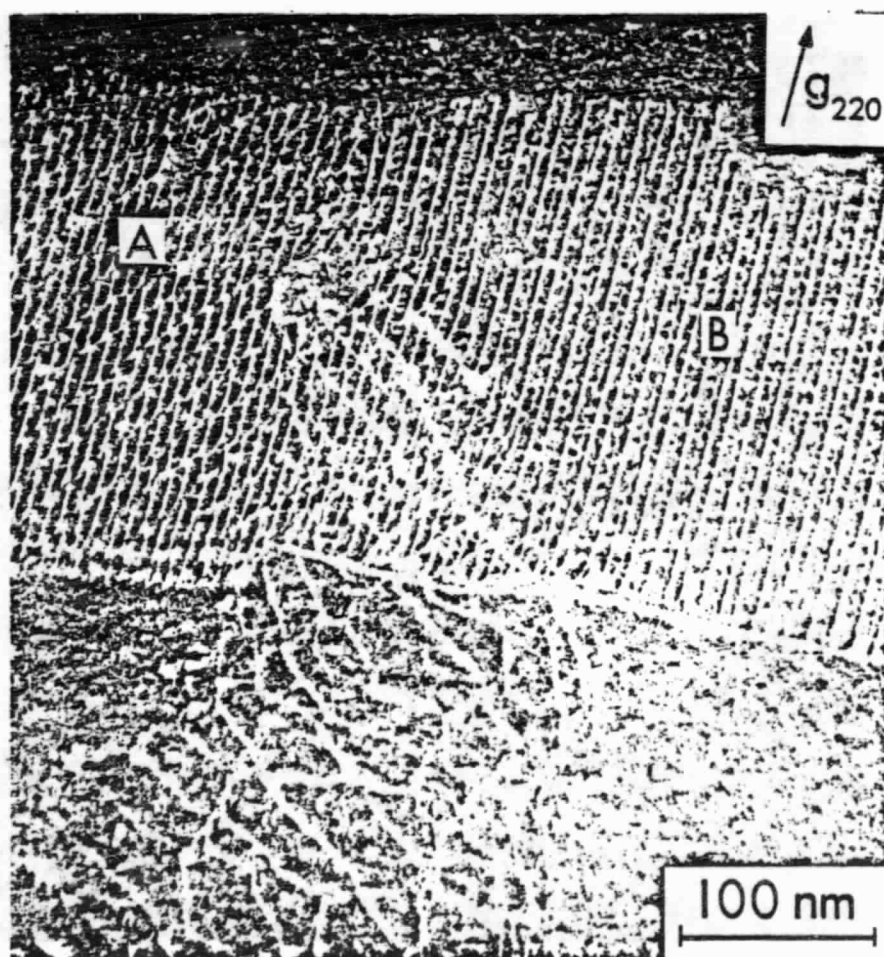
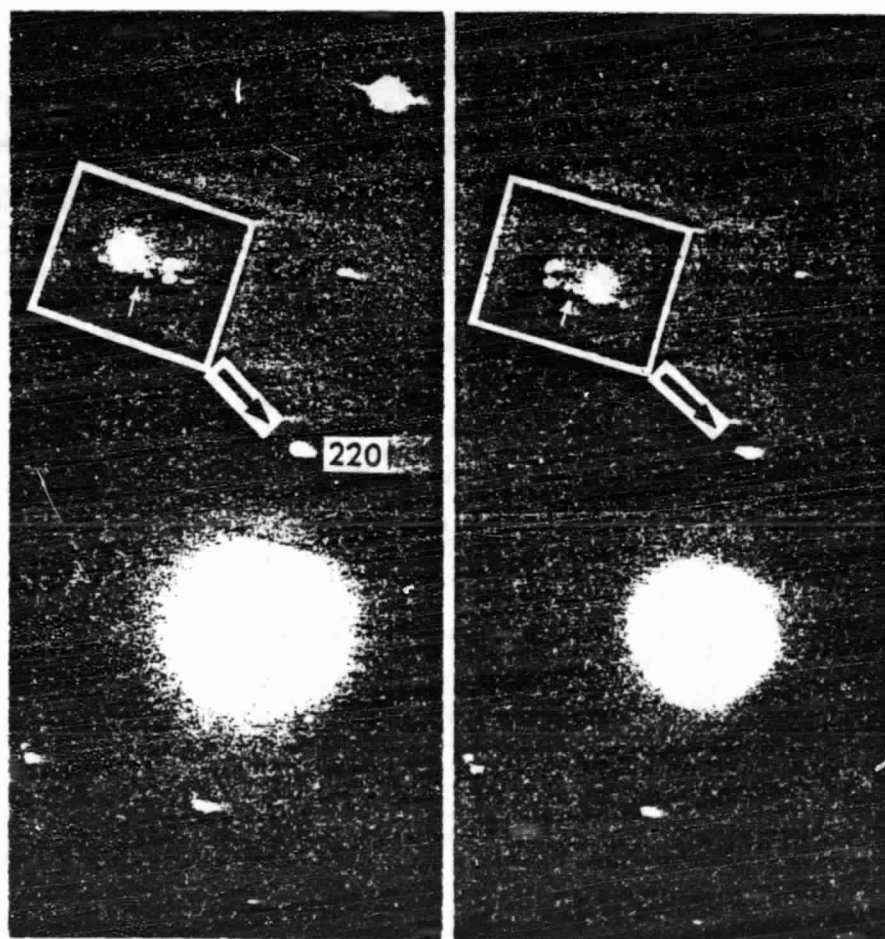


Figure 6(a)

ORIGINAL PAGE
BLACK AND WHITE PHOTOGRAPH



(b)

(c)

Figure 6

ORIGINAL PAGE
BLACK AND WHITE PHOTOGRAPH

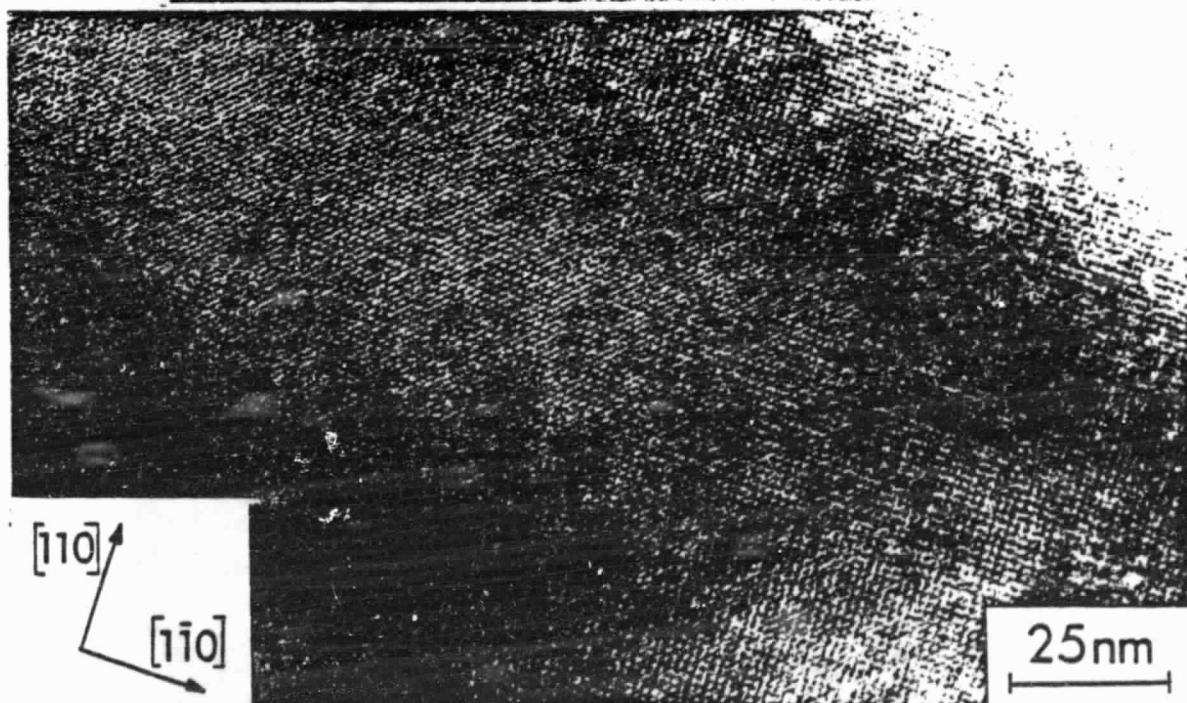
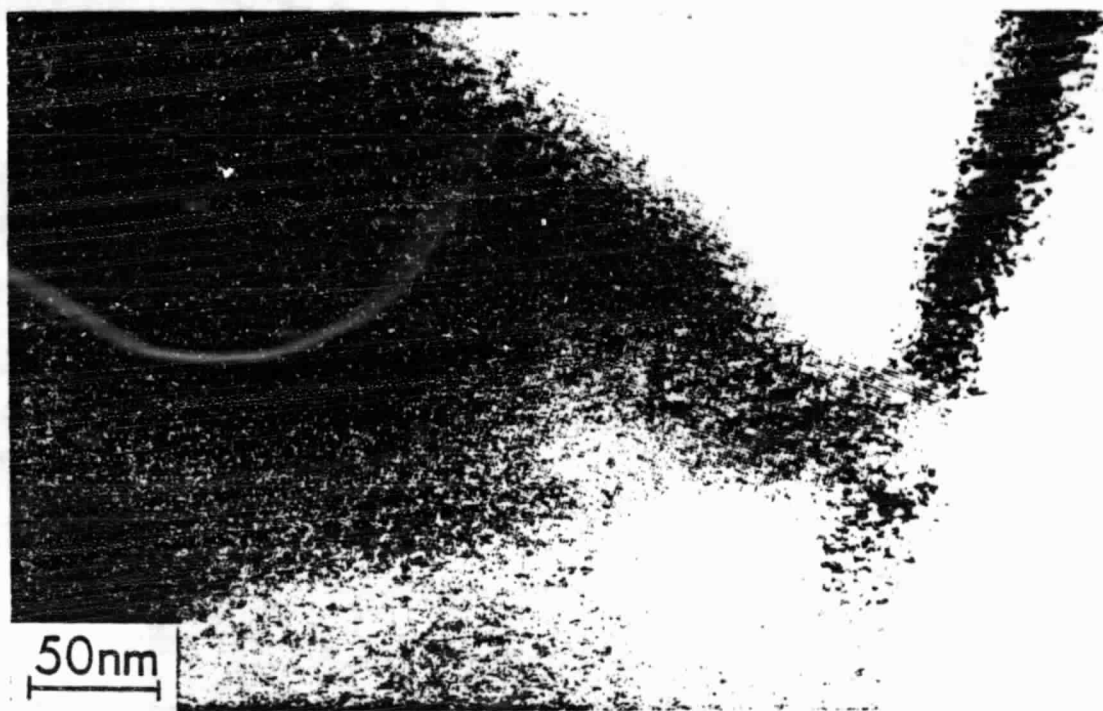


Figure 7

ORIGINAL PAGE
BLACK AND WHITE PHOTOGRAPH

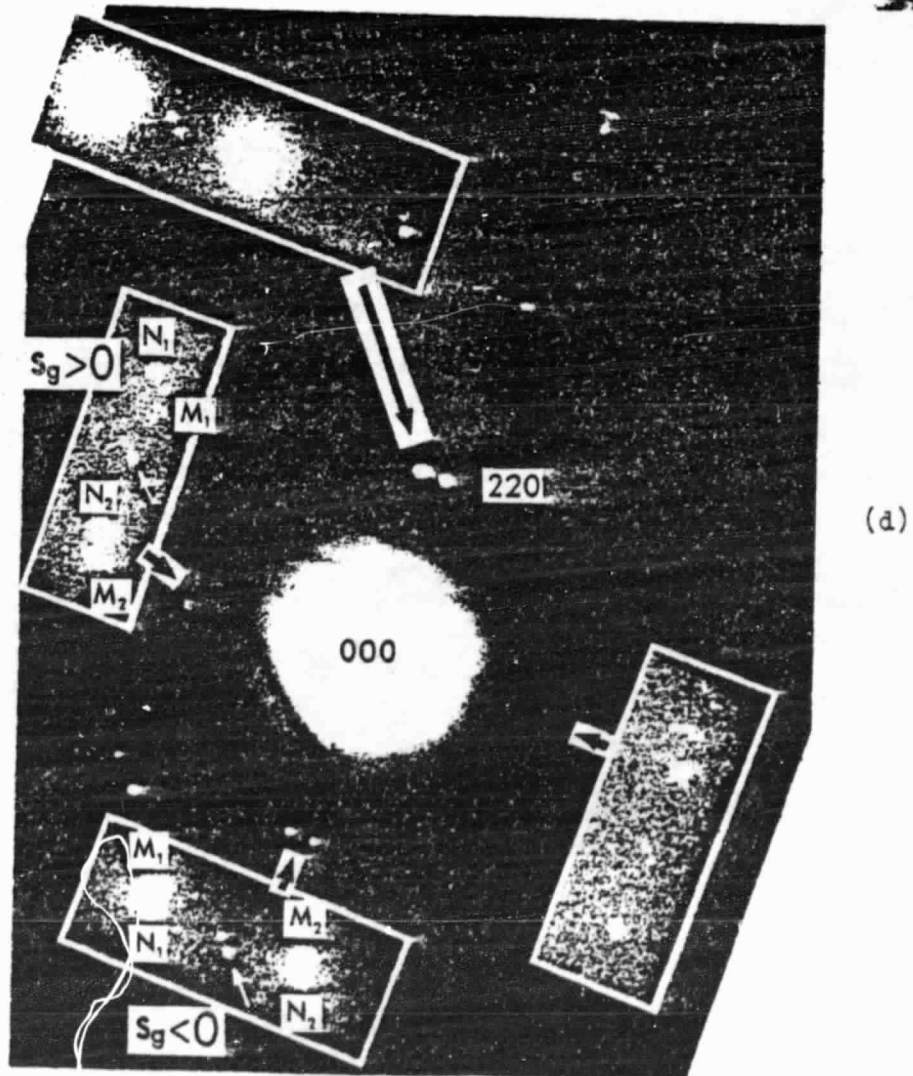
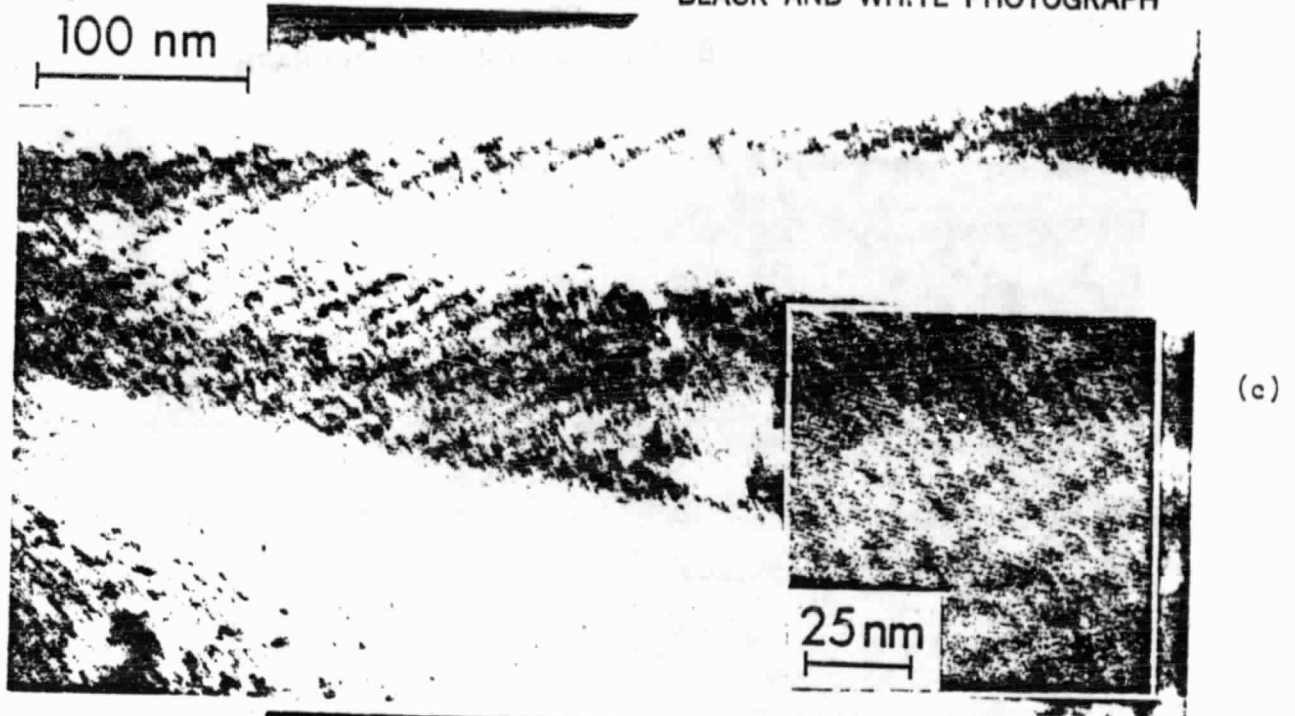


Figure 7

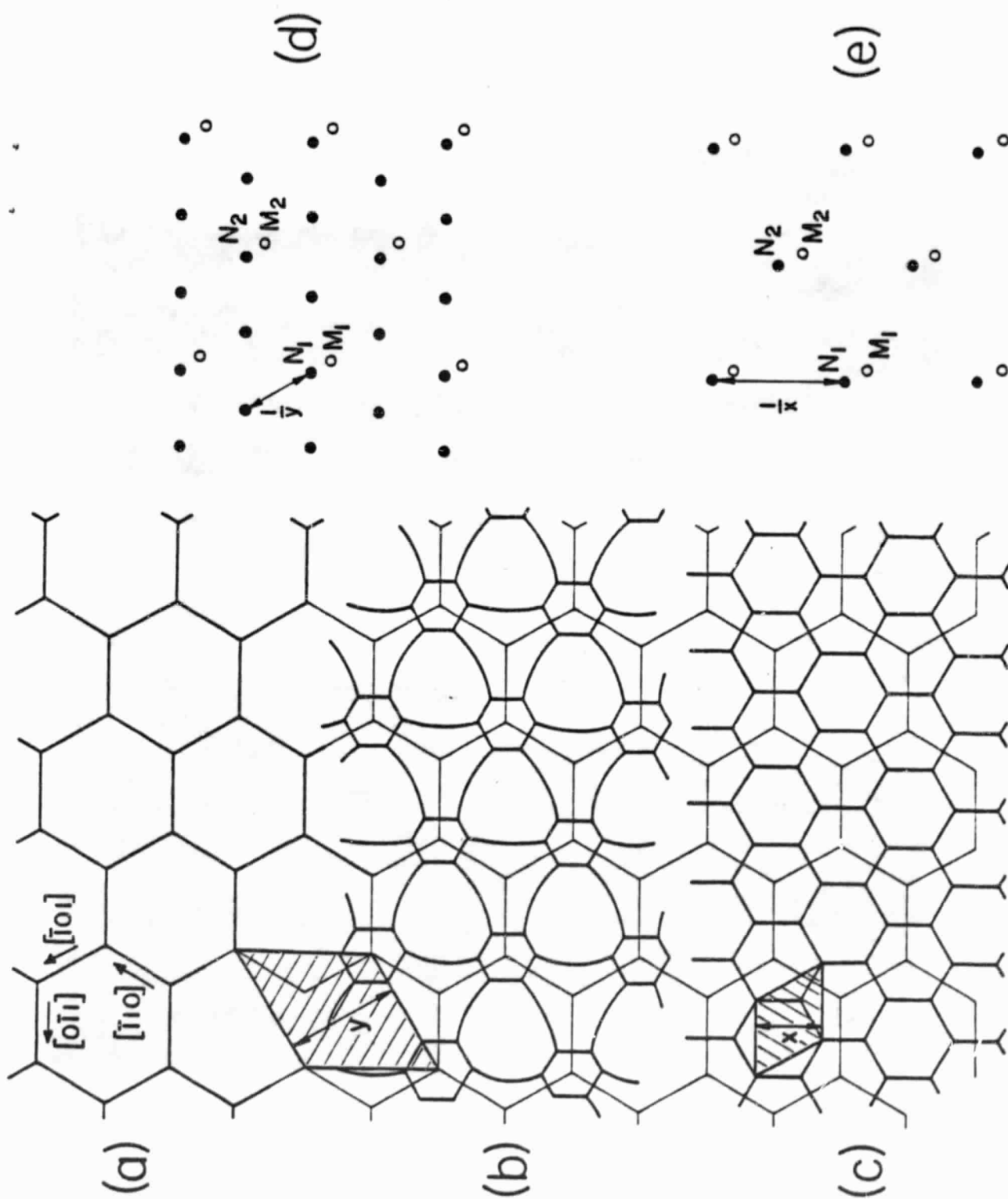


Figure 8

ORIGINAL PAGE
BLACK AND WHITE PHOTOGRAPH

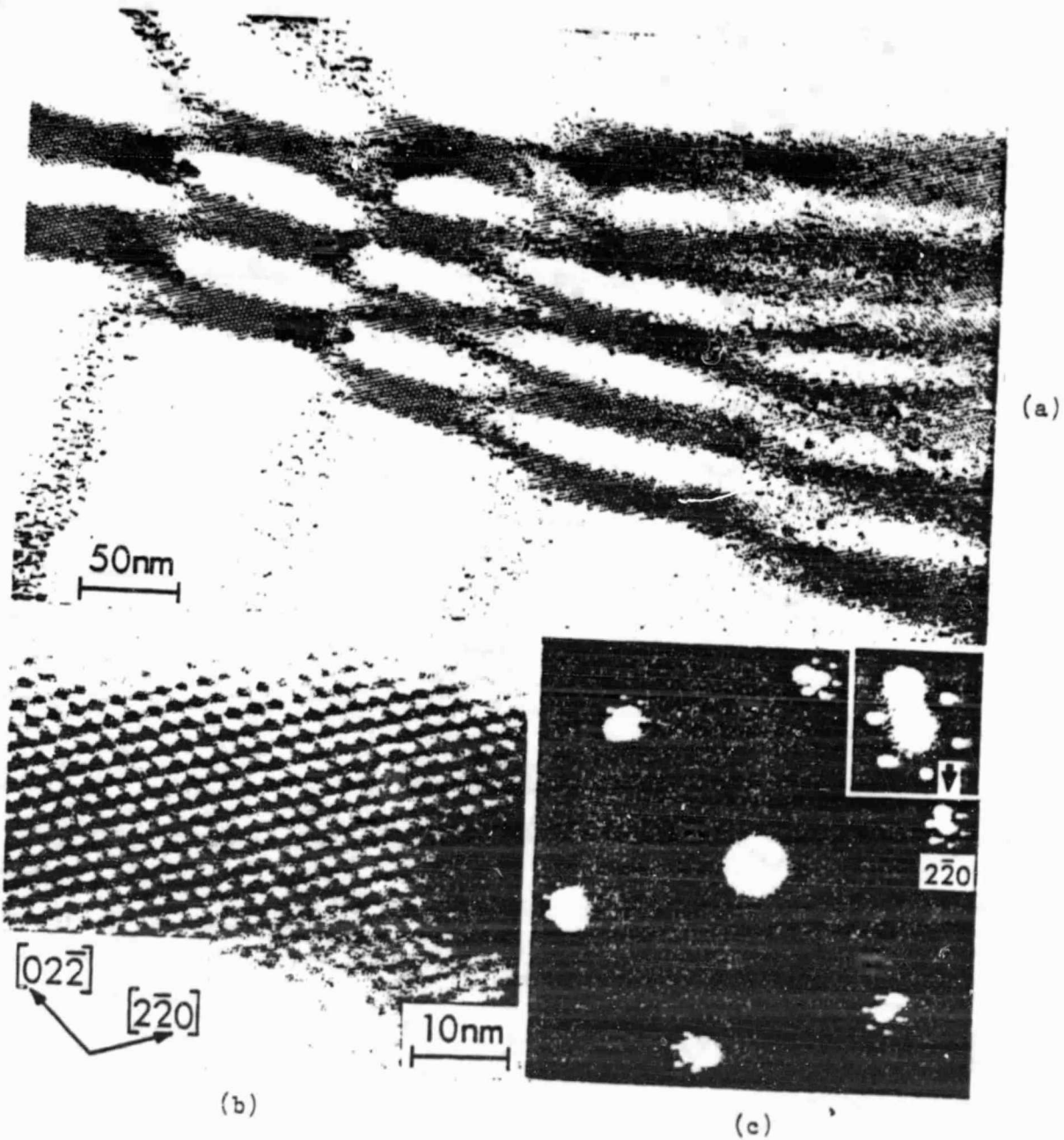


Figure 9

ORIGINAL PAGE
BLACK AND WHITE PHOTOGRAPH

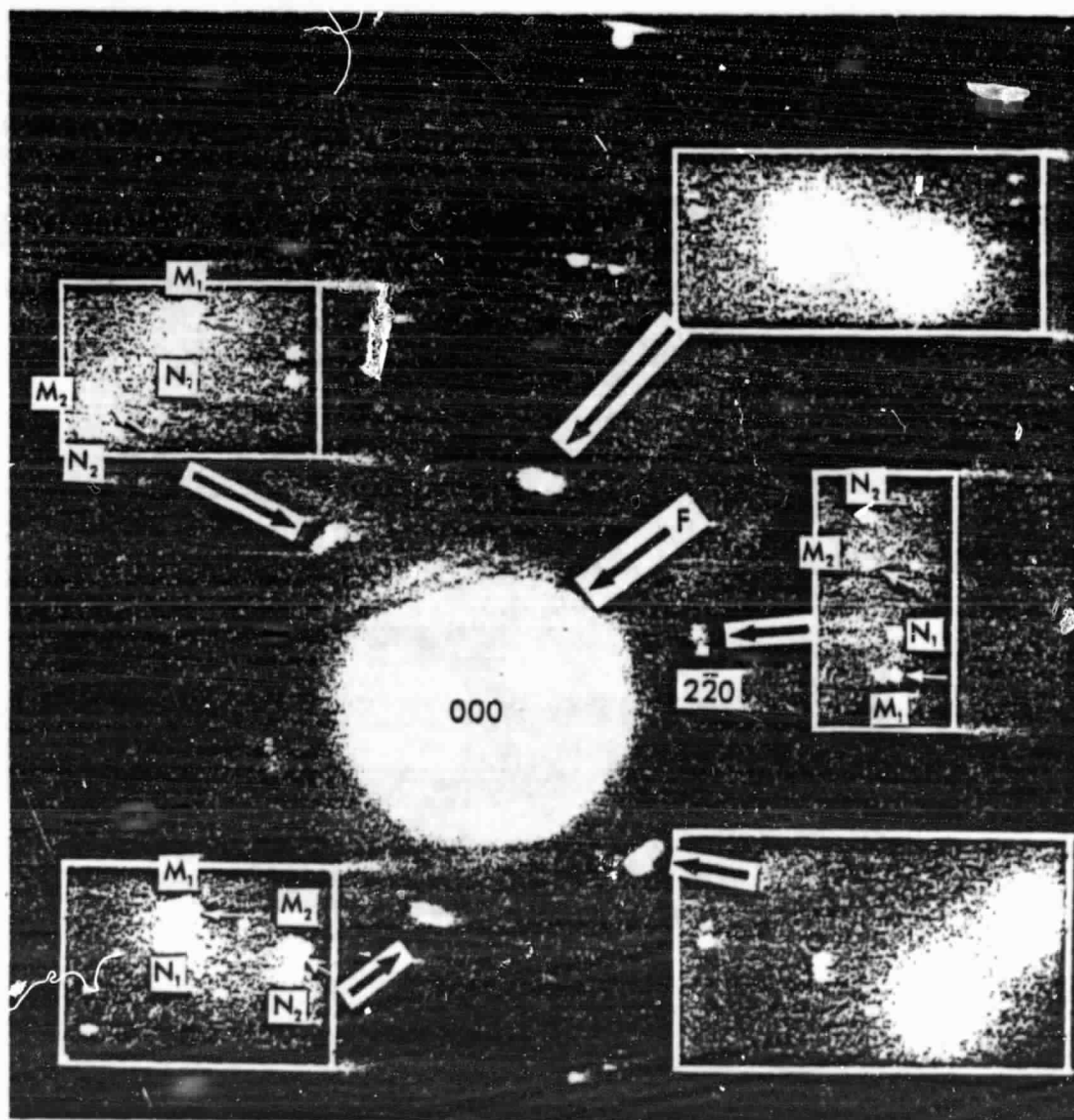


Figure 9(d)

ORIGINAL PAGE
BLACK AND WHITE PHOTOGRAPH

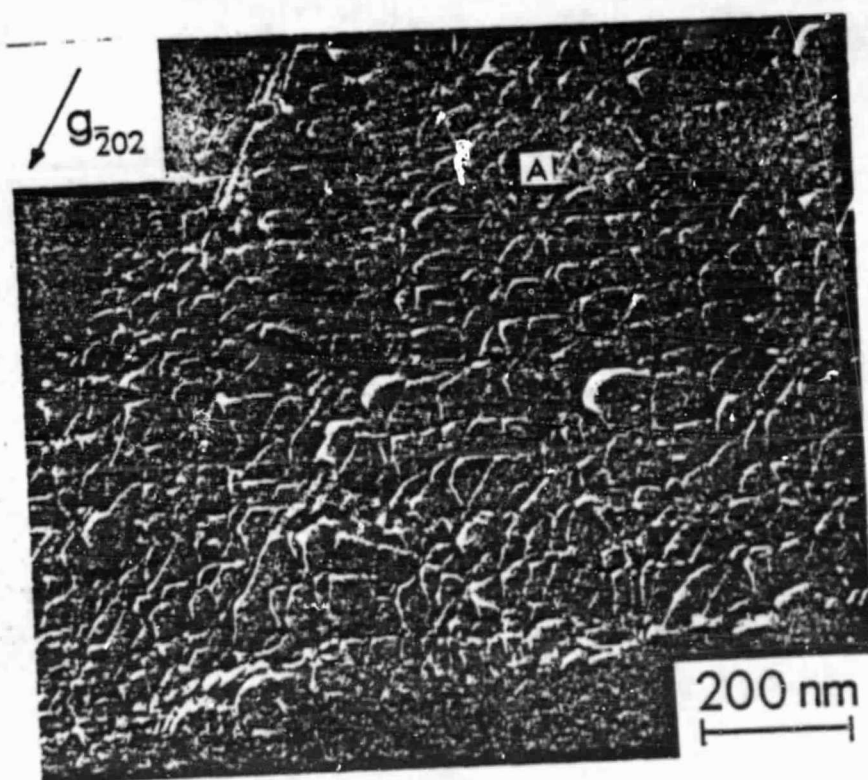


Figure 10(a)

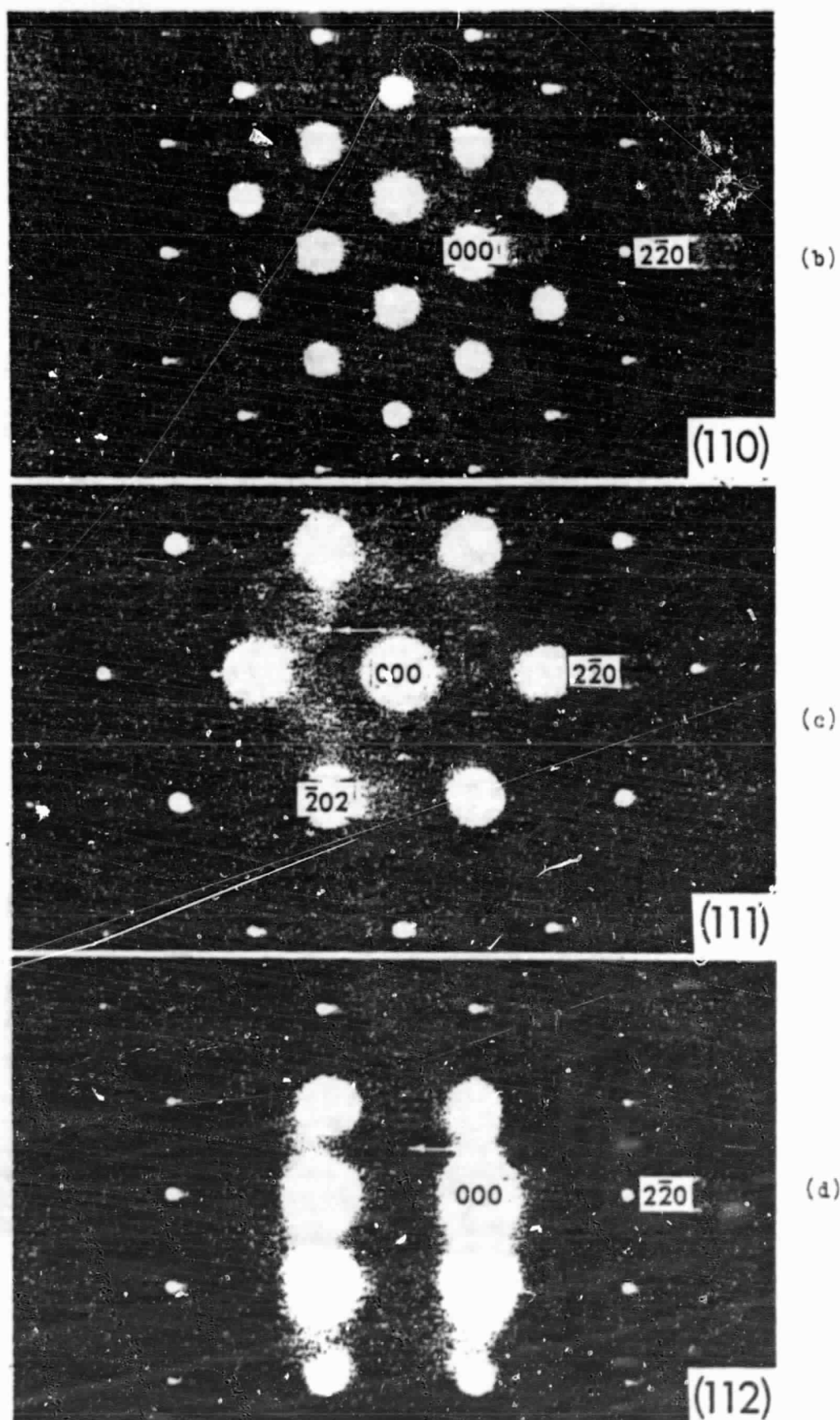
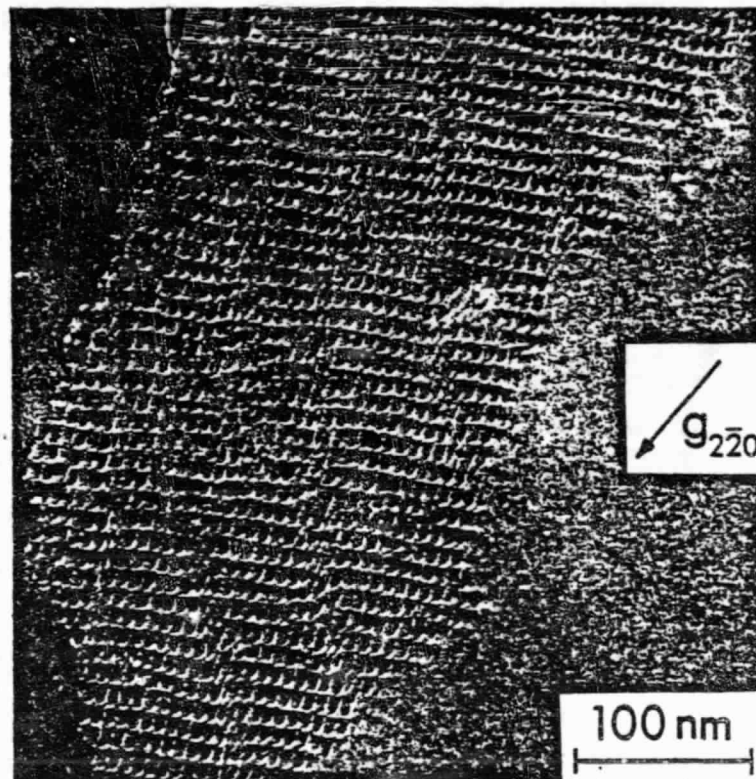
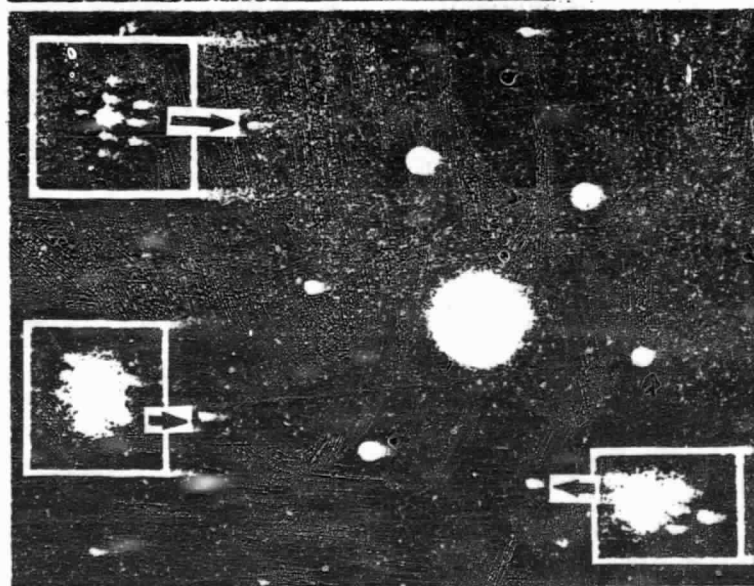


Figure 10

ORIGINAL PAGE
BLACK AND WHITE PHOTOGRAPH



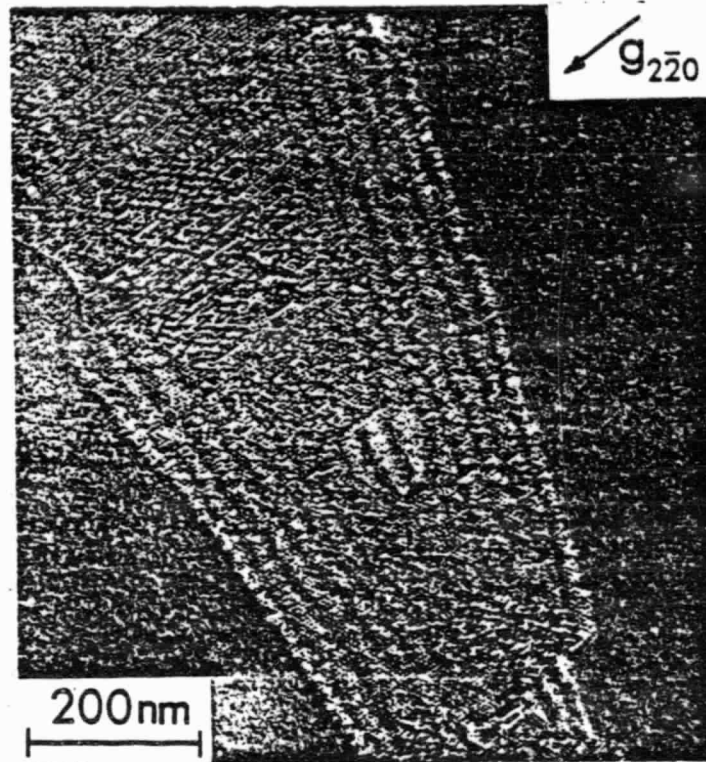
(a)



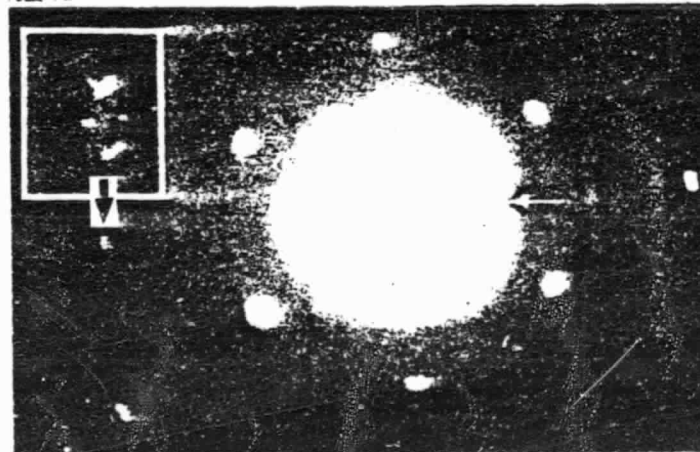
(b)

Figure 11

ORIGINAL PAGE
BLACK AND WHITE PHOTOGRAPH



(a)



(b)

Figure 12

8. a. Regularly and b. irregularly shaped precipitate, imaged with lattice resolution. Note the 'amorphous' looking patches within the precipitates. Insets represent the Si-lattice as projected along an $\langle 110 \rangle$ -direction, the traces of the $\{111\}$ planes are indicated.
9. a. Stacking fault crossing a thin twin. Both are seen inclined to the electron beam by several degrees.
b. Same area, but stacking fault and microtwin seen edge-on. Several precipitates are also present. Bright field. Multibeam along $\langle 110 \rangle$ axis.
10. Complicated arrangement of lattice dislocations, partial dislocations, stacking faults and small dislocation loops. Bright field. Multibeam along $\langle 110 \rangle$ axis.